# Structural and Mechanical Properties of Intermediate Filaments under Extreme Conditions and Disease

by
Zhao Qin

B. Eng. Engineering Mechanics
Tsinghua University, 2006

M.Eng. Engineering Mechanics
Tsinghua University, 2008



SUBMITTED TO THE DEPAREMENT OF CIVIL & ENVIRONMENTAL ENGINEERING
IN PARTIAL FULFILLMENT OF THE REQUIREMENT FOR THE DEGREE OF

DOCTOR OF PHILOSOPHY IN THE FIELD OF STRUCTURES AND MATERIALS
AT THE
MASSACHUSETTS INSTITUTE OF TECHNOLOGY

FEBRUARY 2013



Signature of Author: _____
Department of Civil and Environmental Engineering
November 29, 2012

Certified by: _____
Markus J. Buehler
Associate Professor of Civil and Environmental Engineering
Thesis Supervisor

Accepted by: _____
Heidi M. Nepf
Chair, Departmental Committee for Graduate Students

# Structural and Mechanical Properties of Intermediate Filaments under Extreme Conditions and Disease

by

Zhao Qin

Submitted to the Department of Civil and Environmental Engineering
on November 29, 2012 in Partial Fulfillment of the Requirement for the Degree of Doctor of Philosophy in the Field of
Structures and Materials

**ABSTRACT**

Intermediate filaments are one of the three major components of the cytoskeleton in eukaryotic cells. It was discovered during the recent decades that intermediate filament proteins play key roles to reinforce cells subjected to large-deformation as well as participate in signal transduction. However, it is still poorly understood how the nanoscopic structure, as well as the biochemical properties of these protein molecules contribute to their biomechanical functions. In this research we investigate the material function of intermediate filaments under various extreme mechanical conditions as well as disease states. We use a full atomistic model and study its response to mechanical stresses. Learning from the mechanical response obtained from atomistic simulations, we build mesoscopic models following the finer-trains-coarser principles. By using this multiple-scale model, we present a detailed analysis of the mechanical properties and associated deformation mechanisms of intermediate filament network. We reveal the mechanism of a transition from alpha-helices to beta-sheets with subsequent intermolecular sliding under mechanical force, which has been inferred previously from experimental results. This nanoscale mechanism results in a characteristic nonlinear force-extension curve, which leads to a delocalization of mechanical energy and prevents catastrophic fracture. This explains how intermediate filament can withstand extreme mechanical deformation of >100% strain despite the presence of structural defects. We combine computational and experimental techniques to investigate the molecular mechanism of Hutchinson–Gilford progeria syndrome, a premature aging disease. We find that the mutated lamin tail domain is more compact and stable than the normal one. This altered structure and stability may enhance the association of intermediate filaments with the nuclear membrane, providing a molecular mechanism of the disease. We study the nuclear membrane association with intermediate filaments by focusing on the effect of calcium on the maturation process of lamin A. Our result shows that calcium plays a regulatory role in the post-translational processing of lamin A by tuning its molecular conformation and mechanics. Based on these findings we demonstrate that multiple-scale computational modeling provides a useful tool in understanding the biomechanical property and disease mechanism of intermediate filaments. We provide a perspective on research opportunities to improve the foundation for engineering the mechanical and biochemical functions of biomaterials.

Thesis Supervisor: Markus J. Buehler

Title: Associate Professor of Civil and Environmental Engineering

*This thesis is dedicated to my parents and my love*

# Acknowledgement

During my study, research and my thesis preparation over the last few years, many people have supported me directly and indirectly. I would like to use this inadequate space to give those people sincerely gratitude. My most cordial appreciation goes to my thesis supervisor, Professor Markus J. Buehler, for his recognition and continuous support, patient guidance and teaching, great encouragement and inspiring, as well as the trust and friendship during my study life at MIT. Due to his great effort we were able to publish many parts of the thesis in peer-reviewed scientific journals, books and present the finds in many conferences.

Moreover, I would like to thank Professor Kris N. Dahl of Carnegie Mellon University for her encouragement and support to my work. Her help contributed a lot to this research. I sincerely thank my committee members for their continuous help, useful insights, valuable availability and kind willingness to serve in my committee. In particular, I sincerely thank Professor Roger D. Kamm for guiding me by proving many useful suggestions and selflessness support in thesis meetings and personal meetings. I would like to extend my gratitude to Professor Sidney Yip for kindly sharing his valuable experience in research and career development, as well as his insight on the physical mechanism of material behaviors. I would like to thank Professor Oral Buyukozturk for his insight on the mechanics and application of materials, inspiring my future researcher goals.

I would like to thank Professor Laurent Kreplak for providing experimental insights related to intermediate filament tests. I thank Professor Nicola Pugno for sharing insights on the mechanics of biological materials. For their friendship, moral support and fruitful discussions at work, I thank my labmates Graham Bratzel, Dieter Brommer, Shu-Wei Chang, Chia-Ching Chou, Greta Gronau, Leon Dimas, Tristan Giesa, Anna Tarakanova, Max Solar, Chun-Teh Chen, David Adler, as well as Dr. Steve Cranford, Dr. Arun Nair, Dr. Seunghwa Ryu, Dr. Baptiste Depalle and Dr. Shangchao Lin. I would like to thank my UROP student Andrea Fabre and RSI student Hadass Inbar, for the time of fun when we worked together.

I would like to express my gratitude to all my friends and colleagues for many years support in my research and life, especially for Dr. Zhiping Xu, Dr. Lifeng Wang, Ming Guo, Dr. Allison Beese, Dr. Raffaella Paparcone, Andre Garcia, Dr. Sinan Keten, Dr. Dipanjan Sen and Dr. Haimin Yao and many other people, giving me many wonderful memories in Boston.

I acknowledge the generous funding support for my research and my study at MIT. The Air Force Office of Scientific Research (grant FA9550081-0321), Office of Naval Research (grants N000141010562 and N000140810844), DOD-MURI (grant W911NF-09-1-0541) and China Scholarship Council (for the Chinese Government Award for Outstanding Self-financed Student Abroad) are gratefully acknowledged.

Finally, I want to express my love to my parents, Rui Liu and Qianyu Qin, for bringing me up, educating and encouraging me for the past twenty nine years. I give my special appreciation to Qingyi Yu for all she has done to greatly support me. Their love always accompanies me and makes this research possible.

# Table of Contents

## List of Figures

## List of Tables

# 1 Introduction

## 1.1 Background

Living systems have developed effective strategies in adapting to the environment during the last 3.5 billion years. The structures of plants, fungi and bacteria cells are stabilized and protected mainly by their cell walls. Metazoan cells lack such cell wall structure, and other strategies are required to stabilize their conformations (Herrmann et al., 2007). Moreover, the behavior of animal cells prevents them from having cell walls, such as cell migration and contraction. Migration refers to the movement of cells which is a central process in the development and maintenance of organs, while contraction refers to the shortening of a cell and the concomitant development of tension that is important in generating force in muscles for locomotion and wound healing by closing the extracellular matrix. To survive in various extreme conditions and achieve mechanical functions, cell requires appropriate means to become integrated under mechanical stress. Cytoskeleton in metazoan cell serves as a scaffold to achieve those mechanical requirements. It maintains the cell shape, protects the cell, enables cellular motion and plays important roles in intracellular mass and signal transfers. For eukaryotic cells, there are three major components of the cytoskeleton: microtubules (MTs), intermediate filaments (IFs) and microfilaments (MFs). They have different mechanical functions in cells. IFs and MFs act like ropes to bear tensile force while MTs act like support beams to bear compression force. The name of IFs was termed in 1968 because their diameters are 8–12 nm, appearing to be intermediate in size among the other cytoskeletal components, MTs (25 nm) and MFs (7–9 nm) (Herrmann and Aebi, 2004; Ishikawa et al., 1968).

### 1.1.1 Physiological function of intermediate filament

IFs exist in nearly all eukaryotic cells and many biological materials including wool, hair and hooves (Hearle, 2000; Herrmann et al., 2007; Ishikawa et al., 1968; Omary et al., 2004). Like many other fibrous proteins, such as collagen or fibrin, they linearly and laterally self-assemble into filaments which appear to be intermediate in size between MTs and MFs (Ishikawa et al., 1968; Kreplak and Fudge, 2007). These three components work together to enhance the structural integrity, and motility of cells. Besides the diameter differences, IFs are more flexible to adopt multiple conformations than microtubules, and they are more extensible when subjected to the tensile stress than those two components (Kreplak and Fudge, 2007). Its most fundamental subunit is called a dimer and has a common tri-partite organization characterized by a central alpha-helical coiled-coil domain and amorphous "head" and "tail" domains of variable length and sequence (Chang and Goldman, 2004; Herrmann and Aebi, 2004; Herrmann et al., 2007).

Compared to MTs and MFs, the IF family has more members and each of them features specialized functions. For instance, the IF protein family in humans contains more than 70 proteins (Herrmann et al., 2007; Omary et al., 2004), which are classified into five distinct

types based on their similarities in sequence and the tissue distribution (Chang and Goldman, 2004; Strelkov et al., 2003). Type I and II IFs are acidic keratin and basic keratin produced by different epithelial cells, respectively. Keratins play the key role to maintain the cell's stability in its morphology and contribute to the stability of mechanical connection to adjacent cells (Moll et al., 2008). Type III IFs include vimentin, desmin, glial fibrillary acidic protein, syncoilin and peripherin. Vimentin is found in the cytoplasm of fibroblasts, leukocytes, and blood vessel endothelial cells. It plays a significant role in maintaining cell's integrity by supporting and anchoring the position of the organelles in the cytoplasm (Herrmann et al., 2007). Type IV IFs are mostly inside the nervous system including neurofilament, internexin and nestin. Neurofilaments are found specifically in neurons and they provide structural support for axonal radial growth, leading to an axon diameter increase by a factor of five (Jafari et al., 1997). Type V IFs include lamin which forms a filamentous support inside the inner nuclear membrane. It contributes largely to the structural integrity of the nucleus and plays a vital biological role in the process of the re-formation of the nuclear envelope after cell division (Dahl et al., 2004; Wilson et al., 2001).

Due to their important mechanical roles in cells and tissues, IFs have been referred to as "safety belts of cells". There is evidence to show that the mechanical function of IFs plays a central role among their physiological functions (Wang and Stamenovic, 2002) but conventional material or biological models have failed to explain the mechanism behind (Buehler and Yung, 2009). Nevertheless, recent research have revealed a multitude of mutations in various IF proteins, leading to complex diseases (Omary et al., 2004). Those diseases cause cellular defects, leading to fragility in tissues, including skin, cornea, or muscle (Hegele, 2003; Hegele, 2007; Sylvius and Tesson, 2006; van der Kooi et al., 2002; Vlcek and Foisner, 2007). Although several models involving stress, cell fate, gene expression and signaling pathways have been proposed, fundamental mechanisms of most IF diseases are not at all clear (Cohen et al., 2008; Qin et al., 2010). For example, the complete mechanism of Hutchinson–Gilford progeria syndrome, which is also known as rapid aging disease, is still not clear (Dahl et al., 2006). Children with this syndrome experience severe hardening of arteries and this condition significantly increases the chance to have a heart attack at an early age and die prematurely (Vlcek and Foisner, 2007). By systematically comparing the patients' DNA sequences to normal ones, a point mutation in DNA has been identified that leads to a 50 amino acid deletion in the lamin tail domain (Eriksson et al., 2003). *In vivo* experimental work has provided evidence that the mutated lamin forms more ordered and rigid networks than the wild type (Dahl et al., 2006). However there is relatively little theoretical or modeling work to explain the mechanism by which the peptide deletion causes the nuclear lamina to become unstable, leaving the disease mechanism and process largely elusive.

### 1.1.2 Structural and mechanical investigation of intermediate filament

It is now clear that the nanostructure and nanomechanical properties of intermediate filaments are the key to understanding mechanisms of intermediate-filament-related diseases, since most known genetic diseases stem from single point mutations (Buehler and Yung, 2009; Omary et al., 2004). However, to fully understand the mutation effects one needs to develop a systematic perspective by considering the tissue as an integrated system. Some of the molecular interactions are strong and appear to be critical during physiological processes,

and thus cannot be removed or altered without changing the tissue function. Molecular modeling has shown that a single point mutation is hardly sufficient to affect the mechanical features of a lamin dimer as a standalone system, but its influence appears in the hierarchical context (Zhang et al., 2008). These evidences make us believe that any study restricted to a single scale level is far from enough to model and fully understand an IF system. Thus researchers are challenged by how to effectively study the hierarchical IF structures and material functions at multiple scales.

The monomer of IF proteins is composed of a central α-helical domain with each end capped by non-helical "head" and "tail" domains (Fuchs and Weber, 1994). Two monomers twist around each other to form a coiled-coil dimer, which is stabilized by a hydrophobic left-handed stripe that winds around the axis of each α-helix (Smith et al., 2002). Two dimers then form a tetramer and eight tetramers associate with each other to form a cylindrical unit-length filament (ULF) (Sokolova et al., 2006). The assembly of eight tetramers into ULFs takes a couple of seconds. Unlike MFs and MTs that assemble by monomer or dimer additions at one end, IF assembly proceeds by the end-to-end fusion of ULFs at time scales of minutes (Herrmann et al., 1999). Both ends of the obtained filaments are still active for fusion as demonstrated by a recent kinetic study (Kirmse et al., 2007). The final stage of assembly is a radial compaction of the filaments accompanied by distinct structural rearrangements at the molecular (Georgakopoulou et al., 2009) and supramolecular levels (Mucke et al., 2004b; Steinert et al., 1993). This self-assembly mechanism gives rise to a hierarchical structure of IFs that yield unique mechanical properties (Herrmann et al., 2007; Kreplak and Fudge, 2007; Kreplak et al., 2004a; Qin et al., 2009c).

Vimentin is one of the most important IFs. Its structure is hierarchical as illustrated in Fig. 1.1, ranging from atomistic scale to the cellular scale. The vimentin dimer represents the most fundamental building block, which contains two chains each coded by 466 amino acid residues for human. Each dimer consists of four major rod-like segments linked in series in the sequence 1A (residues 78–138), 1B (residues 147–247), 2A (residues 264–283) and 2B (residues 291–405), connected by linkers L1, L12 and L2, as shown in Fig. 1.2. The four rod-like segments are coiled-coils, whereas the linker domains may have irregular conformations that lead to discontinuities. Although there exists clear evidence that IFs play a key role in important physiological and pathological mechanisms, a complete atomistic-level molecular model of the basic constituents of this kind of protein material remains elusive. Parts of those segments, including 1A, L1, 1B, 2A, L2 and 2B domain of the vimentin dimer structure, have been crystallized and their atomistic structure identified based on X-ray diffraction experiments (Chernyatina et al., 2012; Nicolet et al., 2010; Parry et al., 2007; Sokolova et al., 2006; Strelkov et al., 2002; Strelkov et al., 2001). There are persistent experimental challenges in identifying the entire vimentin IF structure.

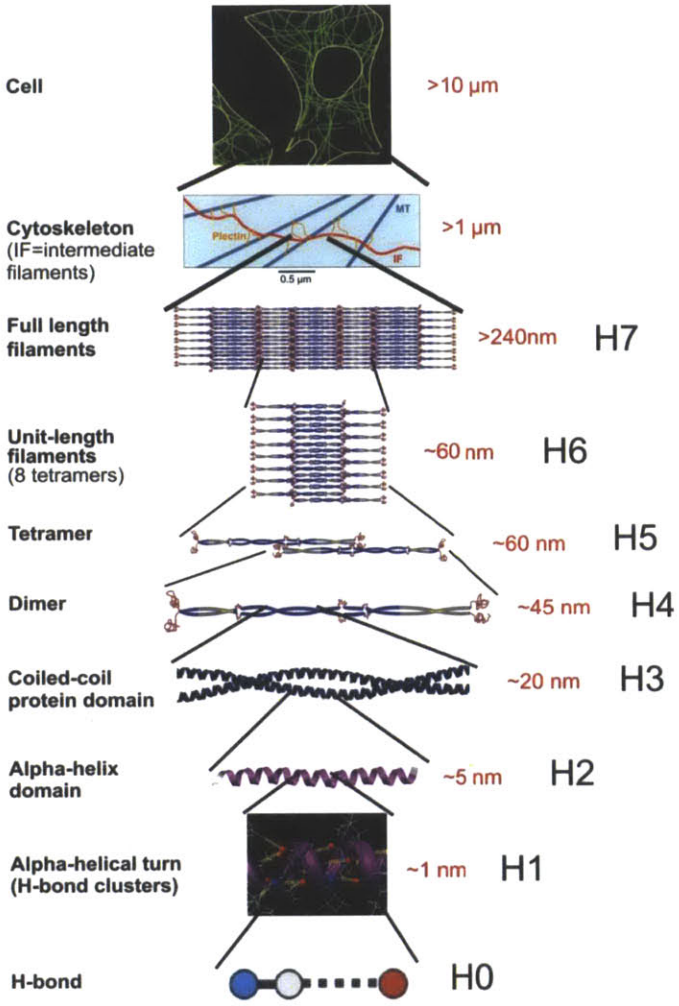


**Fig. 1.1 The hierarchical structure of intermediate filaments (Qin et al., 2009b; Qin et al., 2010).** The figure shows relevant structural levels H0–H7 from atomistic to full length filament levels, as well as the schematic about how it scales up to cellular scale.

The unavailability of the molecular structure prevents us from directly carrying out the molecular-level nanomechanical analysis of this protein. Earlier molecular dynamics studies have focused solely on a small section of the 1A and 2B domain (Ackbarow and Buehler, 2007; Zhang et al., 2008), without considering the properties of the whole dimer structure as shown in Fig. 1.2. Furthermore, recent experimental studies using atomic force microscopy (AFM) analyses focused on the mechanical properties of entire IF filaments or filaments with similar structures (Kreplak and Bar, 2009b; Kreplak et al., 2008), but left the details of the mechanisms of IF deformation remain unknown.

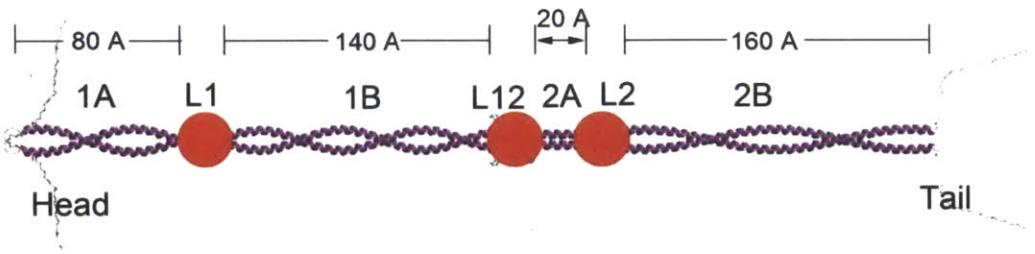


**Fig. 1.2 Schematic representation of a vimentin dimer structure (Qin and Buehler, 2009).** The labels identify the various segments and linker domains.

### 1.1.3 Molecular dynamics simulations

Atomistic molecular dynamics (MD) is a suitable tool for elucidating the atomistic mechanisms that control deformation and rupture of chemical bonds at the nanoscopic scale. It reveals the nanomechanics of materials, and relates this characteristic to macroscopic material deformation and failure. For example, MD simulations have revealed mechanisms of fracture in brittle materials (Buehler and Gao, 2006; Buehler et al., 2003; Buehler et al., 2006; Buehler et al., 2007). The base behind atomistic MD is to explicitly calculate the trajectory of each atom in the material as a function of time, by considering their atomistic interactions and by solving each atom's motion equation according to the basic Newton's law as $F = m \cdot a$. By selecting proper inter-atomic potential function (called force field) as well as by performing numerical integration of the motion equation, one is able to simulate the behavior of a large ensemble of atoms that represents a typical material volume. There are several limits that need to aware of for the application of this technique. The availability of a force field that can precisely describe the atomistic interaction of a specific material is often a limiting factor of this method. The computational power is another limit for the simulation size and time. Classical molecular dynamics computes the interacting and moving of a large number of $N$ particles according to the given force field. The computer calculates the accelerations, velocities and positions of all the particles for each time increment, resulting in the full trajectories of all the particles. This approach is parallel to methods like Monte-Carlo. Their main difference is that MD provides dynamical information and full trajectories as functions of physical time, while the Monte-Carlo method focuses on the equilibrated states without real-time information as well as the detail of transition process. Most simulation studies presented here are carried out with MD approach. However, we also heavily apply Replica Exchange Method (REMD) in our study (Sugita and Okamoto, 1999). This technique combines MD with the Monte-Carlo method, to accerlerate the protein folding calculation. Its principle and application will be discussed in detail in Chapter 6.

### 1.1.4 Multiple-scale modeling

The uniqueness of this thesis is the central role of multiple-scale computational modeling in a bottom-up design direction, differing from the up-bottom direction in classic biochemistry studies. In multiple-scale systems, atomistic interaction, structural effects,

thermal fluctuations, chemical reactions, point mutations can all be essential to quantitatively understanding of material functions and behaviors under extreme conditions, which is a feature roots in the nanoscale realm and extends to the macro realm as shown in Fig. 1.3. These factors govern signaling function, mechanical behavior and interactions with surrounding environments of IFs. With this approach, full understands of IFs become feasible in a rational and organized way. This includes its structure, mechanical property and how they interact with other cellular components. Those characteristics cannot be predicted by any single experiments. The multiple-scale modeling can also improve our understanding of the physiological function of intermediate filaments. For example, how a point mutation alters the IF structure, stiffness and its interaction with other protein, and how those alterations result in distinctly different mechanical functions can be understood by multiple-scale modeling.

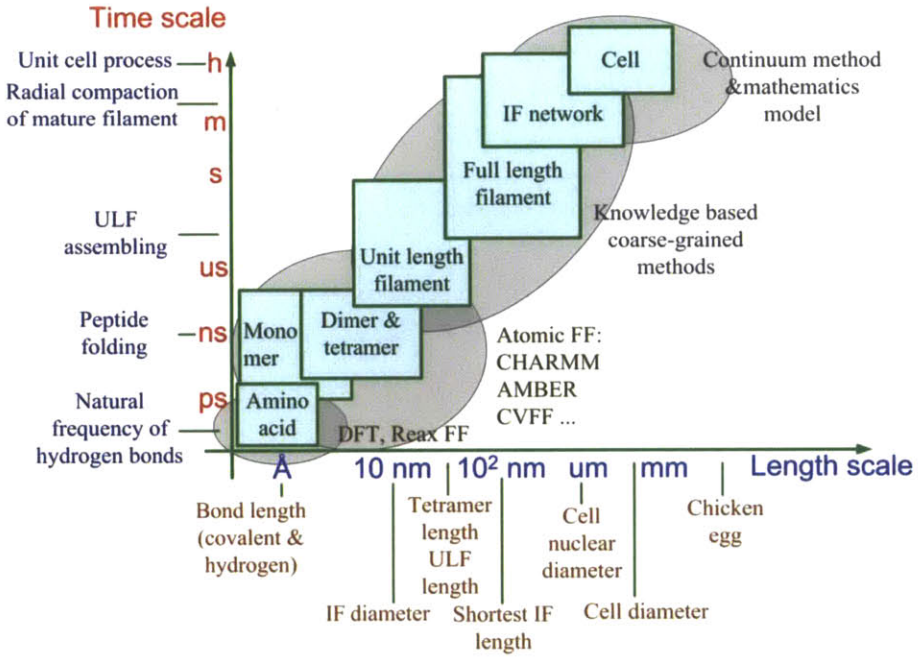


**Fig. 1.3 A schematic figure to summarize the basic approach of the step-by-step finer-trains-coarser procedure of studying the structure and mechanical properties of intermediate filament networks by invoking multiple-scale computational methods (Qin and Buehler, 2012a).** For each subunit level (such as amino acid, monomer, dimer and so on), the corresponding time and length scales are as noted by the $y$ and $x$ axis and sample modeling methods are noted in the gray shaded ellipses.

## 1.2 Research objective

The objective of this research is to develop an in-depth nanomechanical understanding on the hierarchical structural and mechanical properties of IFs, as well as how those properties relate to IFs' functions under many physiological conditions. The study extends our understanding of IFs' biomechanical behaviors, such as deformation, yielding, structural transition and fracture, under extreme conditions, including mechanical stress, defect,

mutations and ionic conditions. We focus on studying those behaviors from a materials science perspective, and on their roles in leading to their biological functions, specifically materials failure in disease or extreme mechanical conditions. The knowledge provides mechanistic insight to reveal relations between structural, mechanical, and functional properties in the biological context of IFs. We hope this systematic investigation would facilitate the quantitative understanding of the property and function of biological materials, as well as it may give principles in designing bio-inspired materials for biomedical and engineering applications.

## 1.3 Research Approach

From the review of former studies on the physiological, structural and mechanical properties of IFs, it is seen that the physical mechanism which governs the material's behavior under various extreme conditions remains largely uncertain. In particular, the full atomistic structures of IF subunits are not available, as well as little is known about the mechanics of single intermediate filament or its subunits, including the mechanisms for its strain sensitivity, large extensibility and stiffening at large deformation. The robustness of the IF network has not been addressed. This is critical to understand how the material is able to maintain its performance under the existence of defects. In addition, it is largely unknown how genetic mutations affect the structural and mechanical properties of IFs. Conventional mechanics or physics models are unable to predict and explain those behaviors as many chemical and biological processes are coupled with IFs' mechanical response. Computational modeling and simulation turn out to be a useful tool for those problems. We use MD simulations to gain atomistic insight on the molecular system, and then use multiple-scale modeling following the finer-trains-coarser principle to obtain the large-scale material behavior without losing its molecular mechanism.

The IFs' nanomechanics is investigated by MD simulations that use several force fields to define the interaction among particles, including classical MD simulation based on CHARMM force field and steered molecular dynamics (SMD) method and coarse-grained method based on MARTINI force field (will be introduced in detail in Chapters 2 and 3). We also use replica exchange method and metadynamics method to increase the sampling space and accelerate the simulation speed to obtain a more precisely described molecular structural as well as its conformational free energy landscape (will be introduced in detail in Chapter 6 and 7). Using the results of atomistic simulations, we apply appropriate multiple-scale modeling method to describe the larger scale material (IF network) behaviors under extreme conditions (will be introduced in detail in Chapter 4). Both the results from MD simulations and multiple-scale modeling have been validated by experiments, some are obtained from literatures and some are measured by our experimental collaborators performing tests in parallel with our simulations. The details of experiments and comparisons will be given in each following chapter.

This research is motivated by the lack of molecular understanding of IF, which is an important cytoskeleton material with its biomechanical function largely unknown. It is anticipated that this work would receive much attention from the IF society as well as

scientific fields including biomechanics, biomaterials, biophysics and nanomechanics. This research provides some essential principles for understanding how sequence, microscopic structure and chemical condition affect properties and functions of protein materials. This knowledge may facilitate bio-inspired material design, as well as improve understanding of their tunable mechanical properties. New protein materials could be designed and produced according to computational modeling and simulation. This could inspire and shorten the material design time and meet the requirements of engineering and biomedical applications, which eventually contribute to human wellbeing.

## 1.4 Thesis organization

This thesis consists of seven subsequence chapters.

Chapter 1 Presents a review on former investigations of the property and function of intermediate filaments, focusing on their physiological function, structural and mechanical properties. A general introduction to MD simulation and multiple-scale modeling method is given in this chapter as is the fundamental technique applied through this research.

Chapter 2 Presents the procedure to build the full atomistic model of vimentin according to structural homology method that combines the protein sequence and experimental descriptions of protein structures. We test the structures in multiple MD simulations with different force fields and compare their equilibrated conformations against experimental observations.

Chapter 3 Presents the procedure to use the atomistic model of vimentin and steer molecular dynamics method to obtain the force-extension function of vimentin dimer and tetramer. The mechanism of the secondary structural transition from α-helix to β-sheet for IFs under tensile force is discussed here, which largely explains the nonlinear mechanical behavior of IFs. In addition, we discuss the rate dependence of IF mechanics under tension.

Chapter 4 Presents the multiple-scale modeling of nuclear lamina network and investigates the mechanism of its flaw tolerance characteristic. We reveal that the secondary structural transition and the crosslink strength contribute to this advanced property.

Chapter 5 Focuses on the structure and mechanical property of the tail domain of lamin A and its mutated counterpart by using the replica exchange method. Our result presents the molecular mechanism of Hutchinson–Gilford progeria syndrome, which is also known as rapid aging disease.

Chapter 6 Focuses on the calcium effect on the structure and physiological function of

lamin A tail. Combined with in-parallel experimental studies, our result provides a more complete description of the maturation process of lamin A, making the pathway of lamin diseases more clear.

Chapter 7 Presents a summary of this thesis and provides conclusions of this work. Future plans and expectations are also included.

# 2 Atomistic modeling of intermediate filament

Intermediate filaments (IFs) are one of the major building materials of the cytoskeleton in eukaryotic cells, and are crucial in the determination of cell mechanical properties (Herrmann and Aebi, 2004; Herrmann et al., 2007; Hutchison, 2002). IFs are crucial in defining key functions of cells such as cell migration, cell division and mechanotransduction, and it is now understood that they play a critical role similar to other cytoskeleton elements such as microtubules and microfilaments. Notably and pointing to their rather important role as mechanical elements, IFs have also been referred to as the 'safety belts of cells', and have been demonstrated to play a role in preventing exceedingly large cell stretch (Fudge et al., 2008; Wang and Stamenovic, 2002; Wang et al., 1993b). A range of studies published over the past years focused on the mechanical signature of IFs. They have suggested that IFs can sustain extremely large deformation of up to several 100% (Herrmann et al., 2007; Kreplak et al., 2008; Lewis et al., 2003). It was also found that due to severe stiffening, the tangent modulus of IFs increases manifold during deformation, which clearly could be crucial for providing mechanical resistance against large stretching. In addition to the cell's cytoskeleton, IFs are also found in the cell nucleus in the form of lamin IF, where they form a dense mesh-like network providing mechanical integrity and biochemical functions at the cytoskeleton-chromatin interface (Ackbarow et al., 2009; Dahl et al., 2004; Wilson et al., 2001). Numerous diseases associated with IFs were identified which point to the clear importance of material factors in the initiation and progression of these disorders (Brenner et al., 2001; Buehler and Yung, 2009; Omary et al., 2004).

## 2.1 Background on experimental evidence of vimentin structure

Vimentin filaments are the most widely distributed type among all IFs (Alberts et al., 2008) and will be the focal point of the study reported here. Its basic unit is a long monomer made up of 466 amino acid residues consisting of four segments: head, 1A, 1B, 2A, 2B and tail divided by three linkers: L1, L12, L2 as shown in Fig. 2.1. Segment 2A (residues 264–282) is the shortest one among all segments. Earlier assumptions suggest the configuration of a nearly parallel alpha-helical bundle (Nicolet et al., 2010; Parry et al., 2007; Qin et al., 2009a). Segment 2B with 115 amino acids (residues 291–405) features alpha-helical coiled-coil geometry for the major segment. One of the discontinuities found in heptad repeats of an alpha-helical coiled-coil protein is the 'stutter' region. As a result it has been suggested that the molecular structure may be altered in this region and deviate from the perfectly coiled regions in the rest of the protein filament. The 2B segment of vimentin contains the stutter region as pointed out in Fig. 2.1 (Ackbarow and Buehler, 2009; Brown et al., 1996; Strelkov et al., 2001). It can be seen that the stutter is located at the end of the eighth heptad, in the vicinity of residue 351 (Strelkov et al., 2002). An analysis of the amino acid sequence revealed that the nature of the vicinity of the stutter region is hydrophilic. Earlier work suggested that this result is in a parallel arrangement for the two coils in the alpha helix rather than a coiled-coil configuration. Although parts of the vimentin dimer

structure have been revealed by a divide-and-conquer method in experiments, a complete atomistic-level molecular model of the basic constituents of this kind of protein material remains elusive. There are persistent experimental challenges in identifying the remaining parts of the vimentin IF structure. Since IFs are intrinsically disordered structures (Rafik et al., 2004), X-ray diffraction studies on naturally occurring or recombinantly produced IF bundles do not provide sufficient data to produce a full atomistic model of IFs. Solid state nuclear magnetic resonance has been successfully utilized to derive atomistic models of amyloid fibrils (Luca et al., 2007). However, units of amyloid peptides are much smaller than IF dimers, so that this approach may remain unsuccessful as well. Finally, cryo-electron tomography offers the promise of molecular-level imaging of single IFs, but the best tomograms are currently limited to a resolution around 5 nm (Goldie et al., 2007). Far-field fluorescence microscopy techniques combined with recently developed super-resolution techniques manage to actively control the fluorophore emission in any imaging frame and thus the resulting image can reach a resolution of 20 nm (Lee et al., 2012). It can be used to observe the 3D profile of intermediate filaments and their dynamic behavior inside cells, but the resolution is even further from being sufficient for molecular modeling.

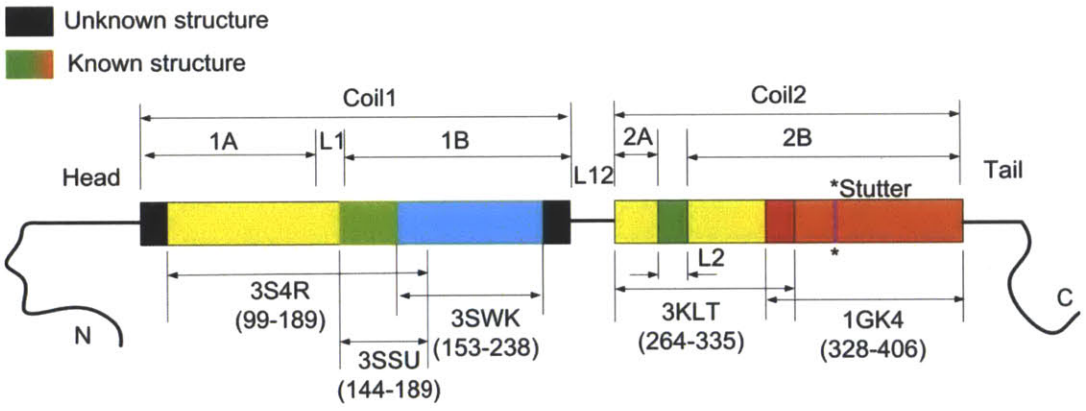


**Fig. 2.1 Schematic view of human vimentin dimer and the regions with their structure revealed by X-ray diffraction (colorful) (Chernyatina et al., 2012; Nicolet et al., 2010; Parry et al., 2007; Sokolova et al., 2006; Strelkov et al., 2002; Strelkov et al., 2001).** The location of the stutter region pointed out by the * symbol.

The intrinsic limitations in experimental methods call for the development of complementary computational methods that can provide a more controlled condition to assess the relation between the nanostructure and nanomechanics of this class of materials. Atomic interactions, which are difficult to be directly measured from experiments, can be computed by first-principles based calculations such as density functional theory (DFT) and relevant numerical implementations. Several massive sampling techniques have been developed during recent years, making protein structure prediction and refinement increasingly feasible (Khatib et al., 2011; Zagrovic et al., 2002), making it feasible to study protein structures in computers.

### 2.1.1 Hierarchical structure of vimentin

Vimentin form hierarchical structures similar to other IFs as shown in Fig. 1.1, ranging

from H-bonds, clusters of hydrogen-bonds (H-bonds) in alpha-helical turns, alpha-helical proteins, dimers, tetramers, unit length filaments, full-length filaments to cellular level.

The basic building block of all IFs is a particularly stable molecular configuration of H-bonded alpha-helix-based protein structures called coiled coils (Alberts et al., 2008; Rose and Meier, 2004). This arrangement of two alpha helices that coil together into coiled-coil domains provides increased strength to the structures. In α-helix-based-coiled coils within a single heptad repeat (with *abcdefg* periodicity), some positions are occupied by hydrophilic (polar) and some are occupied by hydrophobic (non-polar) residues (Buehler and Ackbarow, 2008; MacCallum et al., 2007; Strelkov et al., 2003). The hydrophobic residues are the reason why these proteins assemble into coiled-coil structures to ensure minimal contact of hydrophobic residues with water.

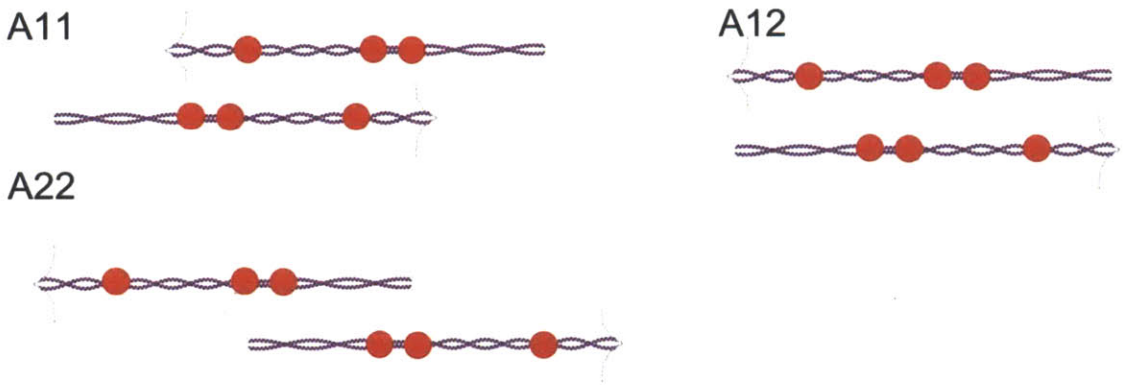


**Fig. 2.2 Schematic representation of vimentin tetramer (Li and Sun, 2012).** Typical geometry of vimentin tetramer observed in experiments: A11, A12 and A22.

Each vimentin dimer, forming the fundamental building block of IFs, is composed of four rod-like structural segments are consisted in the dimer sequentially in the order of 1A, 1B, 2A and 2B, connected by linkers L1, L12 and L2 (Fig. 2.1). Outside the rod-like structure, there is an amorphous head and an amorphous tail domain. Two dimers come together and interact with each other to form a tetramer structure. Three main antiparallel arrangements are found in experiments for this interaction as shown in Fig. 2.2 (Herrmann and Aebi, 1998): A11, the coiled-coil domain of helix 1B of one dimer interacts with the same domain of a second dimer in the antiparallel way; A12, the coiled-coil domain of helix 2B of one dimer interacts with the 1A and 1B domains of a second dimer in the antiparallel way; A22, the coiled-coil domain of helix 2B of one dimer interacts with the 2B domains of a second dimer antiparallelly. Normally, A11 and A22 are found in assembling process at the tetramer stage but A12 is only found in higher assembling stage. A higher level structure is unit length filament, which includes a bundle of 8 tetramers. It is observed in experiment that the head and tail domains play roles at structure levels higher than tetramer level. The headless IF proteins form only dimers and tetramers under conditions of ionic strength lower and pH higher than standard buffer, but no higher-order structures (particularly, no octamers) (Herrmann and Aebi, 1998). This has been shown independently for headtruncated desmin, cytokeratins, and vimentin (Herrmann and Aebi, 1998). There are two possible reasons: the

head domain is needed to allow adding dimers to the tetramer in forming unit length filament, and headless IF dimers associated in the A12 mode does not allow further assembling. This finding indicates that the head domain is necessary for productive formation of octamers from tetramers. Another concern for quite some time is the role of the amorphous tail domain in assembling process or lateral interaction of individual IFs. By analyzing early assembly of tailless vimentins, it was shown that they form IFs in a manner analogous to intact vimentin. However, tailless IFs exhibit no significant tendency for lateral aggregation. It is also shown that tailless vimentins lose control of lateral growth, ending with increasing number of dimers/tetramers at filament cross sections. This finding indicates that the tail domain is necessary for controlling the conformation and interaction of full length filaments (Herrmann et al., 1996).

### 2.1.2 Known sequence and atomistic structure of vimentin dimer

The 466 amino acid sequence for each polypeptide chain of the dimer is gained from literature of human vimentin (Strelkov et al., 2001). Recent advances in identifying the structure of vimentin dimers with atomistic details (Nicolet et al., 2010; Strelkov et al., 2002), combined with protein simulation tools, now enable us to build molecular mechanics models of proteins at relatively large scales, involving tens of nanometres and with a full atomistic resolution. Importantly, the development of this large model based directly on X-ray diffraction data is an advance over earlier smaller models in which the stutter was placed closer to the boundary of the filament (Ackbarow and Buehler, 2009). The vimentin coil2 segment used here is obtained by combining two coiled-coil segments obtained directly from Protein Data Bank (PDB). The N-terminal half of coil2 is obtained from vimentin segment that includes residues 264–335 (PDB with identification (ID) (Nicolet et al., 2010)). The C-terminal half of coil2 is obtained from the vimentin segment that includes residues 328–406 (PDB with ID 1GK4 (Strelkov et al., 2002)). The two segments are aligned to form an integrated coiled coil because both fragments include an overlapped region of residues 328–335 as shown in Fig. 2.1. Other known structures include the crystallized 1A segment for vimentin that includes residues 100–138 (PDB with identification (ID) 1GK7 (Strelkov et al., 2002)), as well as the more recent discovery of the crystal structure of the 1B segment that includes residues 153-238 (PDB with identification (ID) 3SWK (Chernyatina et al., 2012)), a part of 1A segment that includes residues 144-189 (obtained from the PDB with identification (ID) 3SSU (Chernyatina et al., 2012)), a part of 1A segment that includes residues 99-189 (PDB with identification (ID) 3S4R (Chernyatina et al., 2012)).

Those known structures largely construct the rod-like domain of the vimentin dimer, as illustrated in Fig. 2.1. However, there are still some segments have unknown structures. Although techniques rather than X-ray diffraction data have revealed some structural characteristics of those unknown structures, for example, studies based on Electron Paramagnetic Resonance measurements have revealed that the local stiffness of L1 and L2 has local stiffness close to the rod-like domain (Aziz et al., 2012; Hess et al., 2006). Those domains turned out to be helical structures as reveal by the X-ray diffraction study. However, those experimental studies cannot relate directly to the atomistic structure of the vimentin dimer and thereby during the modeling process we heavily depend on those X-ray diffraction data as well as a structural homology method.

### 2.1.3 Data visualization methods

We use Visual Molecular Dynamics (VMD) (Humphrey et al., 1996) for visualization of protein structures as well as for the analysis of the structural transition. The structure analysis is done using the approach suggested in (Frishman and Argos, 1995). The rupture length of Hbonds is 3.7 Å for visualization in VMD. The criterion to identify H-bonding considers both hydrogen bond patterns and the backbone geometry, based on polypeptide chain dihedral angles.

## 2.2 Structural homology modeling method

We used the structural homology method to set up a structural model of intermediate filament dimer and tetramer structures. Each polypeptide chain of the dimer has the identical 466 amino acid sequence to reflect the exact sequence of human vimentin (Strelkov et al., 2001). The amino acids are connected by $\varphi = -58^{\circ}$ and $\psi = -47^{\circ}$ for the known conformation of alpha-helical segments (Brändén and Tooze, 1999), and by $\varphi = 180^{\circ}$ and $\psi = 180^{\circ}$ for the other unstructured parts of the chain. Note that the parameters $\varphi$ and $\psi$ are two characteristic dihedral angles that define the conformation of the protein backbone chain; these angles describe how two neighboring amino acids are connected to one another (Alberts et al., 2008). According to the sequence analysis, the 1A, 1B, 2A and 2B segments possess an initial alpha-helical structure, while the other parts of the chain are initially unstructured (Parry et al., 2007; Sokolova et al., 2006; Strelkov et al., 2001).

Each amino acid within the polypeptide chain takes the topology and local coordinates according to the intrinsic coordinate in the CHARMM 22 force field (MacKerell et al., 1998). Due to the polarities of the amino acids, the apolar amino acids in the 1A, 1B and 2B segments generate a hydrophobic stripe that winds around its helical axis with a left-handed heptad repeat. Via coordinate displacements and transformations, we combine two alpha-helics with initially straight axis together with specific distance and coiled angle to form a coiled-coil structure. This configuration is energetically favored since it shields apolar residues from the polar solvent environment (Apgar et al., 2008). The coiling angle is $3.51^{\circ}$/Å for 1A, $3.85^{\circ}$/Å for the 1B and $2.46^{\circ}$/Å for the 2B segment, as shown in Fig. 2.3. The coiling angles are lightly different in different segments because the twist angle of the hydrophobic stripe on each of the segments differs. This twist angle is determined by linear fitting of the angular coordinate $\theta$ of the hydrophobic amino acids with respect to their axial coordinate $z$ in the $R$-$\theta$-$z$ coordinate system of $C_{\alpha}$ atoms. In the 2A segment, the hydrophobic stripe is nearly parallel to the axis of the alpha-helix, resulting in a parallel alpha-helical bundle.

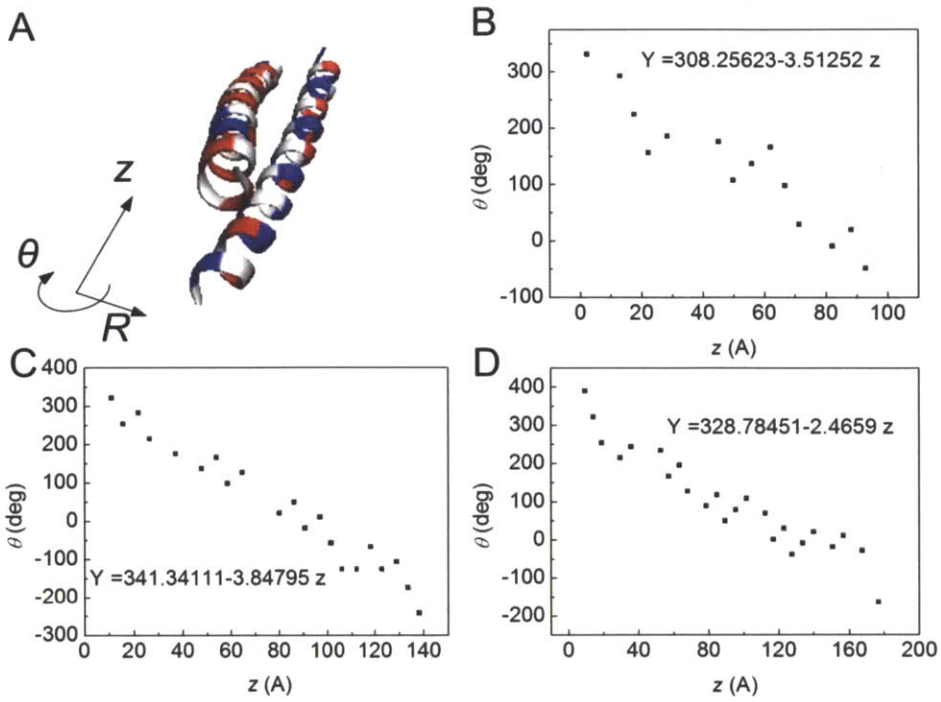


**Fig. 2.3 The geometry character of each coiled-coil domain in a vimentin dimer (Qin et al., 2009b).** Panel A: the schematic representation of a coiled coil segment, and the relative coordinate used to form the model. The hydrophobic amino acids are white, while other amino acids are colored; Panel B: the coordinates of the hydrophobic stripe along a chain in 1A domain; Panel C: the coordinates of the hydrophobic stripe in 1B domain; Panel D: the coordinates of the hydrophobic stripe in 2B domain.

We use this procedure to build the basic dimer model of the vimentin. We keep updating our structure to incorporate the X-ray diffraction data of vimentin. However, the crystallized structure of the vimentin Coil 1 has been largely unknown by X-ray diffraction before we build this structure. At the end of this chapter, we provide an updated structure to provide the most recent result.

### 2.2.1 The equilibration of vimentin dimer/tetramer by CHARMM force field

Atomistic force fields are predominantly used in MD simulations of biological materials at the microscopic scale as they generally are computational efficient but yet reliable way of studying dynamic behaviors of molecules. A wide range of force fields are available and compatible with many open-source MD packages, including the AMBER force field (Cornell et al., 1996), the CHARMM force field (MacKerell et al., 1998), the OPLS force field (Jorgensen et al., 1996), the CVFF force field (Dauberosguthorpe et al., 1988), the COMPASS force field (Sun, 1998), the DREIDING force field (Mayo et al., 1990), the GROMOS/GROMACS force field (Oostenbrink et al., 2004) and ReaxFF reactive force field (van Duin et al., 2001). Each of them has its own formula and a large set of parameters in describing the interaction among atoms in system. Everyone has its advantages in specific areas. For example, the AMBER force field is developed together with the MD software

package AMBER (developed by Peter Kollman's group at the University of California, San Francisco) with the purpose of simulating biomolecules. The CHARMM force field is developed together with the MD simulation and analysis package CHARMM (developed by Martin Karplus's group at Harvard University) with the purpose of simulating biomolecules and drug-like molecules. It is also heavily used by NAMD (Nelson et al., 1996), a very popular MD simulation package that is well developed for massive parallel computing, and it is well scaled for Graphics Processing Unit (GPU) that outperforms Central Processing Unit (CPU). The OPLS force field (developed by William L. Jorgensen's group at Purdue University and later at Yale University) is developed for molecules such as amorphous carbohydrates, especially optimized for describing their liquid and gas form. The CVFF force field is developed originally with with the Discover program in simulating amino acids, water, and a variety of other functional groups. The COMPASS force field is parameterized against a wide range of experimental observables for organic compounds, especially for molecules in their condensed phases. The DREIDING force field is a generic force field that useful for predicting structures and dynamics of organic, biological, and main-group inorganic molecules. DREIDING uses general force constants and geometry parameters based on simple hybridization considerations rather than parameters that depend on the particular combination of atoms. It is a generalized force field that may be used for rational molecule design. The GROMOS/GROMACS force field gets full support of GROMACS, which is a general-purpose MD simulation package for the study of biomolecular systems.

We use CHARMM force field to define the atomistic interactions for our model. CHARMM force field is widely used in the protein and biophysics community, and provides a reasonable description of the behavior of proteins. The parameters in this force fields are often determined from more accurate, quantum chemical simulation models and they have been optimized and revised over the years taking into consideration a wide variety of input including *ab initio* results, experimental crystal structures and geometries, as well as vibrational spectra (MacKerell et al., 1998). The force field includes bonding and non-bonding terms to describe covalently bonded and non-covalently bonded forces among particles. In the CHARMM model, the mathematical formulation for the empirical energy function has the form:

$$E = \sum E_{bond} + \sum E_{angle} + \sum E_{dihedral} + \sum E_{improper} + \sum E_{\text{Urey-Bradley}} + \sum E_{nonbonded} \quad (2.1)$$

Each energy term is given by $E_{bond} = K_{ij}(r - r_0)^2$ is the bond term that defines how two covalently bonded atoms interact in the stretching direction, $E_{angle} = K_{ijk}(\theta - \theta_0)^2$ is the angle term that defines how the angel among three covalently bonded atoms with one central atom changes under external force, $E_{dihedral} = K_{ijkl}[1 + \cos(n\phi - \delta)]$ is the dihedral term that defines how the dihedral angel among four covalently bonded atoms with one central bond changes under external force, $E_{improper} = K_{ijkl}(\omega - \omega_0)^2$ is the improper angle term that defines how the improper angle among four covalently bonded atoms with one central

atom changes under external force, $E_{\text{Urey-Bradley}} = K_u(u - u_0)^2$ is the Urey Bradley term that accounts for angle bending and $E_{nonbonded} = \epsilon_{lj}\left[\left(\frac{R}{r_{ij}}\right)^{12} - \left(\frac{R}{r_{ij}}\right)^{6}\right] + \frac{q_i q_j}{r_{ij}\epsilon}$ is the nonbonded term that accounts for the van Der Waals (VDW) energy and electrostatic energy. In all-atom force fields, water molecules generally can be treated explicitly or implicitly. Parameters of water molecules are given by specific water models (e.g. TIP3P model for CHARMM force field), which we will have an extended discussion in the next section. It is noted that in CHARMM and most other classical force fields, bonded terms are modeled by harmonic springs or its variations, and therefore cannot be modified (to have nonlinear stiffness) or broken once initially defined by the topology of the molecule (given in a .psf file). Further, the atomic charges are embedded and cannot change during a run. Those functions are included in the ReaxFF reactive force field which includes the bond breaking and charge equilibrium functions during the simulation but they make the system much more complex by adding more degree of freedom, making each time step increment more computing effort. The simplifications in CHARMM force field improve its speed and robustness during the run, making it suitable for large systems and running for long time.

We first use the CHARMM19 all-atom force field to define the atomic interactions within the dimer and tetramer model. The solvent effect is generally considered by using the implicit Gaussian model (EEF1) for the water solvent (Lazaridis and Karplus, 1997; Lazaridis and Karplus, 1999). The use of the implicit solvent model has advantages to accelerate the sampling speed of molecular configurations, so that more configurations are visited per simulated nanosecond. Overall, the use of this solvent potential has been shown to be an efficient and reliable approach to take into account solvent effects of large molecular structures suitable for structure prediction applications (Best et al., 2007; Paci and Karplus, 1999; Paci and Karplus, 2000). This molecular model is currently the only feasible approach to simulate large protein structures as considered here at sufficiently long time required for structural equilibration. We use CHARMM package to run the simulation for structural equilibration, the time step used in all simulations is 1 fs. A series of computational steps are adopted to equilibrate the structure. Starting from the initial geometry obtained from structural homology method we follow the following protocol to equilibrate the structure referring to literature (Miteva et al., 2004):

1) Energy minimization (10,000 Steepest Descent steps followed by 10,000 Adopted Basis Newton-Raphson steps).

2) Equilibration runs for 5 ns (NVT ensemble with Nose-Hoover temperature control), where the temperature rises linearly from 240 K (beginning) to 300 K (end).

This precedue is repeated for 10 times to ensure the structure reach an equilibrium state. A final equilibration run at 300 K for 10 ns is given at the end of the cycle. Aside from random fluctuations of the molecule, no significant change in the molecular structure is observed after a few iterations, suggesting that the ten cycles are sufficient to reach a properly equilibrated vimentin structure.

Fig. 2.4A shows a snapshot of the molecular model of the vimentin dimer, displaying the characteristic segmented geometry with coiled-coil regions connected through linker domains. The total length of the dimer without the head and tail domain is <48.7 nm. This result is in agreement with experimental results where a range of 46–49 nm has been reported earlier (Mucke et al., 2004b; Sokolova et al., 2006). From dynamical analyses of the molecular dynamics trajectory of the dimer at 300 K, we observe that the linker domains represent soft, hinge-like structures that connect much stiffer coiled-coil segments. This heterogeneous distribution of the bending stiffness along the molecule's axis strongly affects filament's motion by enhancing its mobility due to an effectively reduced persistence length, which might be significant for IF selfassembly. Thereby, the linker domains act as hinges around which rod-like domains can rather easily bend and rotate.

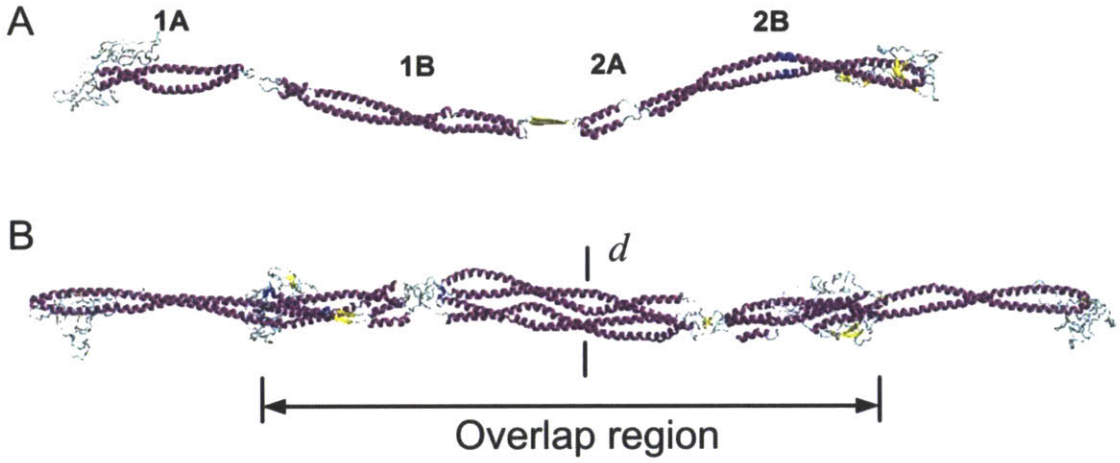


**Fig. 2.4 Molecular structures of vimentin dimer and tetramer (Qin and Buehler, 2010a).** Panel A: Snapshot of the atomistic model of the dimer. The blue part denotes the stutter part around the stutter (amino acids 345-351). Panel B: Snapshot of the atomistic model of the tetramer.

Figure 2.4B shows a snapshot of the molecular model of the vimentin tetramer, consisting of two anti-parallel dimers (Sokolova et al., 2006). The total length of the tetramer is ≈61.3 nm, which agrees with the length of unit length filaments observed in experiment (62 nm at pH 7.5 (Mucke et al., 2004b)). The overlap part of the tetramer has a length of ≈36 nm, where the experimental value is 30–36 nm (Mucke et al., 2004b; Sokolova et al., 2006). Segments 1A, 1B and 2A are fully contained in this part, but the 2B segments in the immediate vicinity of the two terminals locate completely outside. We find that the head segment of each dimer is coiled around the other dimer, increasing the contact surface area and thereby providing enhanced interdimer interactions. This structure is an alternative configuration to the sandwich model that has been discussed as a possible tetramer arrangement, where the head domain locates between the two dimers (Kreplak et al., 2004a). From the simulation we observe that the equilibrated structure of the vimentin tetramer shows that the overlapped L1/L12 linker domains represent regions of small bending stiffness. From an analysis of the movie it can be seen that compared with the dimer structure, the tetramer

structure is notably stiffer due to its increased area moment of inertia, resulting in an effectively increased persistence length. Atomistic level geometry PDB files of the dimer and tetramer are generated and provided (Qin et al., 2009b).

In both protein structures, the 1A segment contains 61 amino acids (residues 78–138), for which both phenylalanine and tyrosine residues are packed consecutively at the hydrophobic core positions near the segment center (Smith et al., 2002). Therefore, the 1A segment is only marginally stable, which increases the mobility of the head domain during IF assembly as suggested in (Strelkov et al., 2002). Segment 1B (residues 147–247) contains 101 amino acids with abundant hydrophobic residues distributed periodically around each alphahelix. Therefore, the two chains generate a stable coiled-coil geometry, in agreement with results based on analytical ultracentrifugation (Parry et al., 2007). Segment 2A (residues 264–282) is the shortest and the least flexible among all segments. It assumes the configuration of a nearly parallel alpha-helical bundle, in agreement with earlier suggestions (Parry et al., 2007). Segment 2B with 115 amino acids (residues 291–405) features an α-helical coiled-coil geometry for the major segment, and a stutter region in the vicinity of residue 349. In the stutter region, the two α-helical chains unwind and give rise to a much longer coiled-coil pitch, resembling two parallel α-helices in that region (see Fig. 2.4B, region marked in blue). This regions is part of a segment that has already been crystallized, which also shows the formation of the stutter region (Brown et al., 1996; Strelkov et al., 2001), confirming our predictions. The left end of the 1A segment connects to the head domain, while the right end of the 2B segment connects to the tail domain (Herrmann et al., 1996), where these two flexible domains are found to be poorly structured, in agreement with earlier suggestions (Parry et al., 2007; Strelkov et al., 2002). Linker L1 of 8 amino acids in length is among the softest regions in the structure, and facilitates the antiparallel assembly of the dimers into larger-scale filaments, where these linkers align with the L12 domain in a regular pattern (Parry and Steinert, 1999). Linker L12 forms a β-sheet structure in the dimer. An earlier sequence analysis has pointed out that the L12 domain region should form a small β-sheet of two chains, with one face of the β-sheet being apolar (Parry and Steinert, 1999). Our simulation confirms this hypothesis. Linker L2, which always features 8 amino acids in length for all IFs, results in a transition between two rod-like segments (Parry and Steinert, 1999).

### 2.2.2 Effect of solvent model

The solvent environment plays an important role in the structure, dynamics, and biological function of biomolecules. It is generally agreed upon that an explicit solvent model provides the most accurate treatment of solute-solvent interaction (Nymeyer and Garcia, 2003), because each explicit solvent molecule reflects its realistic chemical structure and resulting interactions with the solute and one another. Many models have been developed to simulate water, including SPC, TIP3P, TIP4P, TIP5 *et al.*. Those models have different degree of freedom and different distribution of charges to model the polarization effect. Their differences have been investigated in literature that will not be discussed here. Since the parameters for protein, nucleic acid and lipid in CHARMM force field are developed initially according to the TIP3P model, making which the best model for CHARMM force field. However, the approach of relying on an explicit treatment of solvent molecules significantly

increases the system complexity by several orders of magnitude. To achieve a better balance of computational efficiency and physical accuracy, implicit solvent models have been proposed as an alternative approach (Lazaridis and Karplus, 1997; Lazaridis and Karplus, 1999). Implicit solvent models add the effective solvent energy functions to the biological molecule, in terms of functions of the molecular structure and its conformation. Multiple implicit models are available for protein simulation, including methods based on the solvent accessible surface area (including Poisson-Boltzmann model, Generalized Born model (Fogolari et al., 1999) and GBSA model (Spassov et al., 2002)) and fast solvation model such as EEF1 model (Lazaridis and Karplus, 1997; Lazaridis and Karplus, 1999) which has been applied in the last subsection. This implicit solvent model is based on a Gaussian-shaped solvent exclusion to consider the solvent effect on protein surface. This method is very efficient that is only 50% slower than an in-vacuum simulation, but it has been successfully applied to study many protein structures.

This strategy simplifies the numerical effort of simulating the physical system of interest and thereby speeds up the simulation by averaging the solvent effect. Since no frictional effects are included in implicit solvent methods, such models can facilitate a more rapid structural organization toward the equilibrium geometry due to lack of viscosity imposed by explicit water molecules. This effect can be advantageous in structure identification approaches (Best et al., 2007; Paci and Karplus, 1999; Paci and Karplus, 2000) (such as in the study reported in (Qin et al., 2009b)) since it accelerates the sampling of molecular configurations. More configurations are visited per simulated unit time. Whereas the approach of using implicit solvents is computationally efficient, it has been argued that the implicit model may sometimes overestimate some energy components and lead to inaccurate results, in particular regarding the secondary structure of protein (Zhou and Berne, 2002). Therefore, further validation and comparison against explicit solvent models is required to ensure the validity of the result obtained from implicit solvent simulations. To address these issues, a detailed comparison between implicit and explicit simulation models is provided here, applied specifically to a vimentin intermediate filament dimer and tetramer.

We use the CHARMM22 force field implemented by the explicit TIP3P water model and run simulation with NAMD package (Nelson et al., 1996). Our model starts from the equilibrated structure obtained by using the implicit solvent model described above. All the simulations run in a NPT ensemble under a constant temperature (300 K) and constant pressure (1 atmosphere) controlled by Langevin thermostat and barostat. We use the particle mesh Ewald (PME) method in calculating the electrostatic interactions, with a grid size of 1 Å in all three directions. A cutoff length of 10 Å is applied to the van der Waals (VDW) interactions and to switch the electrostatic forces from short range to long range forces.

We begin with a comparison of the equilibrated vimentin dimer and tetramer geometries as obtained from implicit and explicit solvent simulation. Fig. 2.5A shows snapshots of the molecular structure of the vimentin dimer, displaying the characteristic segmented geometry with coiled-coil regions connected through linkers. The figure presents a comparison of the structure based on implicit solvent equilibration and explicit solvent equilibration, where the two geometries are superimposed. Fig. 2.5A also shows detailed views of key domains in the protein structure. It is seen that the linker L12 forms a parallel beta-sheet in both explicit and

implicit solvent models. We find that in both cases the total length of the dimer without the head and tail domain is ≈49 nm. This result is in agreement with experimental results where a range of 46–49 nm has been reported (Mucke et al., 2004b; Sokolova et al., 2006). The visual comparison of the dimer structure between implicit and explicit solvent models shows that the overall geometry of the dimer is stable in either solvent model.

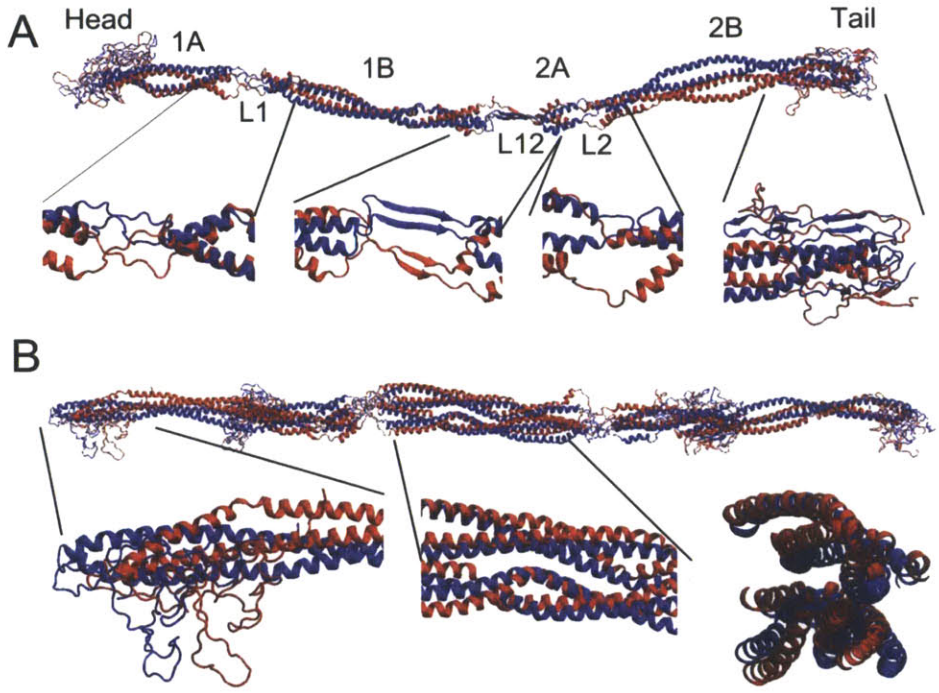


**Fig. 2.5 Structure of the vimentin intermediate filament dimer (panel A) and tetramer (panel B) (Qin and Buehler, 2010a).** The overlapped snapshots depict a comparison between implicit and explicit solvent simulation results.

By comparing the two structures, we find that the 2A segment (parallel helices) and L12 (beta-sheet) are only marginally stable, because the 2A segment lacks the hierarchical structure in enforcing its strength, and short beta-sheet segments are more energy favorable as well as better for protein flexibility (Keten and Buehler, 2008a). Fig. 2.5B shows a comparison of the vimentin tetramer structure of the implicit solvent equilibration and explicit solvent equilibration results, where the two geometries are superimposed. The total length of the tetramer is ≈60 nm with a slightly smaller length of ≈59 nm in the explicit solvent case. These findings agree well with the length of unit length filaments observed in experiment, 62 nm at pH 7.5 (Mucke et al., 2004b). In both cases the overlap part of the tetramer has a length of ≈36 nm, agreeing with the experimental value (30–36 nm) (Mucke et al., 2004b; Sokolova et al., 2006). Segments 1A, 1B and 2A are fully contained in this overlapped part, but the 2B segments in the immediate vicinity of the two terminals are located completely outside. We find that the head segment of each dimer is coiled around the other dimer, increasing the contact surface area and thereby providing enhanced interdimer interactions, as shown in Fig. 2.5B. The structure of the coiled-coil dominated overlap region is rather stable. As for the dimer case discussed in the previous paragraph, here we also present a detailed analysis of the structural character of the equilibrated protein in Fig. 2.5B.

The analysis shows that in comparison with the dimer case, the tetramer structure is more stable, and most of the structural features are well conserved in explicit solvent equilibration. We analyze the structure of the dimer and tetramer by calculating the dihedral angle distribution as shown in the Ramachandran map (Ramachandran et al., 1963) as depicted in Fig. 2.6.

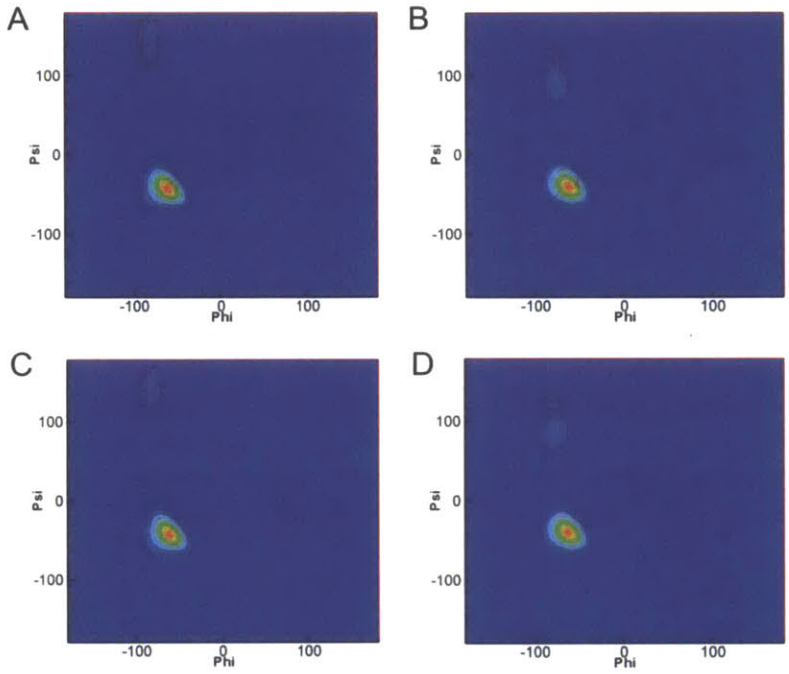


**Fig. 2.6 Ramachandran maps that show the averaged dihedral angle of each amino-acid ([$\varphi, \psi$]) distribution during the equilibrium process, comparing implicit and explicit simulation results (Qin and Buehler, 2010a).** Panels A and B show the results for the dimer in explicit solvent and implicit solvent, respectively. Panels C and D show the results for the tetramer in explicit solvent and implicit solvent, respectively. The analysis shows that most of the residues (≈73%) belong to the left lower corner ($\varphi$<0°, $\psi$<0°), and the peak value emerges at [$\varphi$≈−58°, $\psi$≈−47°]. This data shows the characteristic of a right-handed alpha-helix. Most other residues (≈25%) belong to the left upper corner ($\varphi$<0°, $\psi$>0°), and there is a much less intense peak that resembles the character of a beta-sheet in a Ramachandran map (−180°<$\varphi$<−50° and 50°<$\psi$<180°). The position of this peak center for the dimer/tetramer structure in implicit solvent ([$\varphi$≈−80°, $\psi$≈100°]) is slightly different from that of the explicit solvent ([$\varphi$≈−80°, $\psi$≈140°]), indicating that the beta-sheet in explicit solvent has a more extended conformation than that in implicit solvent.

This analysis shows the probability of specific dihedral angles [$\varphi$, $\psi$] of all amino acid residues in the dimer/tetramer structure in equilibrium. The analysis shows that most of the residues (≈73%) belong to the left lower corner ($\varphi$<0°, $\psi$<0°), and the peak value emerges at [$\varphi$≈−58°, $\psi$≈−47°]. This data shows the character of a typical righthanded alpha-helix. Most other residues (≈25%) belong to the left upper corner ($\varphi$<0°, $\psi$>0°), and there is a much less intense peak that resembles the character of a beta-sheet in a Ramachandran map (−180°<$\varphi$<−50° and 50°<$\psi$<180°). The position of this peak center for the dimer/tetramer

structure in implicit solvent ([$\varphi \approx -80°$, $\psi \approx 100°$]) is slightly different from that of the explicit solvent ([$\varphi \approx -80°$, $\psi \approx 140°$]), indicating that the beta-sheet in explicit solvent has a more extended conformation than that in implicit solvent. We further calculate the number of H-bonds in the dimer and tetramer structure during equilibration. We observe that the number of H-bonds in both the dimer and tetramer structure decreases after energy minimization and converges asymptotically to a constant value in explicit solvent, as shown in Fig. 2.7. The asymptotic number of H-bonds is also stable for the simulations in implicit solvent, as shown in Fig. 2.7A and B. By subtracting two times the number of H-bond in the dimer from that of the tetramer, we estimate the number of inter-dimer H-bonds, which varies with time as shown in Fig. 2.7C. The asymptotic value by the end of the simulation (by averaging over the last 20% of the total simulation time) is given in Fig. 2.7D, where it is observed that the number of inter-dimer H-bonds in explicit solvent (145±5) is greater than that obtained in implicit solvent (78±8), indicating that the interaction between two dimers in explicit solvent might be stronger than that of the implicit solvent.

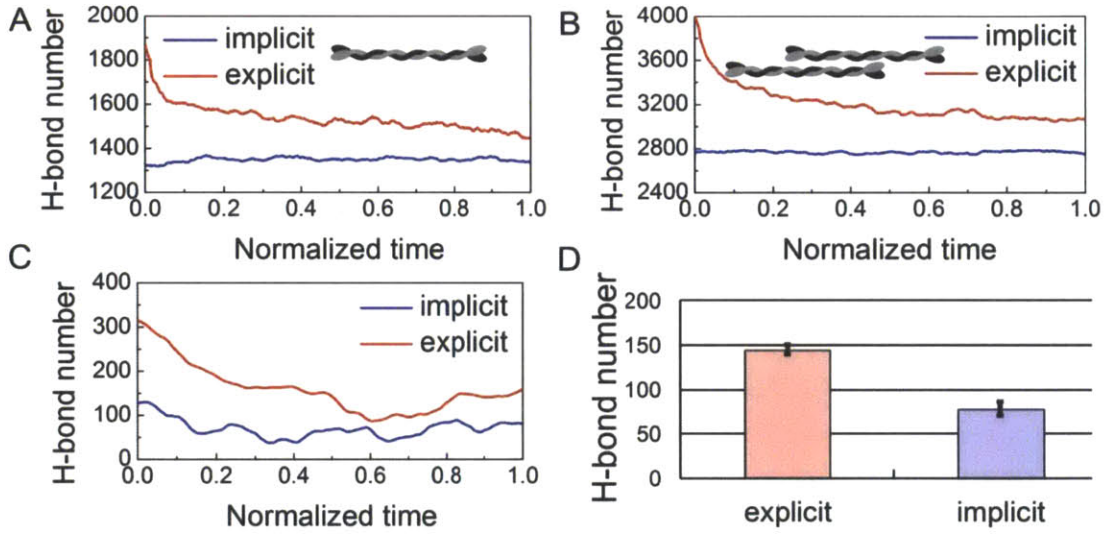


**Fig. 2.7 Number of H-bonds of the vimentin intermediate filament dimer and tetramer, showing a comparison between implicit and explicit solvent simulation results (Qin and Buehler, 2010a).** Panel A: Number of H-bonds in a dimer. Panel B: Number of h-bonds in a tetramer. Panel C: Number of H-bonds between the two dimers within a tetramer. Each of the panels A, B and C are obtained during the equilibration process, in both implicit and explicit solvent, respectively. Panel D: Comparison between the asymptotic values of the number of interdimer H-bonds in both implicit and explicit solvent. The main bar gives the average value during the last 20% of the total simulation time while the corresponding error bar corresponds to the standard deviation. The simulation time is normalized by the length of the total equilibration (10 ns for the implicit solvent for both dimer and tetramer, 16 ns for the explicit solvent for the dimer, and 19 ns for explicit solvent simulations for the tetramer).

Based on molecular simulations, we have analyzed and compared the structure properties of the vimentin dimer and tetramer in implicit and explicit solvent models. In implicit solvent, a long time equilibration was performed in earlier studies reach a minimum

energy state. A continued equilibration in explicit solvent as reported in this section for up to 20 ns reveals that the structural model developed earlier (Qin et al., 2009b) appears to be stable also in explicit solvent. The analysis of Ramachandran maps as reported in Fig. 2.6 provides important insight into structural parameters in implicit vs. explicit solvents, and could perhaps be used as a method to compare against similar experimental data. The detailed analysis of the number of H-bonds within each dimer and the tetramer reveals some differences between the two models, suggesting that the explicit solvent model tends to feature a greater H-bond density.

However, it should be noted that the analysis reported here has limitations, in particular with respect to accessible time scale. Accurate calculations can only be performed starting from an equilibrated or near-equilibrated structure, and the simulation time must be sufficient to include sufficient possible conformations that represent a reasonable sampling of the conformation space. The use of explicit solvents in particular is computational very expensive. In light of these limitations, the implicit solvent calculations show advantages in terms of efficiency at sufficient levels of structural and energetic accuracy.

### 2.2.3 Coarse-grained model

The protein dynamics revealed by simulation in explicit solvent condition provides an accurate description of how the protein changes its conformation toward the state with lower free energy. However, the final equilibrated structure greatly depends on the initial conformation as the initial structure is easy to get trapped at a merely local energy minimum while the global energy minimum is reached by crossing energy barriers. This fundamental mechanism causes the conformation change difficult to happen for classical full atomistic simulations. The energy barrier for breaking of a single hydrogen bond is estimated to be about 6.2 kcal/mol (in CHARMM force field). The time span to observe an structure change can be theoretically estimated by $\tau_0 \exp\left[\Delta G/(k_B T)\right]$ basing on the Bell model (Ackbarow et al., 2007; Qin and Buehler, 2010c), where $\tau_0 \approx 0.1$ ps is the reciprocal of a natural frequency of solids, $\Delta G = 6.2$ kcal/mol is the energy to cross for conformation change, $k_B$ represents the Boltzmann constant and $T$=300 K is the sampling temperature. It yields that at least 3 ns is necessary for observing this single-step conformation change (defined by the rupture of a single H-bond). This explains why the overall structure change can only be observed over a long time.

The use of other methods, such as replica exchange simulations or coarse-grained approaches could be explored to provide an additional comparison with the results obtained here, for example to reach a better sampling of structural configurations at long timescales. Here we report a simulation of the vimentin tetramer using a coarse-grained model with explicit water, as shown in Fig. 2.8A, where the initial geometry is based on the result of the full atomistic model at equilibrium. The initial coarse-grained geometry is generated from the full atomistic model of the tetramer (after the structure prediction process). Each amino acid is represented by one to five beads, one of which is the backbone bead that is generated from the coordinate of the residue backbone and the rest of which are side-chain beads that are generated from the coordinate of the residue side chain. Every four water molecules are represented by a bead. The coarse-grained dimer and tetramer structures are further

equilibrated by using MARTINI force field (Monticelli et al., 2008) in explicit water model. We use a 40 femtosecond time step in this coarse-grained model, and the same constant temperature and pressure as in the full atomistic model. This coarse-grained model enables us to reach time-scales of hundreds of nanoseconds to microseconds.

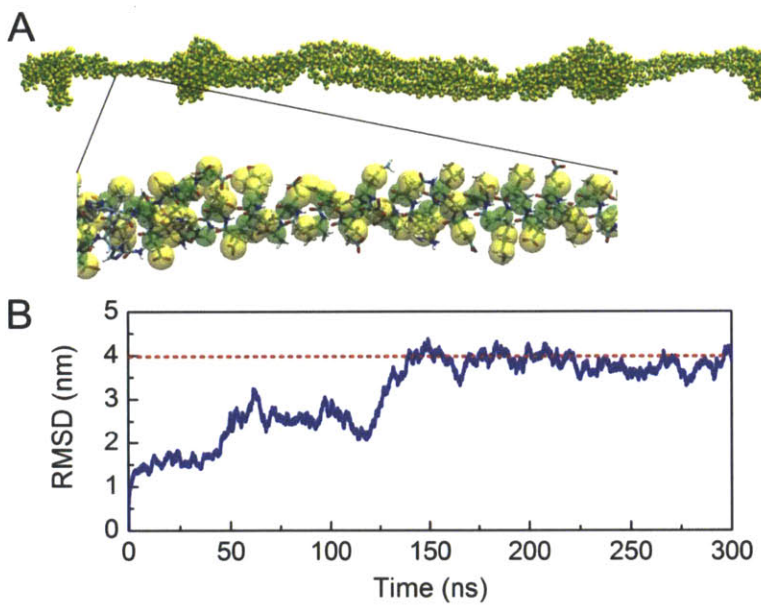


**Fig. 2.8 Coarse-grained representation of the vimentin tetramer (Qin et al., 2009b).** Its structural stability is given during time-scales of hundreds of nanoseconds (RMSD analysis in panel B).

An analysis of the structural evolution of the tetramer in this coarse-grained representation provides further evidence for the stability of the predicted structure at long time-scales of hundreds of nanoseconds, as confirmed in the analysis shown in Fig. 2.8B. The structure is stable with the coarse-grained representation, providing evidence that the results are reliable, despite variations in the model representation.

### 2.2.4 Large-scale parallelized computing

Our simulations are carried out in Linux-based clusters in MIT and supercomputers (of Teragrid, a computing network for the purpose of computationally intensive science). Software including CHARMM and NAMD are compiled in those platforms based on FORTRAN and C compilers as well as High-performance and Portable MPI (MPICH).

For the equilibration of vimentin dimer and tetramer in implicit solvent for 60 ns, we used 4 CPUs (Xeon) that run for 50 days in parallel. There are 15,000 atoms in the dimer model, as well as 30,000 atoms in the tetramer model.

For the equilibration of vimentin dimer and tetramer in explicit solvent for about 20 ns, we used 64 CPUs that run for ~25 days in parallel. There are 265,000 atoms in the dimer model, as well as 507,000 atoms in the tetramer model.

For the coarse-grained model of vimentin dimer and tetramer in explicit solvent for about 300 ns, we used 32 CPUs that run for several days in parallel. The coarse-grained system includes 43,801 particles (4,052 for the protein plus 39,749 for water molecules). The number of particles in the coarse-grained model is 1/11 of the full atomistic representation.

Both explicit and implicit model simulations yield stable structures what do not collapse or unfold, showing that the structure has been build in a rational way.

## 2.3 Validation of vimentin structures and update according to experiments

The average diameter of the cross section of the dimer is $d_{\mathrm{dimer}} \approx 2$ nm, and the average diameter of the tetramer is measured to be $d_{\mathrm{tetramer}} \approx 3.6$ nm, in close agreement with experimental measurements of 3.4 nm (Sokolova et al., 2006) (the small difference may be caused by the interaction with other dimers in larger filaments that contain many dimers, which may lead to increased compaction of the structure). Based on these geometric measurements we estimate that the diameter of a non-compacted unit length filament is $d_{\mathrm{ULF}} \approx 18.3$ nm, which is closely within the range measured in experiment, where values of 16–20 nm have been reported (Herrmann et al., 1999). For compacted vimentin IFs we predict a diameter of $d_{\mathrm{IF,mature}} \approx 11.2$ nm, which is in excellent agreement with various experimental reports of values in the range of 10–12 nm (Fudge et al., 2003; Herrmann et al., 1999). A summary of the structural comparison between simulation predictions and experimental results is shown in Fig. 2.9.

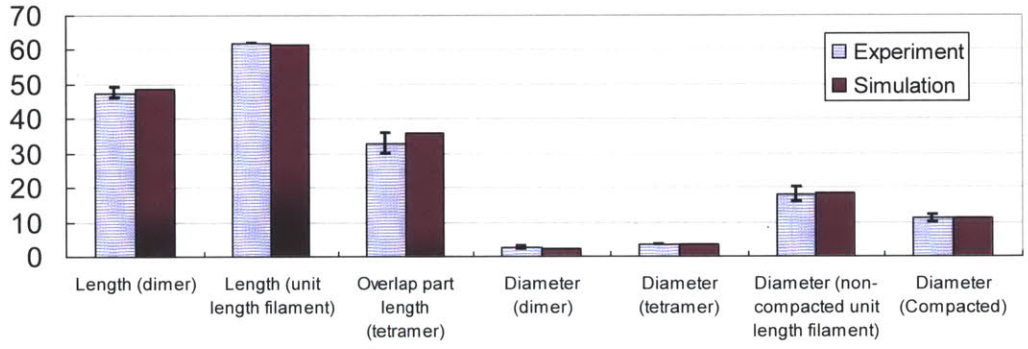


**Fig. 2.9 Comparison of structural properties of IF dimer and tetramer between experiment and simulation** (Qin et al., 2009b)**.**

Furthermore, we carry out an analysis of the radial distribution function (RDF) to determine local and medium range structural features and their comparison between the implicit and explicit solvent models. The RDFs are calculated using the "gofr" plug-in in VMD. It is noted that our analysis approach is the same as in reference (Jones et al., 2009). The RDFs are obtained by averaging over the last 100 ps of the equilibration runs in both cases. The results shown in Fig. 2.10 confirm that in both the two figures, the RDF peaks for our vimentin model is the same as that for the experiment result, which means the structure for the protein within two solvent features the same character. The first peak at 3.84 A is related to the character of the primary structure. The other four peaks for 5.00 Å, 5.46 Å, 6.15 Å, and 8.70 Å, respectively, denote the first, second, third and forth neighbors in the secondary and tertiary structures of the protein filament, respectively.

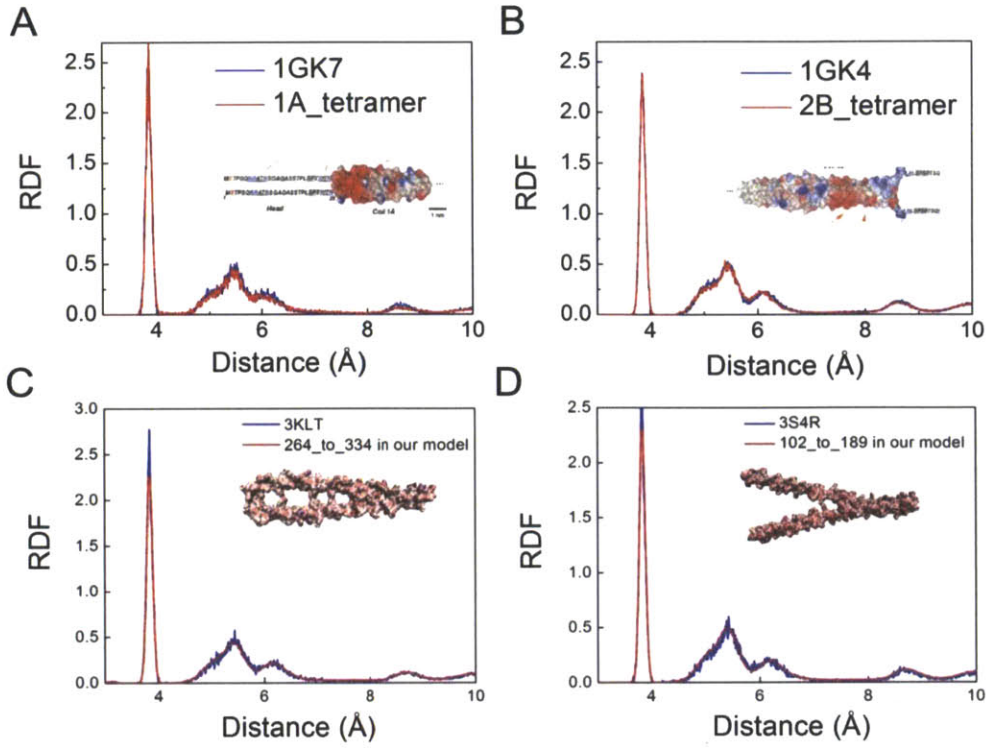


**Fig. 2.10 Comparison of RDF analysis between our model and experimental results.** For the coil1 segment (A and D), and for the coil2 segment (B and C).

We combine our dimer model with the most recent X-ray diffraction result to provide an atomistic structure of dimer with refined structures. We first combine two coiled-coil segments obtained directly from PDB to replace the coil2 domain of the structure. The N-terminal half of coil2 is obtained from vimentin segment that includes residues 264–335 (obtained from the PDB with identification (ID) 3KLT (Nicolet et al., 2010)). The C-terminal half of coil2 is obtained from the vimentin segment that includes residues 328–406 (given by PDB with ID 1GK4 (Strelkov et al., 2002)). The two segments are aligned to form an integrated coiled coil because both fragments include an overlapped region of residues 328–335. We use VMD to find the best fit between the backbone atoms of the overlapped region of the two segments corresponding to the overlapped part. The best fit provides a minimum root mean square deviation (RMSD) of 0.68 Å between the C-alpha atoms within the overlapped region of the two segments, which indicates that the two segments match well with each other. We use the same procedure to combine residues 153-238 (PDB with identification (ID) 3SWK (Chernyatina et al., 2012)) and residues 99-189 (PDB with identification (ID) 3S4R (Chernyatina et al., 2012)) to partially form the structure of coil1. Again, the best fit provides a minimum RMSD of 1.1 Å between the C-alpha atoms within the overlapped region (residue 153-189). We replace those corresponding parts in our vimentin dimer model by repeating the best fit method: for the head domain, we connect the coil1 to our dimer model by using the overlapped region of residue 106-120 and the RMSD yields 0.47 Å. For the right edge of 1B, we connect the combination of head domain and coil1 to this part (residue 210-237) and the RMSD yields 2.5 Å. There are still some domains

(head domain, left part of 1A, right part of 1B, L12 and tail domain) with uncertainty in their structures. Our structural homology method provides a frame to fill those segments revealed by X-ray diffraction method based on the concept of divide-and-conquer method. This combined vimentin structure as shown in Fig. 2.11, is the most up-to-date model as we know.

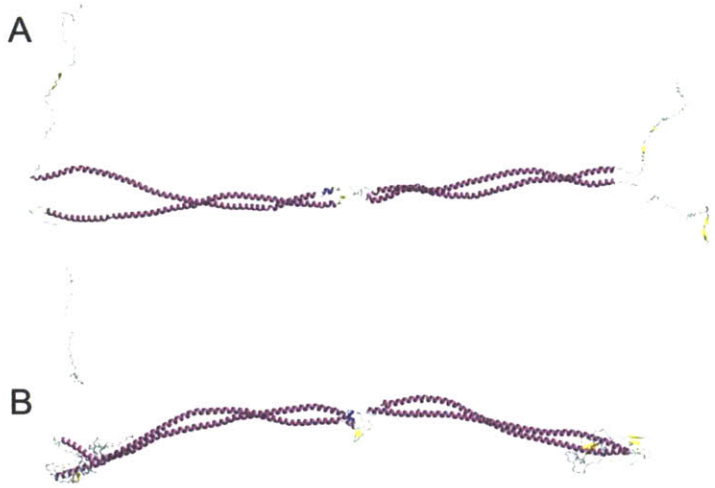


**Fig. 2.11 The updated vimentin dimer structure by combining the structural homology result with the recent X-ray diffraction result (Chernyatina et al., 2012; Nicolet et al., 2010).** Panel A: the initial structure before equilibrium; Panel B: the structure equilibrated in implicit solvent.

# 3 Mechanical property of intermediate filament subunits

Although there exists clear evidence that IFs play a key role in important physiological and pathological mechanisms, a molecular-level nanomechanical analysis of this protein structure remains unavailable. Earlier molecular dynamics studies have focused solely on a small section of the 1A and 2B domain (Ackbarow and Buehler, 2007; Zhang et al., 2008), without considering the properties of the whole dimer structure as shown in Fig. 2.4. Furthermore, recent experimental studies using atomic force microscopy (AFM) analysis focused on the mechanical properties of entire filaments (Kreplak and Bar, 2009b; Kreplak et al., 2008). However, the details of the underlying molecular mechanisms of deformation remain unknown, and no analysis has been reported at the level of individual dimers or tetramers. Here we carry out a series of systematic molecular dynamics simulations to probe the response of entire IF dimers and tetramers to mechanical tensile stretching. Specifically, the aim of our investigation is to elucidate the basis of their great extensibility and stiffening properties, as well as associated molecular deformation mechanisms of this protein material.

## 3.1 Background on the mechanical function of vimentin

Maniotis and coworkers demonstrated early that the IF network is involved in propagating mechanical stresses from the cell surface to the nucleus (Maniotis et al., 1997). However, it is shown only recently that the proteins responsible for the linkage between cytoskeletal IFs and the nuclear lamina have been identified, namely, Nesprin and SUN proteins (Ostlund et al., 2009; Wilhelmsen et al., 2005). Similarly, the involvement of the IF network in cell migration and especially the direct and indirect interactions between IFs and integrins have only been unveiled in the past few years (Bhattacharya et al., 2009; Kim et al., 2010; Schoumacher et al., 2010). The emerging picture is that the IF network is a major constituent of the cytoskeletal system. Still its response to mechanical stresses remain barely studied and the main evidence for the involvement of IFs in mechanotransduction comes from genetic diseases where IF proteins are mutated (Herrmann et al., 2007). Mutations in keratins, desmin and lamin A yield a wide spectrum of pathologies, some of which exhibit mechanical failure of the skin, skeletal muscles or heart muscles (Herrmann et al., 2007). In one case, in vitro measurements indicate that mutated desmin IFs have different mechanical properties than the wild-type ones, thus indicating that the impaired mechanotransduction is a molecular explanation for the observed pathologies (Kreplak and Bar, 2009b). Unfortunately, there have been no in vivo or cell studies performed to confirm this hypothesis. Most of the cell level studies on IF mutants have concentrated on their assembly properties (Bar et al., 2005) and their involvements in signal transduction pathways (Omary, 2009).

Several experimental approaches have been developed to characterize the mechanical properties of IFs from the single filament level to networks and cells. In this section we will focus on introducing three experimental methods, AFM, bulk rheology and particle tracking microrheology.

Single IFs are apolar materials as they need to assemble to form filaments (Kreplak et al., 2004a), and they can have close affliation with solid surfaces (Mucke et al., 2005). For this reason, optical tweezers approaches have not been successful in determining the elastic properties of single IFs. Instead, the AFM technique has been used extensively to determine the mechanical properties of single IFs. Imaging in liquid of vimentin IFs deposited on different surfaces yielded a 1 micron estimate for their persistence length (Mucke et al., 2004a). This result yields a Young's modulus of 8 MPa for this 10 nm wide filament by taking it as pure elastic cylinder. However IFs are composed of bundles of coiled coils, adding anisotropy to their mechanical properties. This fact means that their elastic properties have to be described by a stiffness tensor with at least a Young's modulus and a shear modulus. To measure these quantities, Guzman and coworkers imaged vimentin IFs, unfixed and fixed with a chemical crosslinker, suspended above the 200 nm pores of an aluminate membrane (Guzman et al., 2006). They measured the deflection of the vimentin filaments above the pores for different forces applied by the AFM cantilever on the surface. They obtained an estimate for Young's modulus around 1 GPa and an estimate for shear modulus around 2–3 MPa. Another application of the AFM is the controlled manipulation of nanostructures on surfaces (Falvo et al., 1997). During the manipulation, the AFM cantilever is submitted to a torque that provides an estimate of the force applied on the nanostructure during manipulation (Guthold et al., 2004). Kreplak and coworkers took advantage of this fact to measure the extensibility of several IFs (Kreplak et al., 2005) and the stress-strain curve of a single desmin IF (Kreplak et al., 2008). They observed a maximal extensibility of 250% associated with a nonlinear stress-strain curve above 100% extension. This method has been used successfully to detect nanomechanical differences in desmin filaments with point mutations associated with myofibrillar myopathies (Kreplak and Bar, 2009b).

The first demonstration that IFs have very different mechanical properties compared to actin filaments and microtubules comes from bulk rheological measurements (Janmey et al., 1991). The experiment revealed that a suspension of vimentin IFs can support shear strains of several 100% while hardening in the process (Janmey et al., 1991). Since this early work, bulk rheology has been applied to several IF types, including neurofilaments (Leterrier et al., 1996), vimentin (Lin et al., 2010a), desmin (Schopferer et al., 2009), keratins K5/K14 (Ma et al., 1999) and K8/K18 (Yamada et al., 2003). Most measurements are taken at low frequency, around 1 Hz, and low shear strains, 1%–5%, and provide an estimation of the elastic properties of the IF network as a function of the protein concentration (Lin et al., 2010a; Ma et al., 1999; Yamada et al., 2003). Experiments performed over a large frequency range, from 10 to $10^4$ Hz, reflect the persistence lengths of the filaments within a network. In the case of desmin, a value of 900 nm was obtained in comparison to 400 nm for vimentin (Schopferer et al., 2009). Since IF networks have nonlinear rheological properties, varying the amount of stress or strain could provide additional information. Using a pre-stress method where a small oscillatory stress is applied in addition to a constant stress, Lin *et al.* characterized the nonlinear property of a vimentin network in the presence of magnesium ions (Lin et al., 2010a). Above a given pre-stress, the measured differential modulus varies as pre-stress exponent (3/2) can be explained by the straightening of nonextensible filaments (Lin et al., 2010a). However at very large pre-stresses, vimentin networks in presence of magnesium ions behave differently due to the extensibility of the filaments (Storm et al., 2005). This

method is also applicable for understanding the mechanical properties of network of mixed biological materials, for example, IFs and actin (Esue et al., 2006), or actin and microtubules (Pelletier et al., 2009). It would be interesting to know how IFs contribute to the rheological properties of those composite network materials.

Another way to measure the local viscoelastic properties of IF network is by using the particle tracking microrheology (Wirtz, 2009). Microspheres, such as polystyrene, are embedded in the network and are optically tracked by video microscopy. The trajectory of the spheres can be analyzed according to the function of Brownian motion of a particle in a viscoelastic medium. This technique allows the measurement of both the local elastic modulus of vimentin networks and their local density (Koster et al., 2010), as well as their local rheological properties within cells. In an experiment, the epithelial cells were treated with detergent and high salt to prepare intact keratin networks, making them suitable for particle tracking microrheology measurements (Sivaramakrishnan et al., 2008). These measurements revealed different elastic moduli and network density at the cell periphery and at the perinuclear region (Sivaramakrishnan et al., 2008). Moreover, their study shows that the application of shear stress prior to cell treatment can induce keratin network rearrangements and thus make an homogeneous distribution of network density across the cells (Sivaramakrishnan et al., 2008).

## 3.2 Nanomechanics of vimentin dimer and tetramer

IFs form hierarchical structures, ranging from dimers, tetramers, unit length filaments, and full-length filaments to the cellular scale. The IF dimers and tetramers represent the most fundamental building block. Here we present a series of systematic molecular dynamics simulations to probe the response of entire IF subunits to mechanical tensile stretch.

### 3.2.1 Steered molecular dynamics--the *in silico* stretching simulation method

In experiments, microscopic tensile tests including optical tweezers and AFM are tools that are usually applied to studying the elastic property and strength of protein nanostructures. Those tools are able to stretch the protein and record the force-extension relationship during the entire stretching process. Such stretching experiment usually gives a characteristic sawtooth pattern of spaced peaks that result from the sequential unfolding of its micro structures (Oberhauser et al., 2002). In computational simulations, SMD technique, which has the basic idea to apply external forces to one or more atoms in the protein model, are usually applied to studying the behavior of the protein structure under stretching. This method largely mimicks the process of experimental stretching with AFM. Fig. 3.1 gives an example of the unfolding of the modular protein titin I27 (Marszalek et al., 1999). By comparing the force-extension curve from AFM (Fig. 3.1A) and the conformation change obtained in SMD simulation, it can be predicted that the mechanical resistance in this module arises from a patch of six hydrogen bonds bridging the A' and G strands, and the hump region is caused by the hydrogen bonds between A and B strands (Fig. 3.1B) (Marszalek et al., 1999). They further verify this by introducing a point mutation to break the interaction between strand A and B and a difference force-extension curve is obtained as expected. This SMD method is

helpful and promising to find the relationship between mechanical and micro structural properties of protein structures (Sotomayor and Schulten, 2007). This relationship, which is hard to obtain by only AFM tests, is important to reveal the deformation mechanism of protein structures, as well as to predict the properties after mutation.

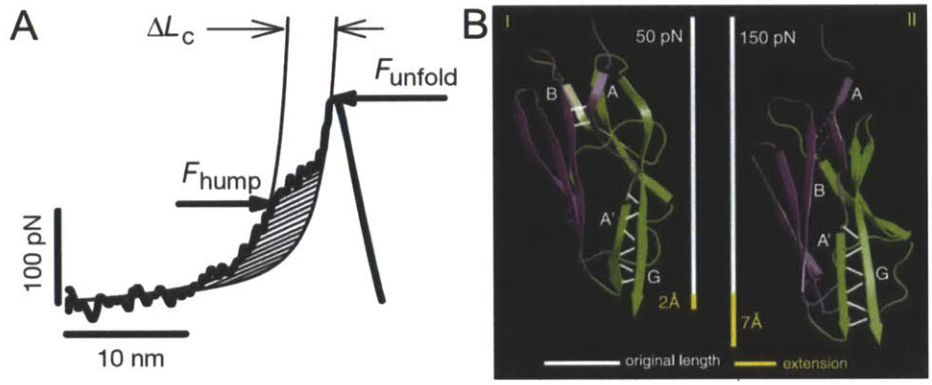


**Fig. 3.1 Titin I27 and its elasticity (Marszalek et al., 1999).** Panel A: the force extension curve of Titin I27 obtained via AFM stretching. Panel B: the cartoon representation of I27 model before and after stretching in SMD simulations. This figure is reproduced from (Marszalek et al., 1999) with permission.

Here, to investigate the mechanical property of IF dimers and tetramers, we apply the boundary condition as follows. The $C_\alpha$ atoms at the end of two 2B segments are pulled on by using an SMD spring (harmonic with a force constant of 10 kcal/mol/Å$^2$), while the other end of the subunit is fixed, as shown in Figs. 3.2A and B for a dimer and tetramer, respectively. As illustrated in Fig. 3.2C, this simulation set up mimics the AFM experiment in applying force on the filament, the SMD spring is elastic to decrease the fluctuation of the stretching force as well as avoiding artificial impact force applied on the protein structure. The pulling force $F$ is recorded versus the position of the spring. The simulations are carried out at pulling velocities ranging from 0.0001 Å/ps to 1 Å/ps. We record the force-extension curve from steered molecular dynamics simulation and analyze the mechanical properties by computing the engineering strain defined as $\varepsilon = \Delta L/L_0$, where $L_0$ is the initial length of the filament and $\Delta L$ is the extension.

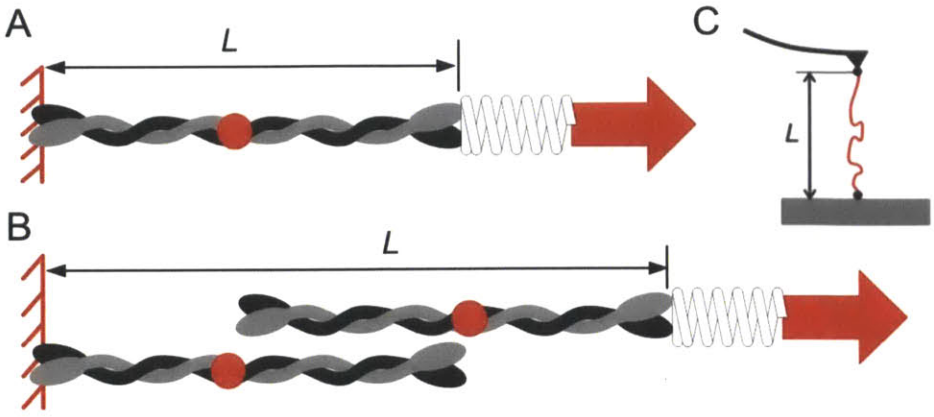


**Fig. 3.2 Schematic of the pulling geometry and implementation of mechanical tensile**

**test on dimer (A) and tetramer (B) (Qin et al., 2009a).** This simulation set up is based on the AFM test on protein materials (panel C).

### 3.2.2 Tensile response of vimentin dimer

The dimer structure is stretched until all helical domains are fully extended. Fig. 3.3 shows the force-strain curves of the dimer at a constant pulling rate of 0.01 Å/ps, and the structural character of the dimer is given in Fig. 3.4.

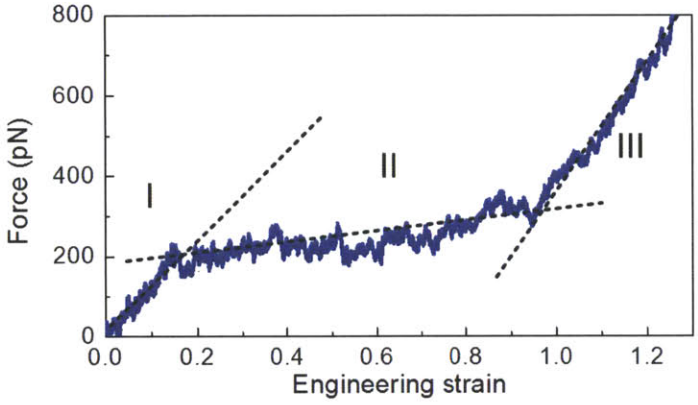


**Fig. 3.3 The force-strain curve of the dimer under stretching for constant pulling rate (0.01 Å/ps) (Qin et al., 2009a).**

The simulations reveal three distinct regimes of deformation. In the first regime (I), the pulling force increases linearly with strain until it reaches an angular point, where a dramatic change in the slope emerges (the angular point corresponds to the point where the first unfolding in the protein occurs). Within this region, no rupture or domain unfolding is observed until the applied strain is higher than 12%. In the second regime (II), the force-strain curve resembles a plateau regime where the pulling force remains almost constant. It is found that unfolding of all alpha-helical domains occurs in this regime. For this region, 2A segment begins to uncoil first, and other segments start to uncoil in sequence. We observe that the uncoiling of alpha-helical structures occurs simultaneously with the formation of betasheet protein domains, a phenomenon referred to as $\alpha - \beta$ transition. With this structural transition, the back bones of both strands start to align with the pulling direction. In the third regime (III), the stretching force increases rapidly as the strain increases, indicating a significant stiffening of the local (tangent) elastic properties. This is caused by pulling the unfolded polypeptide backbone of the protein, where the stretching of covalent bonds leads to a much increased stiffness, as shown in Fig. 3.4, of the strain beyond 95%. The overall characteristics of the force-strain curves of the dimer share similarities with stretching of individual alpha-helices (Ackbarow and Buehler, 2007; Ackbarow et al., 2007) as well as with myosin coiled-coil structures (Schwaiger et al., 2002). Regime (II) represents the main unfolding regime, where the average force in this regime approximates the protein's unfolding force. The slight increase of the force in this regime II (approximately 1.079 pN for 1% strain, as shown in Fig. 3.3) is due to the fact that as more convolutions in the alpha-helical protein are unfolded, a larger rupture force is required (since the failure probability is decreased for a smaller number of remaining convolutions (Bertaud et al., 2009)). It is noted that in experimental and simulation studies of the myosin coiled-coil

protein, the strain-force curve shows a very similar behavior, and the same level of unfolding force (Root et al., 2006).

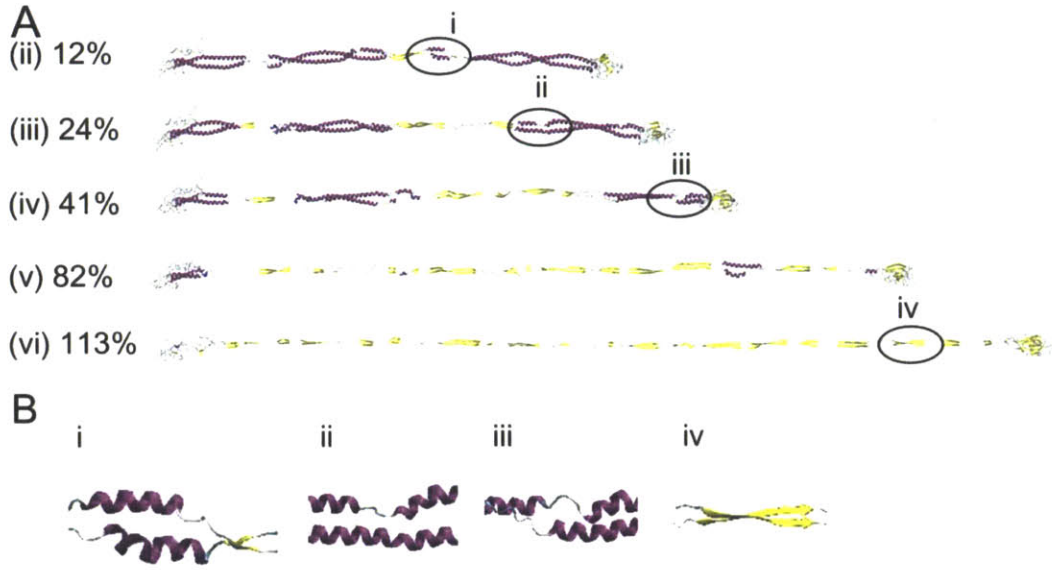


**Fig. 3.4 Simulation snapshots during pulling of the dimer at different pull strain (A) (Qin et al., 2009a).** Panel B shows detailed views of the molecular structure at various levels of strain.

Calculation of the Young's modulus for small deformation (calculated in the pre-angular point regime (I) shown in Fig. 3.3, where the dimer is deformed homogeneously before unfolding sets in) leads to values in the range of 380–540 MPa. This is in close agreement with experimental results from corresponding vimentin IF bending experiments, which show moduli in the range of 300–900 MPa (Guzman et al., 2006). This agreement supports the notion that IFs could be considered as a continuous body in the very small deformation regime where no unfolding or sliding occurs between individual dimers. Fig. 3.5 summarizes the unfolding history of each domain in tension. We observe that the 2A segment ruptures first at 12% strain, and the reason may be that while the other three segments are coiled coils, the 2A segment is essentially a parallel alpha-helical bundle, which has a lower mechanical stability against tensile stretch (Parry, 2006; Parry et al., 2007). Once the 2A segment is fully uncoiled at ~20% strain, the segments 1B, 1A and 2B begin to uncoil sequentially. This unfolding sequence is highly repeatable. This character could play an important role in biomechanical signaling pathways, where specific levels of strain may correspond to particular changes in the molecular structure. Thereby the unfolding of specific domains might induce biochemical signaling, which may be part of the coupling between deformation state and biological processes.

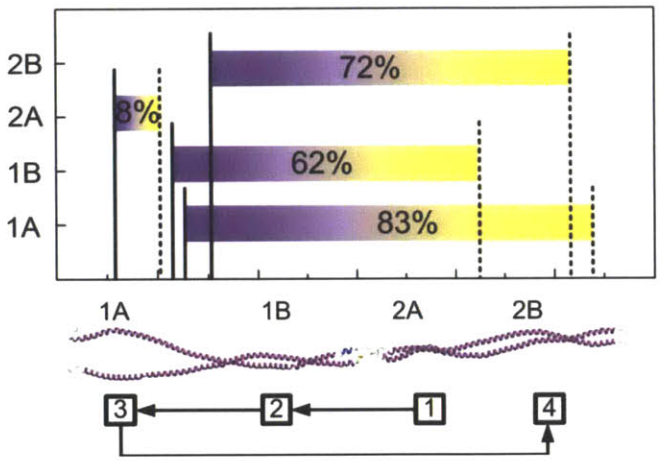


**Fig. 3.5 Unfolding history maps for the dimer as it under tensile deformation for increasing strain (Qin et al., 2009a).**

### 3.2.3 Tensile response of vimentin tetramer

We continue with an analysis of the tetramer mechanical properties. Fig. 3.6 shows the complete force-strain curves of a vimentin tetramer under stretching. The simulations reveal four distinct regimes. In the first regime (I), the pulling force increases linearly with the strain until it reaches the angular point, and we do not observe unfolding phenomenon before overall 10% strain. In the second regime (II), the force-strain curve forms a plateau, where the pulling force keeps almost constant, which is similar to the case of the deformation properties of the dimer. From simulation snapshots in Fig. 3.7A, we find that the 2B segments unfold first, starting from the stutter location, then expand throughout the entire segment. In the third regime (III), we observe a significant transition in the force-strain behavior. During this transition, the pulling force changes from the low-force plateau (~1 nN) to a peak value of 7.3 nN, marking the onset of the final regime (IV). Beyond the peak value, the force in regime (IV) is rather bumpy and its level begins to decrease with the increasing strain.

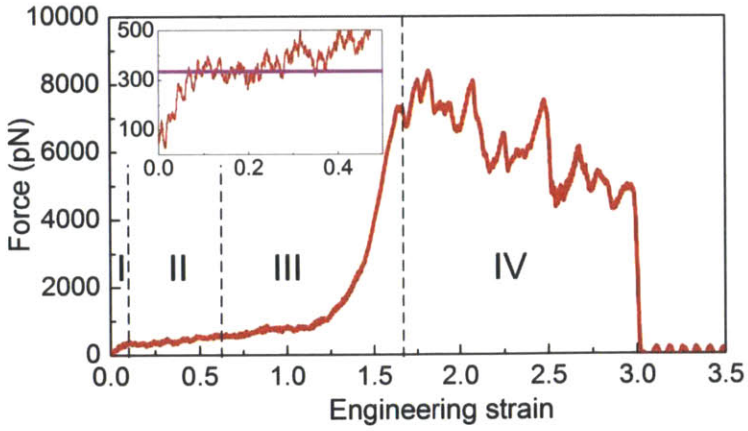


**Fig. 3.6 The force-strain curve of the dimer under stretching for a constant pulling rate (0.1 Å/ps) (Qin et al., 2009b).**

The force plateau observed in Fig. 3.6 relates to the stepwise unfolding of the coiled coil segments. We observe that at the end of the plateau regime, the tetramer behaves differently

from the dimer. The overlapped part in center begins to uncoil (Fig. 3.7A), and the pulling force approaches a much broader transition region, where the structure becomes significantly stiffer and eventual fails by interdimer sliding. The sliding process is composed of many rupture events of hydrogen bonds, that is why the stretching force is much bumpy. The two dimers are completely detached at ≈300% strain (Fig. 3.7). The comparison between the dimer and tetramer reveals a significant difference in the mechanical behavior.

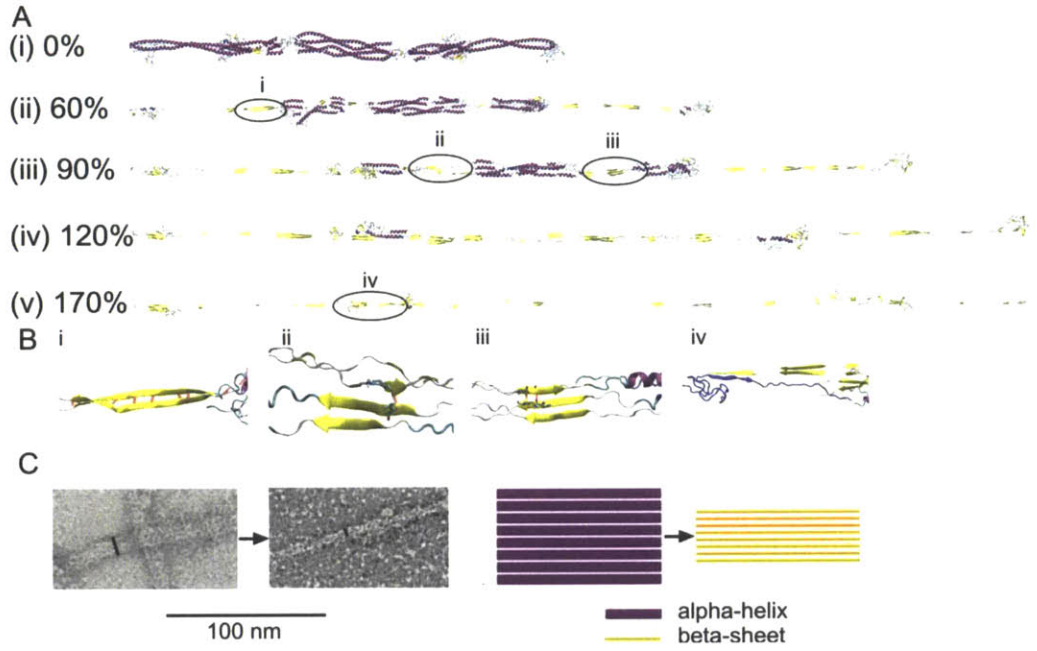


**Fig. 3.7 Simulation snapshots during pulling of the dimer at different pull strain (A) (Qin et al., 2009b).** Panel B shows detailed views of the molecular structure at various levels of strain. Panel C shows the experimental evidence that alpha-beta transition takes place during stretching.

The stretching study of the tetramer indicates that the deformation of IFs involves the α−β transition and subsequent sliding (Qin and Buehler, 2010c). This conclusion suggests that significant filament thinning should occur during stretching. Indeed, this behavior has been observed experimentally in atomic force microscopy and electron microscopy studies of desmin IFs (Kreplak and Bar, 2009b; Kreplak et al., 2008) as shown in Fig. 3.7C, being in qualitative agreement with our predictions. The experimental evidence for microstructure transition in IFs under stretching is based on a small angle X-ray diffraction study of stretched hard alpha-keratin fibers (Kreplak et al., 2002). We extensively discuss the mechanism of this structural transition in the next subsection.

### 3.2.4 Secondary structure transition induced by mechanical force

Alpha-helices and beta-sheets are major secondary structural motifs that organize the three-dimensional structure of proteins (Brändén and Tooze, 1999). Whereas the sequence of amino acids defines a protein's specific secondary and higher level structures (Minor and Kim, 1994), the transition between alpha-helices and beta-sheets (referred to as α-β transition) has been observed universally for a broad range of α-helix based protein filaments. The α-β

transition was observed under variations of pH (Koga et al., 2003), temperature changes (Ding et al., 2003), and solvent composition alterations (Meier and Seelig, 2008), and under mechanical deformation as shown by experiment and simulation (Church et al., 1998; Fudge et al., 2003; Kreplak et al., 2008; Kreplak et al., 2004b; Qin et al., 2009b). Indeed, many α-helix rich proteins are crucial for structural support, in mechanotransduction and cell motility, and in defining the cell's stretchiness. Experimental studies revealed that α-keratin (Church et al., 1998; Kreplak et al., 2004b) (found in wool, hair and hooves), hagfish slime threads (Fudge et al., 2003), desmin (Kreplak et al., 2008) and vimentin (Qin et al., 2009b), all display a α-β transition under deformation. It was found that the transition significantly thins the filament, but toughens and strengthens it at large deformation (Qin et al., 2009b). Furthermore, the α-β transition may also have important implications for diseases related to amyloid formation (*e.g.* Alzheimer's, Type II Diabetes, or Parkinson's), where native proteins convert to β-sheet rich amyloid structures (Daidone et al., 2004; Gross, 2000).

The experimental observation of this phenomenon for a variety of proteins suggests that the α-β transition under stretching is a universal mechanism of deformation, and as such is crucial for providing a link between a protein material's hierarchical structure and its mechanical response (Buehler and Yung, 2009). The understanding of the α-β transition in protein materials is similarly important as studies of dislocation nucleation and propagation in metals or ceramics, which present the fundamental unit deformation mechanism in crystalline materials. However, compared to dislocations (for which much progress has been made and relatively good models exist), the understanding of deformation mechanisms in protein materials remain poorly understood. What is the molecular mechanism of the α-β transition? Is there a key structural parameter that controls this transition? Here we report a systematic computational and theoretical study to address this issue.

We consider 13 randomly picked α-helical coiled-coil proteins selected from the Protein Data Bank (PDB) (Berman et al., 2000) with varying lengths, all subjected to mechanical stretching. Coiled coils are double-stranded protein motifs (*e.g.* found in myosin and kinesin), where each strand is an α-helix with heptad repeated substrings of the form. This seven residue repeat generally has apolar residues at the first and fourth position, forming a left-handed hydrophobic stripe. Following the orientation of this stripe, the two α-helical strands wrap around each other to form a coiled-coil. Each protein is first fully energy minimized (we adjust the coordinates of all the atoms in models to reduce the potential energy via Steepest Descent and Adopted Basis Newton-Raphson methods) and then equilibrated at finite temperature (300 K). In equilibrium, each α-helical strand is stabilized by clusters of 3-4 hydrogen bonds (H-bonds) formed between in each turn as shown in Fig. 3.8A. All simulations are performed using an NVT ensemble (by Nose-Hoover thermostat), with a 1 fs time step. We employ the CHARMM19 all-atom energy function and an effective Gaussian model for the water solvent (Lazaridis and Karplus, 1997; Lazaridis and Karplus, 1999) to facilitate rapid sampling of configurations under loading (Paci and Karplus, 2000). After equilibration, each structure is stretched by SMD, following the shear loading condition shown in Fig. 3.8B. The $C_\alpha$ atom at the left end of one helical strand is fixed to resemble the attachment at a substrate, while the $C_\alpha$ atom at the right end of the other strand is linked to a harmonic spring with a spring constant of 10 kcal/mol/Å$^2$. We pull at a constant velocity of

0.01 Å/ps along the axial direction as shown in Fig. 3.8A, and the displacement and pulling force are recorded. The tensile strain is expressed as $\varepsilon = \Delta L/L_0$, where $L_0$ is the initial end-to-end length of the protein and $\Delta L$ is the extension. By analyzing both the H-bond patterns and the backbone geometry with the STRIDE algorithm (Frishman and Argos, 1995), we assess the secondary structure and associated changes during deformation. For each protein, the stretching simulations are repeated 10 times with a different random seed for the initial velocity distribution to obtain good statistics. Based on the results of an ensemble of 10 simulations for each protein, we then calculate the percentage of the occurrence of the α-β transition as a function of the coiled-coil length.

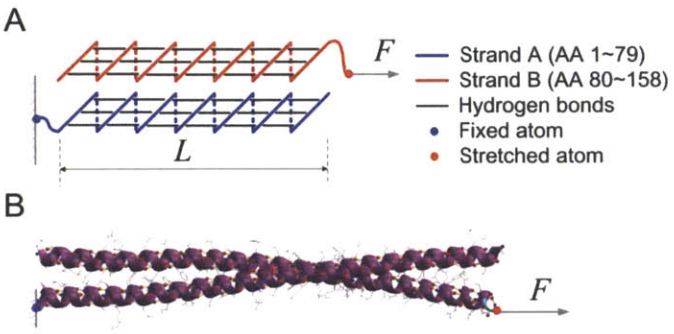


**Fig. 3.8 Model for studying the strength of coiled-coil proteins under shear loading (Qin and Buehler, 2010c).** Panel A: Schematic of the structure and loading condition of the coiled-coil (AA= amino acid residue). Panel B: Example molecular structure of the 2B segment in the vimentin protein (PDB ID 1gk4).

We begin by investigating a very short coiled-coil and a very long one. The short coiled-coil has a PDB ID 1ajy ($L_0 \approx 2.6$ nm). From the force-strain curve shown in Fig. 3.9A, we see that the stretching force remains at a low value, where the maximum force approaches 200 pN at 55% strain. The two helical strands slide against each other (Fig. 3.10A). We observe that only a few amino acids close to the ends of the protein domain are unfolded during the simulation, whereas most other parts of the structure remains intact (Fig. 3.10C). The long coiled-coil has a PDB ID 1gk4 ($L_0 \approx 11.5$ nm). Here, even though all simulation parameters are identical, the force-strain relation shows a dramatically different behavior compared with the previous one, and displays four phases (Fig. 3.9A).

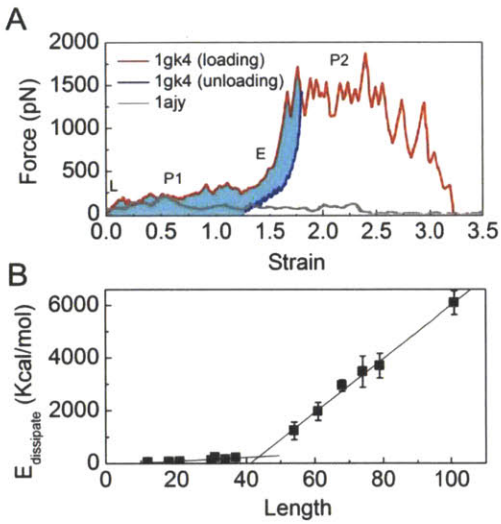


**Fig. 3.9 Forcestrain behavior of two coiled-coil proteins with different lengths (Qin and Buehler, 2010c)** (A) (PDB ID 1gk4, where the modulus in the L region is 0.3 GPa average diameter 2.4 nm, and in the E region reaches 8.9 GPa average diameter 1.1 nm; PDB ID 1 ajy, short). The shaded area reflects the energy dissipated during unfolding. (B) Dissipated energy during the entire stretching process, for coiled-coil proteins with different lengths.

First, we find a linear rise (phase (L)) towards a plateau at 200 pN (phase (P1)). At the end of phase (P1) we observe a regime with significant stiffening (phase (E)), followed by another, bumpier plateau phase (P2) at relatively large force levels close to 1500 pN. A structural analysis as a function of strain as shown in Fig. 3.10D suggests that the secondary structure remains intact within phase (L), indicating that the protein undergoes solely elastic deformation below 15% strain (no H-bond rupture).

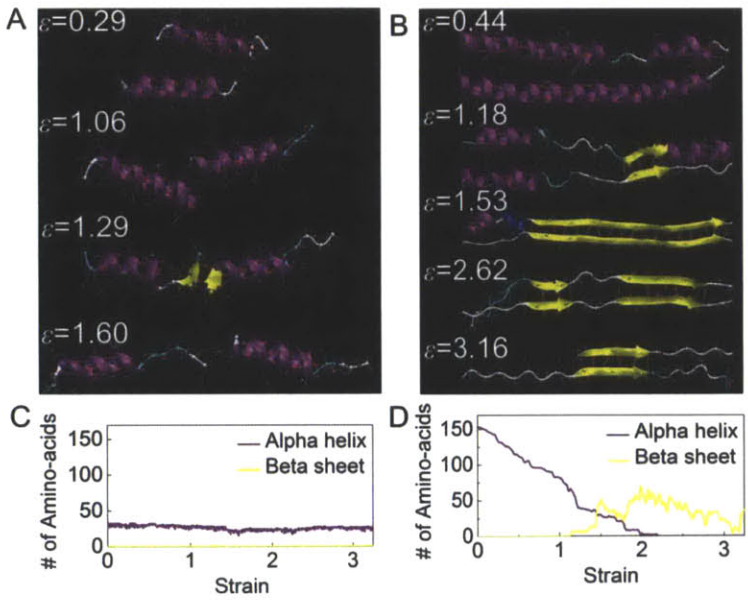


**Fig. 3.10 Simulation snapshots of two coiled-coil proteins under shear (Qin and Buehler, 2010c)** (proteins with PDB ID 1ajy [(A), (C)] and 1gk4 [(B), (D)]). (A) and (B) Structure under applied strain during stretching of the proteins (H bonds are shown as dashed lines). (C) and (D) Number of amino acids associated with alpha-helix and beta-sheet secondary structures as a function of strain.

The snapshots shown in Fig. 3.10B reveal that within phase (P1), each strand twists as it unravels, and that groups of H-bonds along the alpha-helix rupture, causing a sudden unfolding of helical turns. (It is noted that up until this point, the coiled-coil responds to the mechanical load in the similar way as the experimental and simulation results for myosin stretching (Root et al., 2006; Schwaiger et al., 2002).) Phase (E) begins at force levels of 360 pN, but the force increases to more than 1000 pN at strains beyond 150%. In phase (P2), a

large number of beta-sheets have formed, and an increase in the strain leads to the sliding of the two strands against one another, at a force level ~1500 pN (1200–1800 pN; the fluctuations are due to the stretching, rupture and rebinding of the H-bonds in the sheared beta-sheet segments resembling a stick-slip motion). We note that this force level agrees with the strength of natural beta-sheets reported in earlier studies (Sotomayor and Schulten, 2007) at a similar pulling speed. The much greater shear resistance is caused by the fact that beta-sheets in shear mode display a significantly larger strength (Keten and Buehler, 2008a; Keten and Buehler, 2008b; Sotomayor and Schulten, 2007) than alpha-helical proteins (Ackbarow et al., 2007; Schwaiger et al., 2002). Phase (P2) lasts until 325%, where the structure is completely detached. Fig. 3.11A shows an analysis of the secondary structure as a function of strain, providing additional details into structural changes. This transformation of the secondary structure from an alpha-helix to a beta-sheet rich structure resembles the α-β transition observed in experiments. Further, the comparison of the two cases shows that the α-β transition changes the coiled-coil domain from a flexible structure at small deformation to a much stiffer and stronger structure at large deformation.

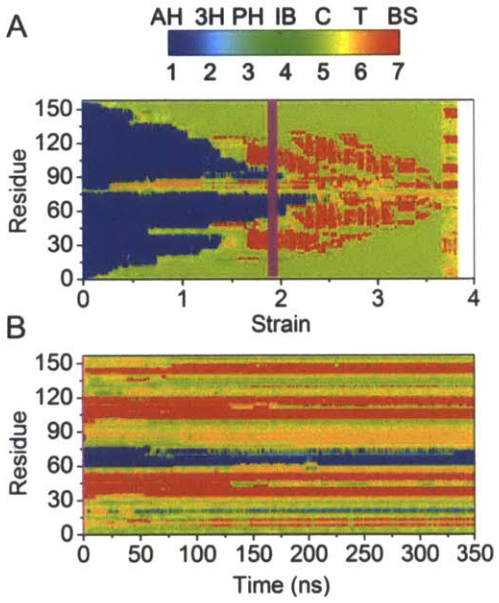


**Fig. 3.11 Structure spectrum for structures under stretching (Qin and Buehler, 2010c).** Panel A: Structure spectrum for structure of the protein 1gk4 under stretching. Panel B: Structure spectrum of the protein 1gk4 during equilibration. The color bar distinguishes 7 structures: Alpha helix (AH), 3–10 helix (3H), Phi helix (PH), Isolated bridge (IB), Coil (C), Turn (T), beta sheet (BS).

We record the unloading $F-\varepsilon$ curve after the α-β transition has occurred. To achieve this, we begin from the configuration obtained at a strain of 180%, and subsequently relax the applied force to zero and then set the two ends free and equilibrate the structure. During 350 ns equilibration, no structural changes are observed as confirmed by the spectrum analysis (Fig. 3.11B). Considering the relatively long time interval, the newly formed beta-sheets appear to be rather stable. This irreversible character of the transition is also found in experimentally observed α-β transitions (Kreplak et al., 2004b; Qin et al., 2009b). The force-strain results of the unloading curve are depicted in Fig. 3.9A, showing that the protein filament retracts during relaxation. However, the protein does not approach the length at the beginning of the simulation, confirming that permanent deformation has occurred. The shaded area in Fig. 3.9A represents the dissipated energy during the unfolding-refolding process, where the dissipated energy is 846 kcal/mol (by evaluating $E_{diss}=\int_0^{180\%}(F_{load}-$

$F_{unload})L_0 d\varepsilon$). Since the number of broken H-bonds during the process is $N_H = 119$ at 180% strain (compared with the initial coiled-coil structure shown in Fig. 3.8), we estimate the energy associated with each H-bond as $E_{HB} = E_{tot}/N_H = 7.11$ kcal/mol.

The initiation of the α-β transition process occurs in three major phases. From phase (L) onwards, a single turn in the middle of the intact strand unravels locally inside one of the alpha-helices (this explains why the ultimate force in this phase approaches the unfolding force of a single alpha-helix). This structural defect, locally highly flexible, forms a nucleation point from which on nearby amino acids begin to unfold, turning them into random coils, as shown in Fig. 3.10B at $\varepsilon = 0.44$ (the increase in flexibility can be explained by the significant decrease in persistence length, from several tens of nanometers for an α-helix to approximately 0.4 nm for a random coil). The increasing number of unfolded turns in both helices increases the probability for hydrophobic interactions to take effect between the two alpha-helices, which squeezes two unfolded turns together to form a first parallel beta-sheet cluster (Figs. 3.10A, $\varepsilon = 1.29$ and B, $\varepsilon = 1.18$), here referred to as a beta-sheet seed. In the shorter coiled-coil, there is either no beta-sheet seed or the beta-sheet seed is not strong enough to induce further unfolding of alpha-helical turns, and rather ruptures, leading to interprotein sliding (Figs. 3.10A and C). In the longer coiled-coil, however, the beta-sheet seed acts as an effective clamp that prevents sliding and thereby enforces unfolding of all other alpha-helical turns (Fig. 3.10B, $\varepsilon = 1.53$), resulting in the occurrence of the transition process throughout the rest of the chain (Fig. 3.10D). At the end of the transition process, the structure is composed of an array of many small β-sheet clusters (Fig. 3.10B, $\varepsilon = 2.62$). The key to understand this process is to consider the ratio of the strength of the β-sheet seed ($f_B$) versus the strength of the α-helix ($f_A$), where the ratio of $f_B/f_A$ controls whether ($f_B/f_A \geq 1$) or not ($f_B/f_A < 1$) the α-β transition occurs.

The off rate of a reference structure (alpha-helix or beta-sheet) with a reference length $N_0$ is (Ackbarow et al., 2007; Evans, 2001; Rief et al., 1998): $\chi_0 = \omega_0 \exp[-(E_b - F_0 x_b)/(k_B T)]$, where $\omega_0 = 10^{13} \mathrm{s}^{-1}$ is the natural frequency of bond vibration (Bell, 1978), $x_b$ the unfolding transition point, $k_B$ the Boltzmann constant, $E_b$ the energy barrier, $F_0$ is the averaged unfolding force, and $T$ the temperature. The off rate of alpha-helices of general length $N$ is $\chi = \omega_0 (N/N_0) \exp[-(E_b - F_0 x_b)/(k_B T)]$, which considers the fact that α-helical turns are arranged in series (so that increasing the length increases the probability of unfolding). Noting the fact that pulling speed $v = \chi x_b$ is constant we obtain

$$f_A(N) = F_0 - \frac{k_B T}{x_b} \ln\left(\frac{N}{N_0}\right) \sim -\ln(N) \tag{3.1}$$

We note that longer alpha-helices result in a reduced mechanical strength with a negative logarithmic dependence on $N$, a finding that has been validated in experiments and simulations (Dietz and Rief, 2008). We now calculate the strength of the β-sheet seed, $f_B$. The energy barrier in the beta-sheet shearing is $E_b = E_{HB} n_{cr}$, where $n_{cr}$=3-4 is the number of H-bonds that are involved in a unit rupture event. This number is based on the observations made in our simulations, the initial beta-sheet seed formed under shearing includes 3-4 H-bonds, which is contained in each alpha-helical turn (Ackbarow et al., 2007) (and two turns combine to form the beta-sheet seed with a same number of H-bonds.

Combining with the expression of $\chi_0$, we arrive at

$$f_B(n_{cr}) = \frac{1}{x_B}\left[k_B T ln\left(\frac{v}{\omega_0 x_B}\right) + E_{HB} n_{cr}\right] \tag{3.2}$$

where $v$ is the pulling speed, and $x_B$ the rupture distance along the shearing direction. Since the size of the β-sheet seed is constant at $n_{cr}$ regardless of the length of the alpha-helical proteins in the coiled-coil, $f_B(n_{cr}) = f_B$ as a constant.

We now identify numerical values of the parameters in Eqs. (3.1) and (3.2) (directly from the atomistic model). For Eq. (3.1), the strength of an alpha-helical protein with $N_0 = 79$ at 0.01 Å/ps pulling speed is $F_0 = 200$ pN, and $x_b$=0.2 Å (parameters extracted from a pulling experiment of a single alpha-helical protein (Ackbarow et al., 2007)). For Eq. (3.2), $E_{HB} = 7.11$ kcal/mol (this value is extracted from the simulations as described above, and is also close to the value predicted from density functional theory (Tsemekhman et al., 2007)), and $x_B$ =4 Å (this value is obtained from geometric analysis (Keten and Buehler, 2008a)). As shown in Fig. 3.12A, of an initial beta-sheet seed falls within the range of 346.5±61.5 pN, whereas $f_A$ varies greatly as a function of the length from 140 pN to 610 pN. Based on the analysis carried out here, the condition $f_B = f_A(N_{cr})$ enables us to solve for the critical amino acid number $N_{cr} = 41 \pm 12$ from which on the α-β transition occurs.

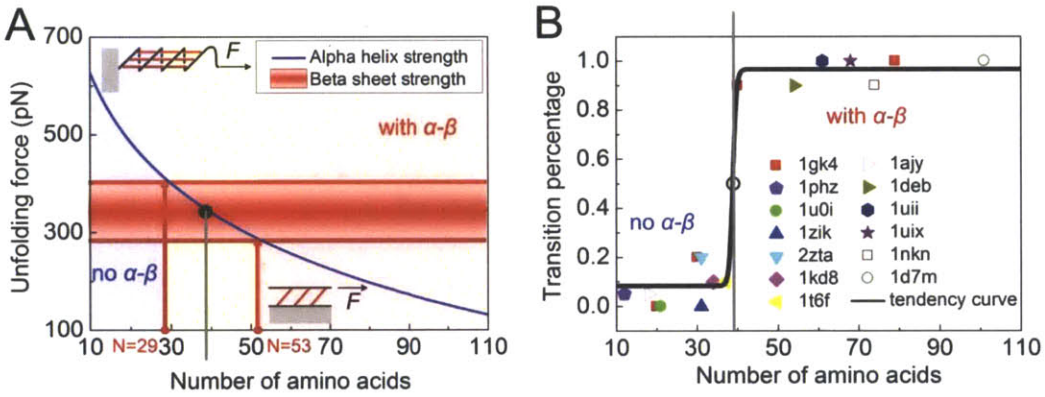


**Fig. 3.12 Theoretical and simulation result of the length dependence in α-β transition (Qin and Buehler, 2010c).** Panel A: Theoretical analysis of the critical condition for the α-β transition, where the shaded area in the middle represents the critical condition. The left side of the critical point corresponds to sliding and unfolding of the α-helices without occurrence of the α-β transition, while the right side corresponds to the regime in which the α-β transition occurs. Panel B: Percentage of α-β transition occurrence for various coiled-coil proteins (simulation). Each point reflects the percentage of the transition within the simulation ensemble. The fitted curve is a sigmoid function $\boldsymbol{p = A_2 + (A_1 - A_2)\{1 + exp\,[(n - n_0)/dx]\}^{-1}}$, with $\boldsymbol{A_1 = 0.083}$, $\boldsymbol{A_1 = 0.967}$, $\boldsymbol{n_0 = 38.835}$, and $\boldsymbol{dx = 0.465}$. The fit enables us to identify the transition point from the simulation data, leading to $\boldsymbol{N_{cr} = 38.7}$ (probability 50%).

We carry out simulations for 13 different coiled-coil proteins (corresponding PDB ID shown in Fig. 3.12B), and measure the probability for the occurrence of the α-β transition).

The results show that the points fall in two distinct regions and that the transition occurs at a critical number of $N_{cr} = 38.7$ amino acids (or 5.7 nm), which agrees with the theoretical analysis, thus corroborating the concept of a critical length for the α-β transition. It is noted that the outcome of the test for each protein is highly repeatable, since most of the points are either one or zero, except for those near the critical length (for these, the repeated simulations give appropriate statistics and convergence).

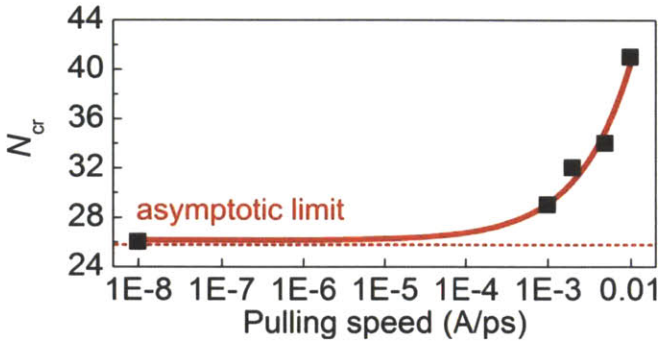


**Fig. 3.13 Critical number of amino acids $N_{cr}$ as a function of the pulling speed (Qin and Buehler, 2010c).** The continuous curve is a power law fit to the simulation data (asymptotic limit $\boldsymbol{N_{cr} = 26}$)

From further analysis we find that the critical length decreases even under extreme variations of the pulling speed. For example, at $v = 0.005$ Å/ps, we obtain $F_0 = 167$ pN, $f_B = 340$ pN and $N_{cr} = 34$; at $v = 0.002$ Å/p, $F_0 = 146$ pN, $f_B = 330$ pN and $N_{cr} = 32$; at $v = 0.001$ Å/p, $F_0 = 116$ pN, $f_B = 323$ pN and $N_{cr} = 29$. At vanishing pulling velocities corresponding to experimental and physiological conditions (at 1 μm/s and less), we estimate a critical number of 26 amino acids, or 3.8 nm ($F_0 = 14$ pN, $N_0 = 288$, $x_b = 1.2$, $f_B = 96$ pN and $N_{cr} = 26$ based on asymptotic strength estimates as reported in the early work (Ackbarow et al., 2007; Keten and Buehler, 2008a; Keten and Buehler, 2008b; Qin et al., 2009a)). These results (Fig. 3.13) are rather similar to the findings at larger pulling speeds, and illustrate the robustness of the prediction put forth here.

### 3.2.5 Rate dependence of tensile response

We extend the mechanical analysis by performing stretching simulations with pulling rates ranging from 0.0001 Å/ps to 1 Å/ps. The unfolding force at the angular point (denoting the onset of domain unfolding in the protein) is plotted as a function of the pulling speed in Fig. 3.14. The results show a significant dependence on the unfolding force as a function of pulling velocity, reaching a plateau value for small pulling speeds on the order of ≈100 pN. Using those results to fit the Bell model whose details are given in (Ackbarow et al., 2007; Qin et al., 2009a), the following is abtained:

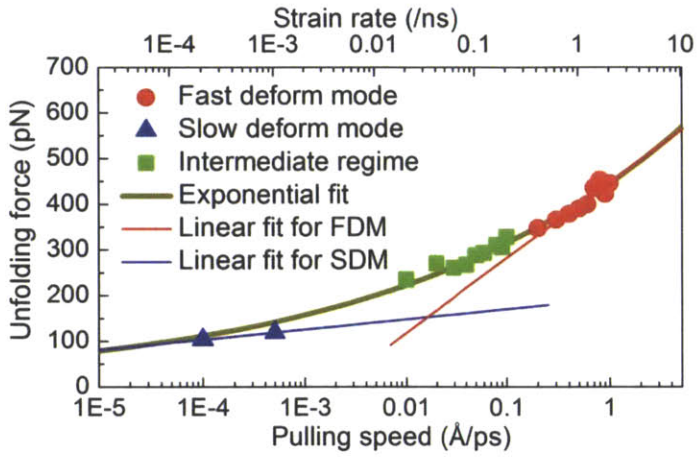


**Fig. 3.14 Unfolding force as a function of the pulling speed and corresponding strain rate (Qin et al., 2009a).**

$$f = \frac{k_B T}{x_b}\ln(v) - \frac{k_B T}{x_b}\ln(v_0), \tag{3.3}$$

where $f$ is the unfolding force, $k_B$ is Boltzmann constant, $T$ is the temperature, $v$ is the pulling speed, and $v_0$ is the natural bond-breaking speed defined as

$$v_0 = \omega_0 x_b \exp\left(-\frac{E_b}{k_B T}\right). \tag{3.4}$$

Here $\omega_0 = 10^{13}\mathrm{s}^{-1}$ is the natural vibration frequency. We obtain for the slow deformation regime (as shown in Fig. 3.14), $E_b = 14.05$ kcal/mol and $x_b = 4.27$ Å. For the fast deformation regime, we obtain $E_b = 5.18$ kcal/mol and $x_b = 0.64$ Å, where $E_b$ and $x_b$ physically equal the energy barrier height and width to unfold the molecule. In earlier studies (Evans and Ritchie, 1997) it has been suggested that the protein structure strength increases as a weak power of rate under slow loading. Based on this suggestion, we use an overall fitting function to the data defined as

$$f_{\mathrm{fit}}(v) = A\exp\left(\frac{\ln(v)}{B}\right), \tag{3.5}$$

which empirically captures the asymptotic trend of the strength properties for a very wide variation of pulling speeds. The parameters $A$ = 222.77 pN and $B$ = 6.634 are obtained by fitting Eq. 3.5 to the overall simulation results as shown in Fig. 3.14. The prediction of Eq. 3.5 for pulling velocities comparable to those used in experiment (on the order of $8 \times 10^{-12}$ Å/ps) is ≈10 pN, being in agreement with experimental results (Fudge et al., 2003) that reported a strength of 15.7 pN in regime (II). For the coiled coil myosin structure, the unfolding force measured by atomic force microscopy (with a cantilever speed of 1 μm/s) is ≈33 pN (Root et al., 2006), while from our model the unfolding force for this pulling velocity is found to be 28 pN. This comparison suggests a rather good agreement with experimental results.

## 3.3 Validation in atomic force microscopy experiment

To compare our result with that of AFM stretching of single filaments, knowing the fact

that unit length filaments fuse from the head to the tail to form full length filaments, we look at the force-strain curve from $\varepsilon_0$ =60% strain which corresponds to the beginning of the third region. The strain within the overlapped region thereby yields

$$\varepsilon_{overlap} = (\varepsilon - \varepsilon_0) L_{tetramer} / L_{overlap} \tag{3.6}$$

Where $L_{tetramer}$ and $L_{overlap}$ are the lengths of the tetramer and overlapped region with their value summarized in Fig. 2.9. The force is divided by the cross-sectional area of the tetramer, $A_0$= 32.9 nm$^2$ for stress. To account for the rate effect that makes the force orders larger than those of experiments (Ackbarow et al., 2007; Sotomayor and Schulten, 2007), we use a force scaling factor of $b$=7.1. This value is based on earlier studies that for beta-sheet proteins the strength at 0.1 Å/ps pulling speed is 1700 pN (Keten and Buehler, 2008b). For slow pulling on the order of $10^{-11}$ Å/ps the strength is found to be 240 pN (Sulkowska and Cieplak, 2007). The normalized stress yields

$$\sigma_{overlap} = \frac{F}{A_0 b} \tag{3.7}$$

Eqs. 3.6 and 3.7 facilitates a direct comparison with experimental results using AFM (Kreplak et al., 2008), as given in Fig. 3.15.

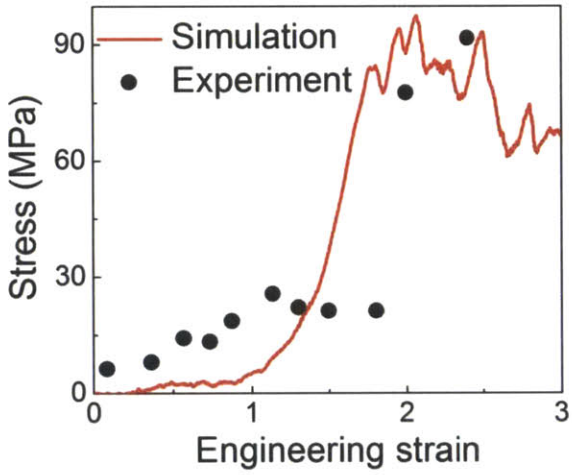


**Fig. 3.15 Comparison of stress-strain curve of IF filaments between experiment and simulation (Qin et al., 2009b).**

A quantitative comparison with AFM experiments to summarize the mechanical property of single IF filaments (Kreplak et al., 2008) is presented here as shown in Fig. 3.15. It is shown that there is overall good agreement between simulation and experiment. The resulting maximum stress for the filament is predicted to be ≈97 MPa (found at ≈205% strain) from simulation, close to experimental measurements of 90 MPa at similar levels of strain (Kreplak et al., 2008). The transitions of the stress-strain behavior and the maximum strength in the two methods show overall good agreement. However, in the lower strain regime before transition, the experimental stress is higher, possibly caused by effect of sliding of the filament on the surface during stretching. From the analysis of the stressstrain behavior, we extract the tangent modulus for the full length filament to be ≈3–12 MPa below 50% strain. This modulus is close to experimental results as summarized in Fig. 3.16, where a range of ≈7–15 MPa was reported (Fudge et al., 2003; Kreplak et al., 2008). We note that the initial

tangent Young's moduli found here are significantly smaller than typical values reported for α-keratins (1.8 GPa), microtubules (0.9 GPa) (Hearle, 2000) and F-actin (2.6 GPa) (Gittes et al., 1993), confirming the characteristic properties of IFs. In both simulation and experiment, the tangent modulus increases by a factor of ≈20 once 150% strain is reached, leading to severe stiffening. The tangent modulus in simulation approaches ≈185 MPa before failure, similar to experimental results. The reason to cause differences between simulation and experiment is not yet well understood. Possible explanations include the presence of defects, structural irregularities, and the fact that much longer filaments are considered in experiment, whereas the small system considered in our simulations is pristine without any structural flaws.

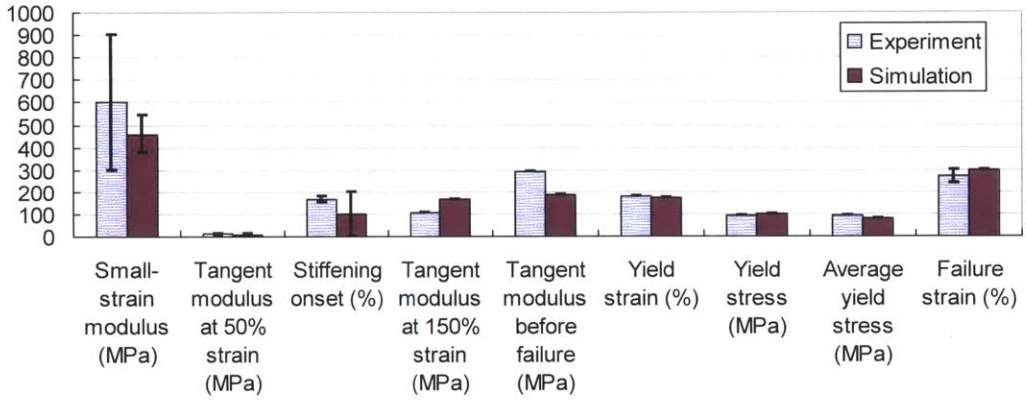


**Fig. 3.16 Comparison of mechanical properties of IF filaments between experiment and simulation (experiment results from (Fudge et al., 2003; Guzman et al., 2006; Kreplak and Bar, 2009a; Kreplak et al., 2008))**

# 4 Multiple-scale modeling of intermediate filament network

Having understood the basic structural and mechanical properties of IFs, we upscale our simulation to study the physical and physiological roles this filament system plays in cells. IFs are often neglected in cell mechanics models based on principles such as tensegrity (Ingber, 1993) or soft glassy materials (Fabry et al., 2001). It is generally argued that IFs are too flexible compared to MFs and MTs to have any major impact on cell elasticity at small strains or even on cell adhesion and cell motion. However early studies on vimentin deficient cells and cells treated with acrylamide pointed towards a pivotal role of IFs in cell stiffness, stiffening and growth (Wang and Stamenovic, 2000; Wang and Stamenovic, 2002). Recently, Bhattacharya et al. demonstrated that vimentin IFs mediate cell adhesion strength through their interactions with plectin and β3 integrin (Bhattacharya et al., 2009). Moreover, skin fibroblasts of plectin deficient mice generate less traction forces at focal adhesion sites compared to skin fibroblast of wild-type mice (Na et al., 2009). Interestingly, the same cells are also deficient in long distance propagation of mechanical stresses in the absence of plectin (Na et al., 2009). The disruption of mechanotransduction remains to be demonstrated in the absence of IFs instead of plectin.

So far the extensibility of IFs has already been demonstrated in sonic muscle fibers of the type I male midshipman fish (Lewis et al., 2003). In this special skeletal muscle developed for high frequency contraction, the desmin IF network is better organized in 3D than any other vertebrate skeletal muscle (Wang and Ramirezmitchell, 1983). This particularity enabled Lewis et al. to follow by immunofluorescence the deformation of the desmin network in a muscle fiber stretched to 60% strain (Lewis et al., 2003). Such strains did not induce breakage of the filaments and the deformation was reversible at the resolution of immunofluorescence (Lewis et al., 2003). Based on this result and nanomechanical data on single IF filaments (Kreplak and Bar, 2009b; Kreplak et al., 2008; Qin et al., 2009b), it is straightforward to propose that IF networks may behave as "security belts" in tissues exposed to large tensile strains (Wang et al., 1993a).

## 4.1 Background on mechanics of nuclear lamina

The nuclear lamina is a dense meshwork at the inner membrane of the nuclear envelope of eukaryotic cells1 and is formed primarily by ≈10 nm wide type-V IFs composed of lamin proteins (Aebi et al., 1986; Chang et al., 2006; Herrmann et al., 2007; Ishikawa et al., 1968). The lamina contributes largely to the structural integrity of the nucleus, and therefore a key biological role is to protect genetic material against extreme environmental conditions (Burke and Stewart, 2002; Qin et al., 2010). The lamina is broken down during mitosis; this, however, represents only a relatively short period during the life of a cell (Guttinger et al., 2009; Panorchan et al., 2004). Emphasizing the importance of this meshwork is the fact that there

are at least 13 human diseases associated with mutations in lamin proteins. For example, the permanent loss of lamin proteins causes muscular dystrophy and cardiomyopathy, and overaccumulation of lamin mutants at the nuclear membrane causes the rapid aging disorder Hutchinson-Gilford progeria syndrome (HGPS) (Eriksson et al., 2003; Omary et al., 2004; van der Kooi et al., 2002).

What is remarkable is that all the various types of nuclear lamina naturally feature structural imperfections, defects, and heterogeneities including those induced by nuclear pores (Aebi et al., 1986; Goldberg et al., 2008a; Goldberg et al., 2008b; Schermelleh et al., 2008). Defects in the lamina can also be caused by localized forces from cytoskeletal structures or by atomic-scale defects due to the imperfect assembly of the meshwork, leading to void formation in the meshwork (Aebi et al., 1986; Dahl et al., 2004; Goldberg et al., 2008a; Goldberg et al., 2008b). Another source of imperfections is generated by the clustering of lamin-associated nuclear pore complexes, which can grow rather large and are naturally present in virtually all cells (Beaudouin et al., 2002; Goldberg et al., 2008a; Schermelleh et al., 2008). Other possible factors include ionizing radiation that results in the breakage of covalent or noncovalent bonds within protein structures and thus results in structural defects (Djaczenk.W et al., 1973; Munro, 1970; Szekely et al., 1980). It has been shown that continuous radiation, as experienced for example during space flight, causes cracks to occur around nuclear pores which leads to a complete fragmentation of nuclear envelopes once a critical defect concentration is reached (Djaczenk.W et al., 1973).

While experimental data has provided clear evidence that nuclei in healthy cells can effectively withstand extreme dilations and deformation without rupture (Dahl et al., 2004), conventional material models have failed to explain their significant capacity to expand without failure. This is because in most existing models locations of structural imperfections such as crack-like inclusions present singularities for stresses, which typically causes a deterioration of material properties. However, this is not observed in nuclear lamina which provides an extremely robust mechanical framework to protect genetic material (Janmey et al., 1991). Here we present an answer to this intriguing question and explain a general mechanism by which the IF meshwork, and potentially other protein materials, are capable of forming an extremely robust flaw-tolerant material. We use a simple model developed based on a multiscale approach to assess the mechanisms of defect initiation and propagation in the nuclear lamina under extreme loading conditions, mimicking the conditions a cell experiences during tissue stretching and contraction. The use of a multiscale approach to deal with this problem allows us to simulate a system with tens of micrometers dimension while retaining information about molecular structures and mechanisms.

## 4.2 Modeling of nuclear lamina

We consider a meshwork model resembling a *Xenopus* oocyte nuclear lamina (Aebi et al., 1986; Goldberg et al., 2008b) because the structural and mechanical properties of this meshwork are experimentally well characterized, and it represents one of the few measured systems of a pure nuclear lamina without mechanical coupling with chromatin (Dahl et al., 2004; Goldberg et al., 2008a). It is noted that so far only amphibian oocytes' nuclear lamina

has been shown to form a rather regular lattice (Aebi et al., 1986; Dahl et al., 2004; Goldberg et al., 2008a), while the structure of nuclear lamina in other cells is likely more disordered and more tightly associated with chromatin. Thus it is important to note that the model we study here may only represent a first approximation to the structure of other nuclear laminas. Fig. 4.1A illustrates the hierarchical structure of this nuclear lamina (Goldberg et al., 2008b; Herrmann et al., 2007; Qin et al., 2009b). We consider the meshwork with a small crack-like defect using uniaxial and biaxial tension to mimic in situ loading conditions (Fig. 4.1B). For instance, *in vivo* pressure differences across the nuclear envelope can result in an exposure of the nuclear lamina to significant biaxial tension (Dahl et al., 2004).

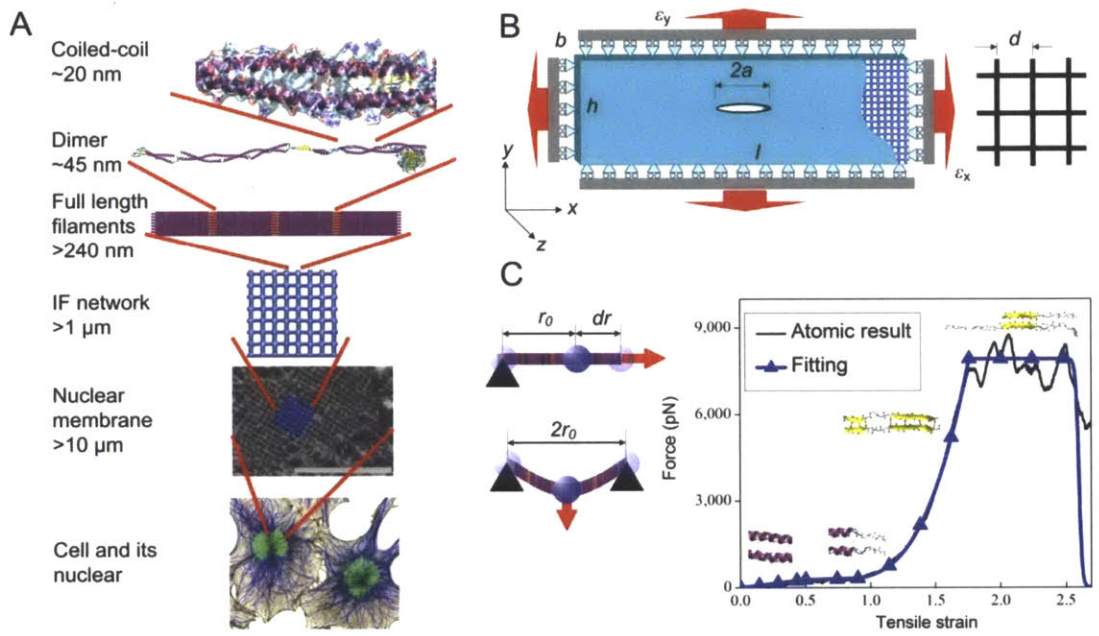


**Fig. 4.1 Hierarchical structure of an IF meshwork as found in the inner layer of nuclear envelope of Xenopus oocytes, boundary conditions in simulations, geometry of the meshwork model and tensile properties of a single IF (Qin and Buehler, 2011a; Qin and Buehler, 2011b).** A: Schematic of the hierarchical IF structure that ranges from nano to macro. Panel a shows typical structural features of IF meshwork, including hydrogen bonds, coiled-coil composed of alpha-helix, a lamin A dimer composed of coiled-coil and linkers, bundles of dimers that fuse laterally to form full length filaments with a diameter of $b \approx 10$ nm, which form an orthogonal meshwork attached to the inner nuclear membrane with a lattice constant of ~50 nm. The scale bar is 1 μm. B: The geometry of the orthogonal meshwork model, boundary conditions, and the coordinate system used in our simulations. The initial crack is oriented into the x-direction and the meshwork is loaded in one or both directions. The parameters *b, l,* and *h* denote the thickness, length, and width of the meshwork model; *d* is the lattice constant (≈50 nm) and $2a$ is the initial crack length. C: Schematic of the coarse-grain method used to model the meshwork. Mesoscopic particles or "beads" are used to describe full length filaments, where the equilibrated nearest neighbor distance is r0 and an interbead potential fitted from stretching tests based on full atomistic modeling of IF is adopted. Inserted figures are snapshots of the atomic model of a segment of the 2B domain of

an IF dimer under stretching, revealing molecular mechanisms of deformation.

### 4.2.1 Mesoscopic model based on atomistic modeling

As demonstrated by earlier experimental and computational molecular mechanics studies of the single IF level, the deformation mechanism is characterized first by elastic elongation, α-helix unfolding (Ackbarow et al., 2007), alpha-to-beta transition (see chapter 3, refer to (Qin and Buehler, 2010c) for more detail), and eventual stick-slip-sliding (Keten et al., 2010; Qin and Buehler, 2010b). This results in the characteristic nonlinear force-extension of a single fibril as shown in Fig. 4.1C, with a severe change in the tangent modulus as strain is increased. As a model we use the mechanical response of vimentin IFs obtained in the earlier work (Qin et al., 2009b) for exploring the mechanics of lamin meshwork (please refer to the Appendix part for modeling detail). This is a reasonable first approximation because all IF proteins consist of tightly packed and aligned subunits, where each subunit is primarily composed of an extended coiled-coil structure which is crucial for the molecular mechanical properties as described above (Fudge et al., 2003). Indeed a direct comparison between lamin and vimentin molecular mechanics reveals that the mechanical response of the lamin dimer is found to be similar as the vimentin dimer (Qin and Buehler, 2011a). It has been shown in earlier works that this force-extension result agrees with experimental measurements for the general class of IF protein family (Qin et al., 2009b) and we thus consider this in the formulation of our mesoscopic model to mimic the basic quasi-static deformation properties at vanishing pulling rates as relevant for physiological and experimental deformation speeds. This is an idealized mechanics model, which, although being limited by missing the diversity of IF types, offers a powerful starting point for understanding the fundamentals of the mechanical properties of IF meshworks. We emphasize that the goal of our model is not to accurately reflect the mechanical properties of one specific or all the different types of nuclear laminas. Rather it is formulated deliberately as a simple model to study generic aspects of the mechanical properties of protein meshwork materials at the microscale relating to the underlying molecular mechanics.

### 4.2.2 The flaw tolerance of nuclear lamina

On the basis of the knowledge of the behavior of a single fibril we now assess the mechanical response of an entire meshwork to large deformation by applying increasing uniaxial tension at the top and bottom layers. Fig. 4.2A shows snapshots of the meshwork model with increasing deformation. We observe that no catastrophic failure of the meshwork occurs below 161% strain. However, we find that the crack geometry transforms drastically from an initial sharp edge in the $x$-direction into an elliptic shape, where the longest axis pointed in the $y$-direction, with a ratio between long axis and short axis being $\approx 3$ (Fig. 4.2A). What is remarkable is that instead of forming a rather small localized deformation zone at the crack tip as seen in linear elastic materials such as concrete, carbon fibers, or silicon(Buehler et al., 2006), virtually all filaments in the meshwork (oriented in the $y$-direction) undergo large deformation and unfold. This represents the formation of a very large "yielding" region in which the elastic energy supplied by applied forces is dissipated. A detailed analysis of the forces that act on those filaments indeed confirms that the coiled-coil structure within each molecular subunit has undergone secondary structure unfolding via the breaking of clusters of

hydrogen bonds up to strains of 90%. As the load is increased beyond 90% strain, a greater number of filaments begin to stiffen due to the onset of an α-β transition at the molecular scale. For even greater loads, and when deformation reaches 161%, we observe that deformation starts to localize at the crack tip, resulting in eventual catastrophic failure of the meshwork. Under catastrophic failure the breakdown of the meshwork is mediated by highly localized breaking of individual filaments at the tip of the crack, and at the molecular scale due to slip of individual protein chains against each other (Fig. 4.2A, snapshot iv).

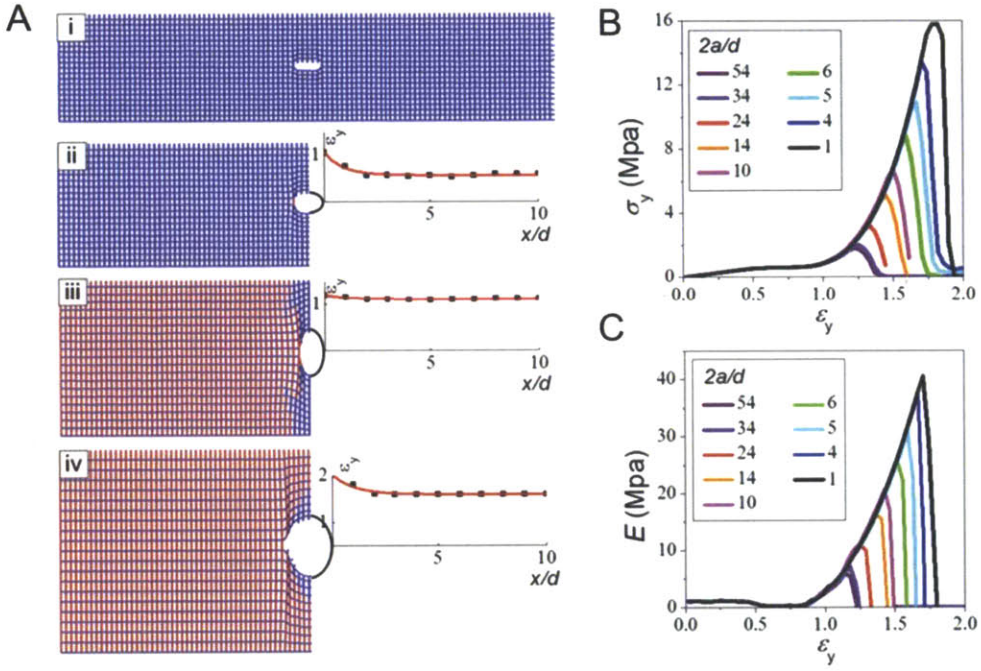


**Fig. 4.2 Deformation of the nuclear lamina under uniaxial loading at different levels of applied strain and mechanical analysis of the stress-strain properties of a meshwork with different crack sizes (Qin and Buehler, 2011a).** A, The snapshots i-iv show the deformation field for different levels of applied strain. i, $\varepsilon$=38%, ii, $\varepsilon$=58%, iii, $\varepsilon$=110%, and iv, $\varepsilon$=161%. Each filament is colored according to its structural character, with blue denoting the structure before the alpha-to-beta transition has occurred, and red for the structure after the alpha-to-beta transition has occurred (at filament strains of around 90%). Tensile strains of filaments in the x-direction starting from the crack tip are plotted for snapshots ii–iv, where snapshot iv shows the onset of propagation of the crack. B, Stress-strain relation for meshwork models with different initial crack lengths. C, Tangent modulus-strain relation derived from B.

To summarize our observations, we find a sequence of events that involves delocalization of deformation at applied strains below 161% strain, followed by localization of deformation at larger applied strains and eventual catastrophic failure during which a small number of filaments break. The ability of the material to mitigate the effect of the defect by dissipating energy via unfolding of all filaments in the meshwork is referred to as flaw tolerance. This flaw tolerance can be theoretically explained by the characteristic nonlinear material behavior provided by the IF meshwork. The stress-strain curves for the bulk material (with and without defect) are depicted in Fig. 4.2B and the Young's modulus ($E$) versus strain

($\varepsilon_y$) relation depicted in Fig. 4.2C show that the meshwork features a highly nonlinear deformation character, with initial softening, followed by stiffening and eventual softening at the failure point. The lowest tangent modulus $E$ is obtained at 70% strain and features a 3-fold decrease compared with the initial value at zero strain. The tangent modulus E then significantly increases with strain, and at the failure point reaches a value that is 24-fold as large compared to its initial value.

### 4.2.3 The mechanism of flaw tolerance in the nuclear lamina

The bulk strain-stress relation of a general nonlinear (that is, hyperelastic) material can be given by a simple power law as $\sigma \sim \varepsilon^N$, where $N$ is the so-called hardening exponent that describes the stress-strain response of a material. Thereby, $N < 1$ denotes softening behavior (also referred to as "elastic-plastic"), and $N > 1$ represents a stiffening material. As seen directly in Fig. 4.1C the behavior of the protein meshwork is therefore characterized by a change in the local hardening exponent $N$ as the loading is increased, where for deformation up to 90%, $N = 0$, and for larger deformation of up to 176% strain, $N \gg 1$.

Why is this parameter important? It is known from continuum fracture theory that crack-like defects such as voids typically result in stress and strain concentrations, which are mathematically described as singularities of stresses at the tip of the crack. The stress and strain singularity at the crack tip of a nonlinear material is given by (Rice and Rosengren, 1968)

$$\frac{\sigma_C}{\sigma_F} = F a^{\frac{N}{1+N}} \tag{4.1}$$

and

$$\frac{\varepsilon_C}{\varepsilon_F} = F^{\frac{1}{N}} a^{\frac{1}{1+N}}, \tag{4.2}$$

where $\sigma_C$ and $\varepsilon_C$ represent the critical structural transition or failure stress and strain of a single filament at the crack tip, $\sigma_F$ and $\varepsilon_F$ are the applied stress and strain to the meshwork to reach $\sigma_C$ and $\varepsilon_C$ at the crack tip, and $F = [K/\sqrt{\pi\sigma_C}]^{-[2N/(1+N)]}$ is a material constant ($K$ is the material's fracture toughness) (Pugno et al., 2008). The crack length, $a$, relates to size of the imperfections in the structure (see for example, in Figure 4.1B). Eq. 4.1 shows that the nature of the stress or strain concentration depends strongly on the hardening exponent $N$.

We now use this simple model of how stresses and strains are distributed near a crack to explain the findings of our simulations. The first important insight here is that the stress-strain response of the material in different regimes of deformation can be approximated by different values of $N$, reflecting the behavior seen in Figs. 4.2B and C. Eqs. 4.1 and 4.2 predicts that a change in $N$ leads to a drastic change in the stress and strain distribution near a crack tip. Specifically, $N = 0$ leads to a highly delocalized stress field but a localized strain field, where $N \gg 1$ leads to a highly localized stress field and a delocalized strain field. We note that here, "localized" means that a quantity is larger at the crack tip than elsewhere, and "delocalized" means that a quantity is of similar magnitude at the crack tip than elsewhere in

the system.

Indeed, in agreement with the notion that the hardening exponent $N$ changes as the meshwork is deformed, we observe two distinct types of stress and strain distributions around the crack tip. First, in the softening regime of up to 90% strain, the strain of the highly stretched individual filament at the crack tip tends to reach the end of the softening stage of 90% and leaves filaments further away from the crack tip exposed to a much smaller (applied) strain of 58% (as shown in Fig. 4.2A(ii)), and thus $\varepsilon_C/\varepsilon_F = 1.55$. This represents a localized strain, where all filaments oriented in the y-direction feature strains between those two bounds. However, because of the plateau in the force-strain curve the tensile forces that act on each filament for this range of strains are the same as shown in Fig. 4.1C, implying that the stress is delocalized and $\sigma_C/\sigma_F \approx 1$. This corresponds to the situation when $N \to 0$ (reflecting softening) in Eq. 4.1, which agrees with the hypothesis that this case leads to a delocalized stress distribution.

Second, in the stiffening stage from 90% up to 176% strain, we observe that the strain of filaments at the crack tip is 120%, and filaments further away from the crack tip are exposed to an applied strain of 110% (as shown in Fig. 4.2A(iii)). While the strain distribution is delocalized, quantified by $\varepsilon_C/\varepsilon_F \approx 1$, it leads to a highly localized stress distribution of $\sigma_C/\sigma_F \approx 2.2$ (as shown in Fig. 4.1C). We thus obtain $N \gg 1$ (reflecting stiffening) from Eq. 4.1, which agrees with the hypothesis that this case leads to a localized stress distribution. In the large-deformation regime of over 161% strain and when rupture occurs, single filaments at the crack tip reach the maximum strength as shown in Fig. 4.2A(iv) and break. This localized failure of single filaments at the crack tip results in eventual crack propagation (mediated by sequential breaking of single filaments at the crack tip) without any crack branching or other large-scale failure mechanisms that involve many filaments.

### 4.2.4 Fracture of nuclear lamina

Fig. 4.3 illustrates the failure mechanism of the meshwork with several snapshots shown for the case of uniaxial tensile crack loading (resembling mode I). To realize uniaxial tensile loading only $\varepsilon_y$ is increased with a constant lateral strain $\varepsilon_x = 0$. The meshwork is deformed and snapshots are taken at applied strains of $\varepsilon_{y1} = 37\%$, $\varepsilon_{y2} = 161\%$, $\varepsilon_{y3} = 162\%$, $\varepsilon_{y4} = 167\%$, $\varepsilon_{y5} = 172\%$ and $\varepsilon_{y5} = 174\%$. We observe no failure before $\varepsilon_{y2} = 161\%$, but the crack transforms from an initial horizontal orientation with a sharp edge pointed in the $x$-direction into a vertical orientation as the longest axis points in the $y$-direction. We observe that instead of forming a highly localized yield zone at the crack tip as typically seen in materials with a crack, all filaments in the direction in which tensile load is applied stretch significantly, and deformation extends over the entire specimen and is not limited to the crack tip region. A detailed analysis of the molecular state of these filaments reveals that the coiled-coil structure within each dimer building block has undergone molecular unfolding and a subsequent α-β transition (Qin and Buehler, 2010c). Catastrophic failure of the meshwork occurs once loading reaches $\varepsilon_{y3} = 162\%$ and proceeds by rapid extension of the initial crack, which continues to propagate as a rapidly moving single crack as is shown in Fig. 4.3(III-IV). At the single filament scale crack propagation is facilitated by the sliding apart of

protein filaments after the transition into antiparallel beta-strands is completed, as is shown in Fig. 4.1C. Crack propagation occurs in a straight fashion into the $x$-direction without any branching or other instabilities.

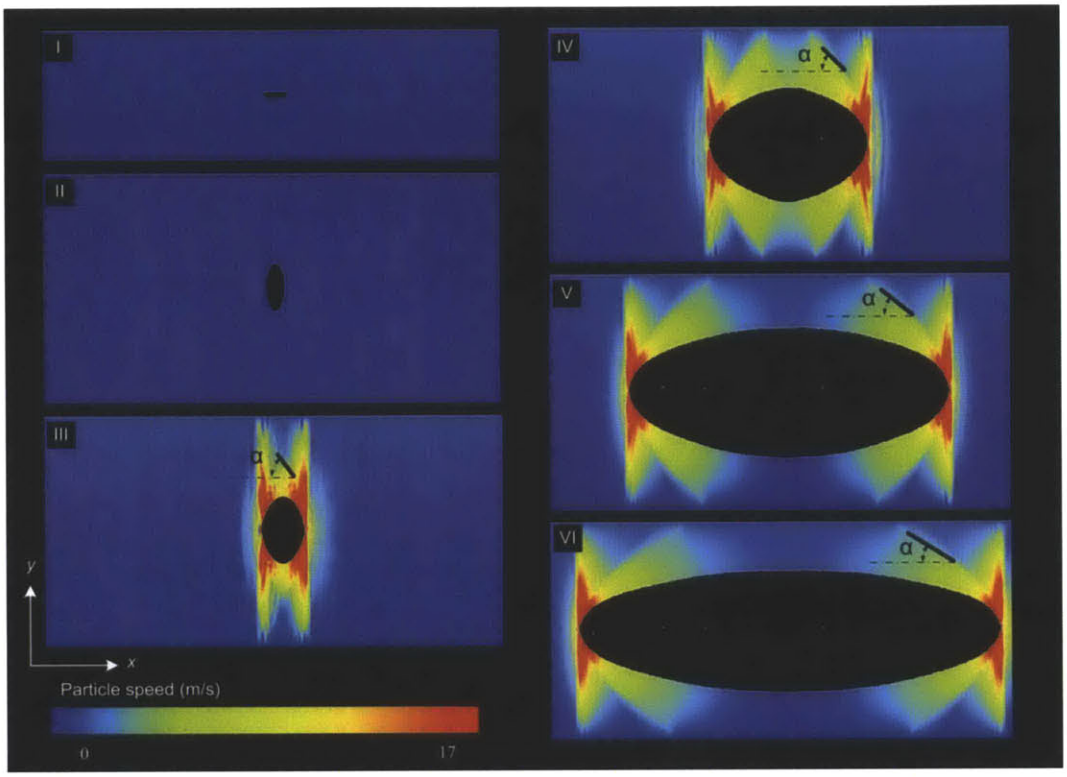


**Fig. 4.3 Snapshots of deformation profiles, mode I (uniaxial tensile) dynamic crack propagation and formed shock waves in the IF meshwork. The meshwork is loaded by uniaxial tension in $y$-direction (loading condition shown in) in a constant strain rate of 0.13 $ns^{-1}$(Qin and Buehler, 2011b).** The deformation mechanism of the material is characterized by molecular unfolding and sliding apart of the full length filament. The nonlinearity of the filament makes the material around the crack tip to form a large plastic yield region to dissipate energy instead of local breaking apart at the crack tip. The crack geometry under deformation changes from a sharp crack to an elliptical geometry with a 90 degrees rotated long axis. After the failure strain, the crack starts to propagate in both directions. Two wave fronts associated with shear wave speeds in the two orthogonal material directions are illustrated by the snapshots colored by the particle speed. According to the Mach cone angles of the two waves and speed analysis in the manuscript, the front wave correspond to the shear wave in filaments in the $y$-direction and the later wave correspond to the shear wave in filaments in the $x$-direction.

We proceed with a detailed analysis of the dynamics of failure by crack propagation. We measure the steady-state crack speed $C$ and find that $C = 18$ m/s, $C = 21$ m/s, $C = 26$ m/s and $C = 28$ m/s from small to large deformation, or from $\varepsilon_{y3}$, $\varepsilon_{y4}$, $\varepsilon_{y5}$ to $\varepsilon_{y6}$. We observe that as the crack moves through the material two distinct wave fronts emanate from each crack tip as shown in Fig. 4.3(III-IV). One of the wave fronts resembles a shock front similar to a Mach cone, whereas the other one is almost orthogonal to the crack propagation direction. For the

clearly visible shock wave, the measured angles between the wave front and the crack propagation direction are $\alpha \approx 53°$, $45°$, $36°$ and $33°$ for strains $\varepsilon_{y3}$, $\varepsilon_{y4}$, $\varepsilon_{y5}$ and $\varepsilon_{y6}$, respectively. Using these angles we estimate the wave speed associated with this particular shock wave based on the relation $\sin(\alpha) = C_0/C$, where $C_0$ is the characteristic wave speed that corresponds to the wave front with an angle of $\alpha$. Based on this analysis we find $C_0$ =14, 15, 15 and 15 m/s of $\varepsilon_{y3}$, $\varepsilon_{y4}$, $\varepsilon_{y5}$ and $\varepsilon_{y6}$, respectively. The occurrence of the shock wave suggests that crack propagation occurs faster than a characteristic wave speed of the material, which is estimated to be around 14-15 m/s. According to continuum theory the Rayleigh-wave speed is given by $C_R \approx 0.923\sqrt{G/\rho}$ , the shear wave speed by $C_S = \sqrt{G/\rho}$ and the longitudinal wave speed is given by $C_L = \sqrt{3G/\rho}$, where $G$ is the shear modulus of material and $\rho$ is the average mass density of the meshwork model. To estimate the wave speeds as a function of applied strain for the protein meshwork considered here we apply a shear stress $\tau_{xy}$ on the boundary of a perfect meshwork model under tensile loading with a strain $\varepsilon_x$ and record the shear stress over shear strain response as shown in Fig. 4.4A. We measure the shear modulus $G$ of the meshwork material by computing the slope of the curve at the origin, with results shown in Fig. 4.4B. By continuously changing the value of $\varepsilon_x$ we compute the shear modulus as a function of applied strain in the orthogonal direction. The analysis shows that the shear modulus and thus wave speeds increase as the loading is increased. For $\varepsilon_x = 0$ the shear wave speed and longitudinal wave speed in the $x$-direction are estimated to be $C_L = 25$ m/s and $C_S = 14$ m/s, respectively. We thus conclude that the shock wave front seen here corresponds to the shear wave speed that it is caused by crack propagation faster than the speed of shear waves in the surrounding meshwork material, where $C > C_S$; representing intersonic crack propagation.

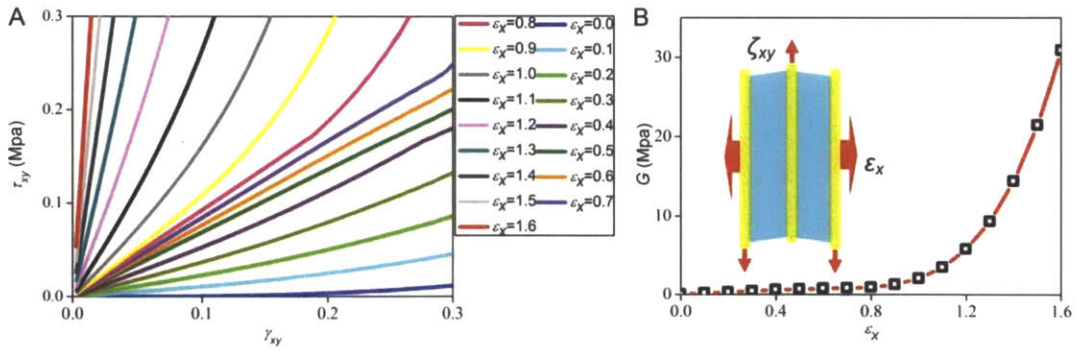


**Fig. 4.4 The shear stress-strain relation at different axial loading strain** (panel A) and the shear modulus $G$ of the material as a function of the axial loading strain $\boldsymbol{\varepsilon_x}$ (panel B). The results show that $G$ exponentially increases with the increasing $\boldsymbol{\varepsilon_x}$ and a broad range of $G$ can be achieved by altering $\boldsymbol{\varepsilon_x}$.

We suggest that the occurrence of intersonic crack propagation is due to the stiffening of the meshwork in the loading direction ($y$-direction), which results in an increased tangent modulus and as a result, in increased wave speeds and thus faster energy transport that can drive the crack to faster velocities (Buehler and Gao, 2006; Buehler et al., 2003). The shock

front emerges because the wave speeds become anisotropic under uniaxial loading. The shear wave speed and thus rate of energy transport in the $y$-direction increases as loading is increased due to the stiffening of the meshwork. Yet, the shear wave speed in the $x$-direction is limited to a constant value, and hence, we observe the emergence of a shock front as the crack speed is driven to larger values in excess of the shear wave speed. To test this hypothesis we carry out an equi-biaxial fracture test where the applied strain is identical in the $x$- and the $y$-direction, such that $\varepsilon_y = \varepsilon_x$. We observe, as expect, lack of shock wave fronts in this case due to the fact that under equi-biaxial loading the tangent moduli and thus wave speeds increase equally in both the $x$- and $y$-directions.

We also study effect of damping due to the presence of water, by considering a viscous drag force. Under the presence of water the critical strain $\varepsilon_C$ needed for crack initiation increases as the crack starts to propagate at a higher strain level. Once the crack starts to move, its steady speed starts with the Rayleigh-wave speed, increases in a steeper linear function with the increasing strain condition and reaches a maximum value as the same strain as in the model without solvent effect as shown in Fig. 4.5A. This result agrees with experimental observations that suggested that solvent viscosity slows down crack initiation as well as the propagation speed under constant pulling rates (Baumberger et al., 2006). However, what we observed here is that the effect of viscosity vanishes at extreme loading conditions and does not affect the steady-state maximum crack speed in this case.

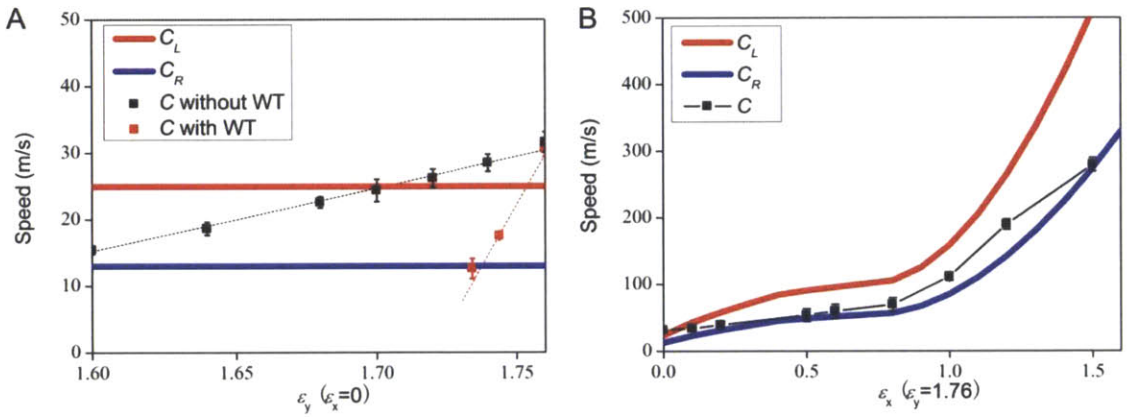


**Fig. 4.5 Steady-state crack propagation speeds, Rayleigh-wave speed and longitudinal wave speed as a function of loading conditions (Qin and Buehler, 2011b).** A. Crack speed as a function of uniaxial loading strain $\boldsymbol{\varepsilon_y}$. The crack speed is calculated from the derivative of half crack length $a$ to the time once the value becomes steady; the fluctuations of the measured speed define the standard deviation as shown by the error bars. The Rayleigh-wave speed and longitudinal wave speed in the x-direction are calculated from the shear modulus $G$ (as given in Fig. 4.4B) of a perfect meshwork model subjected to the corresponding loading condition. B. Crack speed as a function of loading strain $\boldsymbol{\varepsilon_x}$, with $\boldsymbol{\varepsilon_y = 176\%}$ kept constant. The crack speed significantly increases as $\boldsymbol{\varepsilon_x}$ increases, and the crack speed is between the Rayleigh-wave speed and longitudinal wave speed in the plastic zone, which act as the lower and upper bound of the crack speed, respectively. The results shown here demonstrate that the

crack propagation speed in the nuclear lamina is governed by the loading condition and the lateral strain $\boldsymbol{\varepsilon_x}$ is more dominant in governing the crack speed.

### 4.2.5 Effect of crosslink strength on failure mechanism

While it is known that single IFs are composed of bundles of subunits with hierarchical structures, from coiled-coil dimer level to the full length filament level, it is not clear how full length filaments associate to form a network structure, and in particular how the change of the chemical nature of their association can affect the particular mechanical and physiological function of the network. For example, divalent cations, such as $Ca^{2+}$ and $Mg^{2+}$, have been recognized as widely observed crosslinking agents in the vimentin network and their concentration can affect the stiffness of the entire filament network (Lin et al., 2010b). Plectin, a protein with coiled-coil structure, plays a role as linker to connect cytoskeletal filaments and is important for network organization and mechanical properties (Wiche, 1998). In this section, we do not restrict the focus on the role of any specific crosslinking agent but, for a more general purpose, we model both the IF and the crosslinks with varied mechanical properties and study how the strength of the crosslink affects the mechanical behavior of the overall IF network.

The structure of the network used in this study is composed by IFs distributed independently in the *x*- and *y*-directions and they are pinned by crosslinks at their intersections as show in Fig. 4.6A. This set up broadly mimics the microscopic structure of the *Xenopus* oocyte nuclear lamina (Aebi et al., 1986; Goldberg et al., 2008b; Qin and Buehler, 2011a). Realistic structures of IF network can be more disordered and/or have slightly variegated structures, but our model represents an approximation to the network. We focus on how the mechanical property of the crosslink affects the failure of IF network, while other factors such as chemical reactions are not included in our work. This is motivated by the fact that maintaining the mechanical integrity of cell is one of the most important functions of IF networks (Bertaud et al., 2010; Buehler and Yung, 2009; Panorchan et al., 2004).

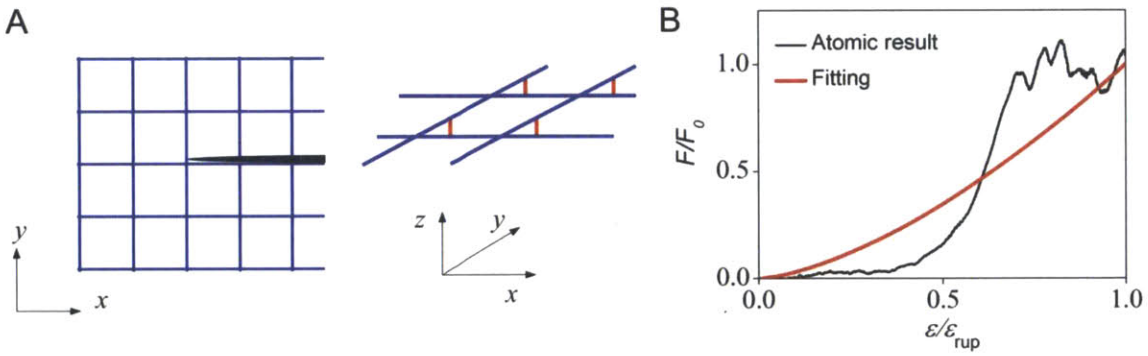


**Fig. 4.6 Structural and mechanical properties of IFs and IF networks (Qin and Buehler, 2012b).** A, The configuration of the network structure near the crack tip used in this study: blue for the IF, red for the crosslink and black shadowed part for the one end of the initial crack. B, The force-strain relationship of a full length filament. This plot contains both the result of atomic simulation and the corresponding fitting curve with a result of $\boldsymbol{\varepsilon_{rup} = 2.6}$ and $N$=1.5.

We use a mesoscopic model to describe each IF as a series of beads interacting according to nonlinear interparticle multibody potentials. The total energy is given by:

$$E_x = \sum_{\text{pair}} \varphi_T(\varepsilon) + \sum_{\text{triplets}} \varphi_B(\theta). \tag{4.3}$$

For general purpose, the force-strain curve $F_T(\varepsilon)$ of each single IF is modeled by a power-law function as:

$$F_T(\varepsilon) = -\partial\varphi_T(\varepsilon)/(r_0\partial\varepsilon) = F_0(\varepsilon/\varepsilon_{rup})^N f(\varepsilon) \tag{4.4}$$

where $F_0$ is the strength of a full length filament, $\varepsilon_{rup}$ is the corresponding strain for $F_0$ and $N$ is the so-called hardening exponent that describes the nonlinear stress-strain response of a material. For a crosslink, the force response under deformation is given by a similar expression as Eq. 4.4 except for that the strength is given by another independent term $F_{c\_0}$. For the hardening exponent, $N$<1 denotes softening behavior (also referred to as "elastic-plastic") of the material, $N$=1 denotes linear behavior and $N$>1 represents a stiffening material (Qin and Buehler, 2011a). The expression $f(\varepsilon)$ is a cut-off function as $f$=1 for $\varepsilon < \varepsilon_{rup}$ and $f$=0 for $\varepsilon \geq \varepsilon_{rup}$; and typical force-extension curves of a full length filament is given in Fig. 4.6B (Qin et al., 2009b). For simplicity, the force expression included in this study is normalized by the strength of the full length filament. The bending energy of each filament is given by:

$$\varphi_B(\theta) = \frac{1}{2}k_B(\theta - \theta_0)^2 \tag{4.5}$$

with $k_B$ relating to the bending stiffness of the IF $EI$ through $k_B = 3EI/r_0$. $EI$ relates to the IF persistence length $L_P$ through $EI = L_P K_B T$, where $K_B$ is the Boltzmann constant and $T$ is the temperature. All the parameters of the modeling are as summarized in Table 4.1.

**Table 4.1 Geometric and numerical parameters for the computational model.**

| Parameter and units | Numerical value |
|---|---|
| Equilibrium bead distance $r_0$ (in nm) | 5 |
| Equilibrium distance of crosslink $r_{c\_0}$ (in nm) | 2 |
| Filament diameter $D$ (in nm) | 10 |
| Lattice constant $d$ (in nm) | 50 |
| Strength of each filament $F_0$ (in nN) | 7.9 |
| Overall hardening exponent $N$ | 1.5 |
| Bond breaking distance $\varepsilon_{rup}$ | 2.6 |
| Equilibrium angle $\theta_0$ (in rad) | $\pi$ |
| Bending stiffness parameter $k_B$ (in kcal/mol/rad$^2$) | 169.51 |
| Mass of each mesoscale particle (in amu) | 230913 |
| Density $\rho$ (in kg/m$^3$) | 260 |

The meshwork model shown in Fig. 4.6A includes 24 filaments in the $y$-direction (1.2 μm) and 24 filaments (1.2 μm) in the $x$-direction, with a crack-like defect added in the center to mimic a structural imperfection. Filaments at the orthogonal corners are mechanically cross-linked by chemical interaction in our model. All simulations reported here are carried out in two steps by LAMMPS package (Plimpton, 1995). First, we perform a relaxation during which we equilibrate the system. Relaxation is achieved by energy minimization, heating up

the system from 0 to 300 K, and then annealing the structure at a temperature of 300 K. Second, we perform a loading simulation during which we keep the system at 300 K and apply a constant strain rate of $8.0 \times 10^{-3}\ \mathrm{ns}^{-1}$ to continuously increase the loading applied to the bottom and top layers of beads.

To examine the effect of the crosslink strength on the failure mechanism of IF network, we apply tensile force to the IF network with different crosslink strengths, $F_{c\_0}$. The conformational changes of the networks under tension with two typical crosslink strengths are as summarized in Fig. 4.7. The network models of $F_{c\_0} = F_0$ and $F_{c\_0} = 0.2F_0$ show rather different deformation and failure mechanisms under tension as visualized in Figs. 4.7A and B, respectively. It is observed that for the case with strong cross-links ($F_{c\_0} = F_0$), the network fails by breaking filaments at the crack tip with the increasing tensile force and the crack propagates in the initial direction of the initial crack orientation. For the network with weaker cross-links ($F_{c\_0} = 0.2F_0$) the crack does not propagate. Rather, the tensile force unpins the filaments in the $x$-direction from the filaments in the $y$-direction by breaking the crosslinks. This failure mechanism facilitates a "diffusion" of the deformation energy at the crack tip and renders the deformation within the filaments more uniform in the $y$-direction. This can be directly confirmed in the visual representations. Moreover, this unpinning step affects the flaw tolerance of the network material by increasing its tensile strength as shown in Fig. 4.8A. The overall strength $F_{net}$ of the entire network increases from $15.0F_0$ to $18.4F_0$, and the failure strain increase from 2.2 to 2.5 as the strength of the crosslinks decreases from $F_0$ to $0.2F_0$.

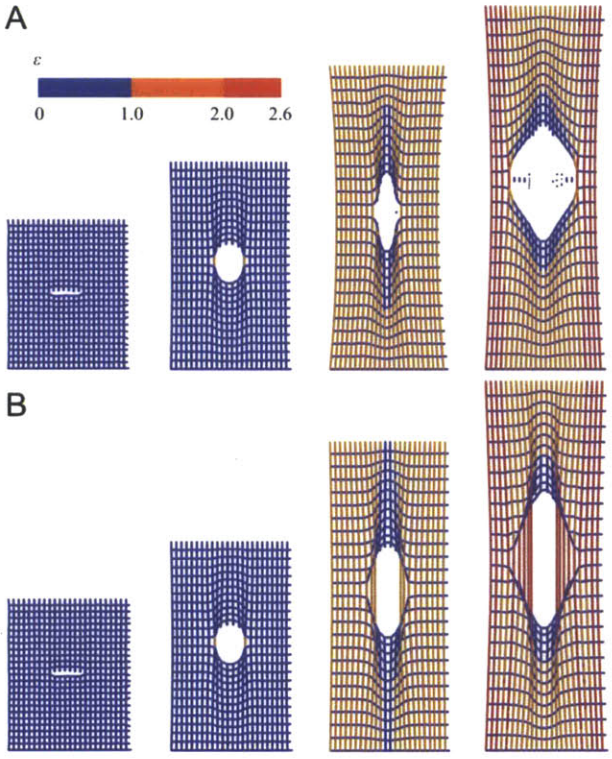


**Fig. 4.7 Simulation snapshots of the conformations of IF networks under different applied strains (Qin and Buehler, 2012b)** (from left to right) of 0.22, 0.70, 1.50 and 2.00. A, IF network with crosslink strength of $\boldsymbol{F_{c\_0} = F_0}$. B, IF network with crosslink strength of $\boldsymbol{F_{c\_0} = F_0}$. Each of the filaments is colored according to its local tensile strain as given by the color bar depicted in Panel A.

We now study the maximum stress of the network by using $\sigma_F = F_{net}/(24dD)$, where $d$ is the lattice constant of the network and $D$ is the diameter of the filament. Its relationship with the strength of the crosslinks is as shown in Fig. 4.8B. Instead of a gradual transition, the

decreasing strength of the crosslink increases the maximum stress of the network exponentially, and by 23% between $F_{c\_0} = 0.5F_0$ and $0.2F_0$. This leads to the most important result of this paper: a relatively weaker crosslink increases the strength of the overall IF network. This result is counterintuitive but makes sense because the rupture of crosslinks before reaching the strength limit of the filaments at the crack tip efficiently decreases the force concentration at the crack tip. Thereby, it efficiently increases the maximum applied loading before failure occurs.

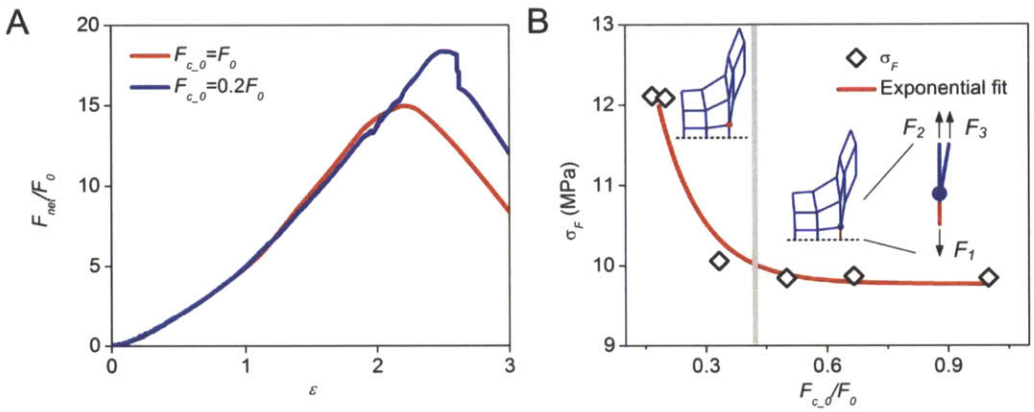


**Fig. 4.8 Mechanical response of IF network under tension (Qin and Buehler, 2012b).** A, Overall force-extension curve of the network with strong crosslinks ($\boldsymbol{F_{c\_0} = F_0}$) and weak crosslinks ($\boldsymbol{F_{c\_0} = 0.2F_0}$). B, The tensile strength of the network with different crosslink strengths. The weak crosslink increases the tensile strength of the network by switching the failure mechanism from failure of filaments at the crack tip (right to the bar) to failure of the crosslinks (left to the bar). The gray bar corresponds to the critical condition that $\boldsymbol{F_{c\_0} = 0.42F_0}$ as obtained.

To find an analytical solution of the particular crosslink strength that leads to an increased robustness of the IF network, we assess the geometric details and force distribution around the crack tip. Based on the fact that the initial crack deforms to an elliptical shape before failure we have $\left.\frac{dx}{dy}\right|_{x=a} = 0$ at the crack tip along the inner crack surface. Therefore, including the fact that IFs are flexible in bending, the balance of force in tension is achieved via $F_1 = F_2 + F_3$, where $F_1$ is the tension force within the filament at the crack tip, $F_2$ is the tension force exerted from the neighboring lattice in the tensile direction, and $F_3$ is the tension force exerted from the crosslink as illustrated in Fig. 4.8B. The rupture condition of the filament at the crack tip is $F_1 = F_0$, which corresponds to the rupture strain $\varepsilon_{rup}$. Under the condition that there is no rupture event of crosslinks, the applied tensile force to the network near the crack tip is proportional to $1/\sqrt{r}$ (Freund, 1990), where $r$ is the distance to the crack tip. We have $F_2 = F_1(\sqrt{r_1/r_2})$ where $r_1$ is the distance from the middle of the filament with $F_1$ in tension to the crack tip and $r_2$ is the distance from the middle of the filament with $F_2$ in tension to the crack tip. Therefore, the condition

$$F_3 < F_0[1 - (\sqrt{r_1/r_2})] \tag{4.6}$$

is the necessary condition to prevent rupture of the filament at the crack tip before rupture of the crosslink occurs. As we have $r_1 = 0.5$d and $r_2 = 1.5d$ for the geometry of this lattice model, $F_3 < 0.42F_0$ as the necessary condition is obtained (as shown in Fig. 4.8B). Indeed, it is shown by our simulations that networks with crosslinks weaker than this critical value are stronger under tension. It is also noted that this condition does not directly correspond to the maximum strength because of the nonlinearity of the stress distribution around the crack tip of such a strain-hardening material.

To investigate if this unpinning process exists for materials with mechanical responses that are significantly different from what IF display, we test other two materials with typical force-extension curves of $N$=0.5 and $N$=1.0 as given by Eq. (2). Each of them represents a strain-softening and elastic material, respectively. For each of the materials, we obtain the stress-extension curves for crosslink strengths of $F_{c\_0} = F_0$ and $0.2F_0$ as shown in Fig. 4.9A and B, respectively. We find that the increments of the network strength caused by the weak crosslink of those two materials are only 1% and 11%, which are significantly smaller than that of the strain-hardening material as for IF network (23%) as summarized in Fig. 4.9C.

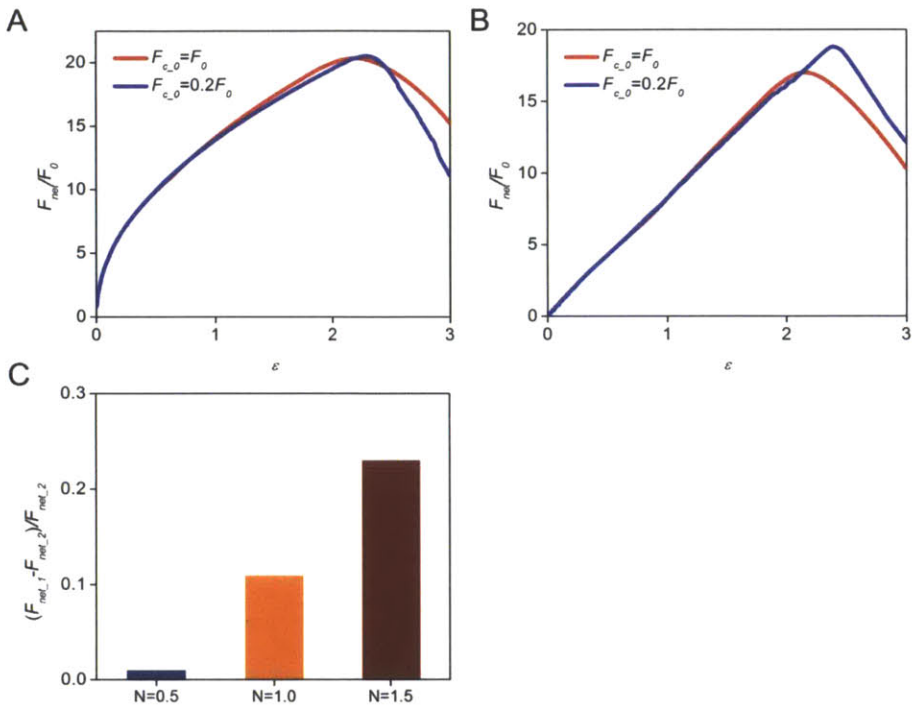


**Fig. 4.9 Force-extension curve of networks with different mechanical characteristics under tension (Qin and Buehler, 2012b).** A, By using $N$=0.5 in Eq. 4.4 to give the characteristic of strain-softening materials. B, By using $N$=1 in Eq (2) to give the characteristic of linear elastic materials. Each of those networks is test with two typical crosslinks strengths $\boldsymbol{F_0}$ and $\boldsymbol{0.2F_0}$. C, Increment of the strength of the network ($\boldsymbol{F_{net\_1}}$) with weak crosslinks ($\boldsymbol{F_{c\_0} = 0.2F_0}$) comparing to that ($\boldsymbol{F_{net\_2}}$) of the network with strong crosslinks ($\boldsymbol{F_{c\_0} = F_0}$). Results of three typical materials with different $N$ are summarized here for comparison.

## 4.3 Experimental evidence of nuclear lamina mechanics

Specific molecular mechanisms that act at different levels of strain control this change of the "local" value of $N$ (in Fig. 4.10A). Lamin filaments initially feature their typical structure as intact bundles of coiled-coils (Fig. 4.10B), where clusters of hydrogen bonds are arranged in series and grouped in α-helical turns. This geometry facilitates the unfolding of α-helical loops after reaching the limit of elastic deformation at 50%. The unfolding force until all α-helical loops are unfolded is basically constant for long coils, leading to a strong softening behavior (which can be referred to as "ideal elastic-plastic") and thus a hardening exponent of $N \to 0$. Further loading causes polypeptide strands to be fully unfolded, squeezed together driven by hydrophobic interactions and eventually undergoing a transition into beta-sheets. The structure after this alpha-to-beta transition exhibits a stronger ability to withstand forces because many clusters of hydrogen bonds are loaded in parallel and deform cooperatively (Qin and Buehler, 2010c; Qin and Buehler, 2012c), leading to a severe increase of the force and stiffness as loading is further increased.

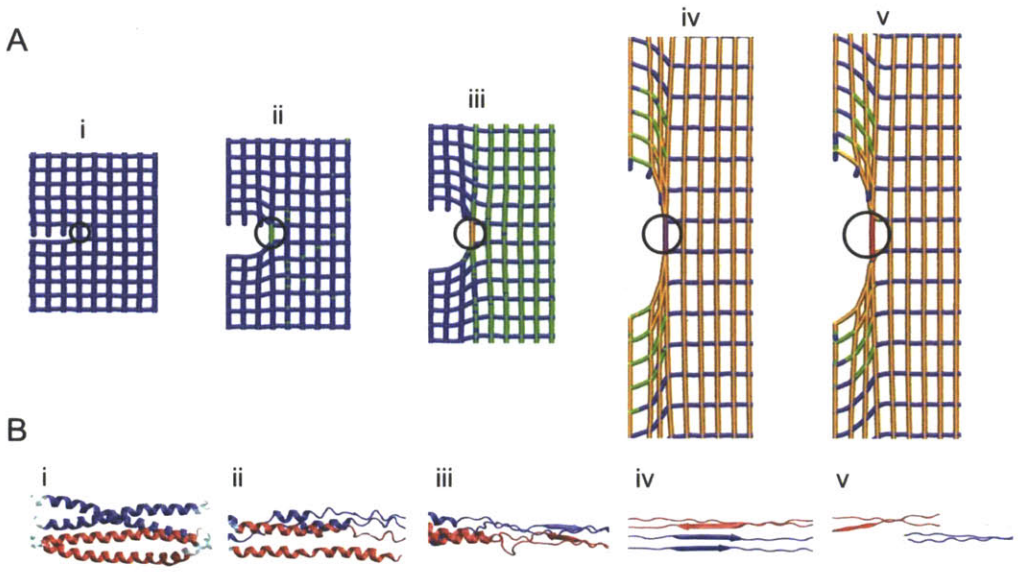


**Fig. 4.10 Deformation of the lamin filaments around the crack tip under uniaxial loading at certain strain level (Qin and Buehler, 2011a).** A, Snapshots of the meshwork geometry near the crack tip at applied strains of i: $\boldsymbol{\varepsilon_y = 17\%}$, ii: 42%, iii: 58%, iv: 160%, v: 161%; The crack length is $\boldsymbol{2a/b = 6}$ and each filament is colored according to its structural character. B, Visualization of the molecular structure of the IF under stretching. The structural character of the filament ahead of the crack tip (marked by a circle in a) is shown at different strains, corresponding to the strain levels shown in snapshots i–v in a (the local strain at the filament considered here is $\boldsymbol{\varepsilon = 40\%}$, 50%, 90%, 190%, and 220% and thus generally larger than the applied strain).

This results in severe stiffening and is captured in a hardening exponent of $N \gg 1$. An increasing loading causes first sliding and then rupture of the entire filament, leading to a final softening behavior at very large deformation. This analysis shows that the softening and stiffening behavior, described by changes in the "local" hardening exponent $N$, is caused by secondary structure transitions at the molecular level at the nanoscale.

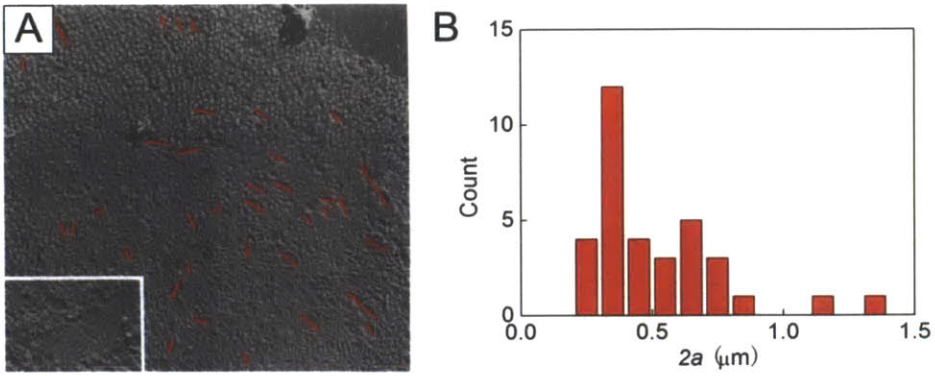


**Fig. 4.11 The experimental image of nuclear lamina of *Xenopus* oocytes and the distribution of imperfect on the network material.** Panel A, adopted from(Aebi et al., 1986). Freeze-dried/metal-shadowed nuclear envelope, revealing the structure of nuclear lamina meshwork partially covered with arrays of nuclear pore complexes (bars, 1μm). Imperfections on the meshwork are highlighted by red bars for their long axis. Panel B, The histogram of lengths of the imperfections as shown in panel A.

Finally, in order to identify the flaw-tolerance ability of the material for varied defect sizes, we investigate the failure strain $\varepsilon_F$ of the meshwork as a function of the crack length a as shown in Fig. 4.12A. The results depicted in Fig. 4.12A show that the failure strain is largely insensitive to the presence and size of cracks, and that the failure strain approaches a constant value even as the defect size grows. Considering Eq. 4.1 we empirically fit the $\varepsilon_F - a$ relation by

$$\varepsilon_F = \varepsilon_{F0}\left(\frac{2a}{d}\right)^{-\frac{1}{1+N}} \tag{4.7}$$

where $\varepsilon_{F0}$ = 196% corresponds to the highest failure strain at $2a = d$ (for the case where no crack is present, or a perfect meshwork), and $N$ = 7.6 is the hardening exponent of nuclear lamina before failure (as defined in section 4.2.3). For the case of biaxial loading with $\varepsilon_x = \varepsilon_y$, we obtain $\varepsilon_{F0}$ = 197% and $N$ = 6.8. It is noted that we confirmed that as we change the parameters $h$, $l$, and $d$ we find the parameters ($\varepsilon_{F0}$, $N$) do not change with those variations. The voids of nuclear lamina in experimental studies are observed to be up to on the order of 1.4 μm, (Fig. 4.11), leading to $\varepsilon_F$ = 128%. This analysis explains the phenomenon that the integrity of nuclear lamina is not greatly affected by a single or larger number of clusters (for example, a conglomerate of several nuclear pores), representing a flaw-tolerant material.

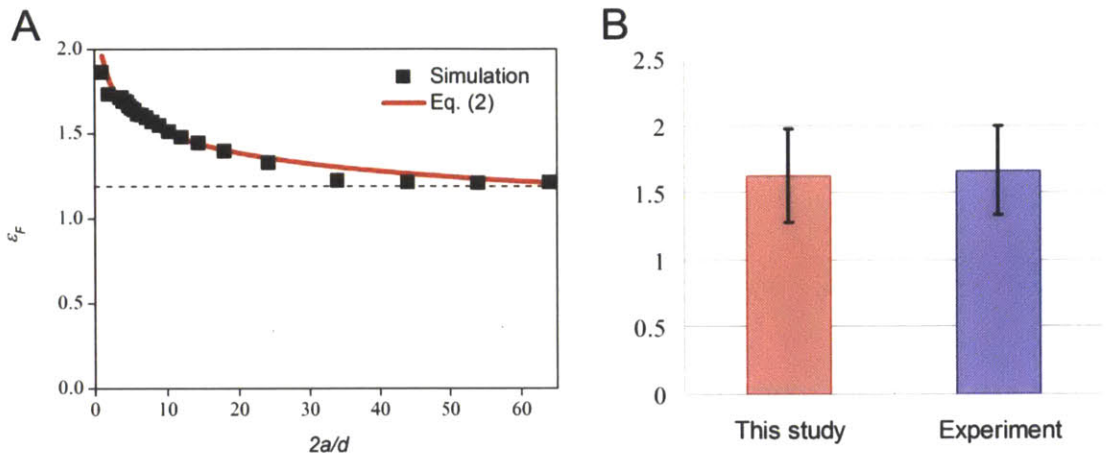


**Fig. 4.12 Failure strain of the meshwork as a function of initial crack length, here quantified in normalized form (crack length normalized by the lattice constant *d*) (Qin and Buehler, 2011a).** A, Failure strain of the meshwork for varied crack sizes. The results show that the failure strain is largely insensitive to the presence and size of cracks, and that the failure strain approaches a constant value of 128% in the asymptotic limit for very large crack sizes. B, The comparison of $\boldsymbol{\varepsilon_F}$ between results obtained in this study with a characteristic defect size and the experiment of the axial extensibility of nuclear lamina gel (Panorchan et al., 2004). The data compares well and provides validation for the results obtained from our computational model.

Our results also explain recent experimental stretching tests of gels of nuclear lamina, where the material has been found to exhibit a large axial strain before failure in the range of 133%-200% (Panorchan et al., 2004). This agrees with our finding that the failure strain of the nuclear lamina is between two bounds of 128%-197%, as shown in Fig. 4.12B. Comparing with the failure strain measured for the entire nuclear envelope (in the range of 50%-60% strain (Dahl et al., 2004)), the nuclear lamina is found to be much more extensible, and much greater than the deformation that can be generated by microtubules (<50% (Janmey et al., 1991)) that impinge on the nuclear envelope (Beaudouin et al., 2002). Therefore, external deformation applied outside the cell are likely not sufficient to cause the rupture the nuclear lamina by mechanical signal transduction through microtubules. These results, together with the fact that the integrity of the nuclear lamina only breaks down during mitosis through breakdown processes, suggest that even if there exists a structural flaw, the nuclear lamina is a reliable structure that effectively protects genetic material from extreme external force and deformation applied on the cell, which will not result in rupture of the nuclear lamina unless there is further biochemical modification or mutations that affect its mechanical property to lead to a loss of flaw tolerance. Although the accuracy of this result may be distorted since the gel is composed of lamins in random orientations, it is the only experimental result that quantitatively provides an estimate of the deformation capacity of nuclear laminas. We use this result to carry out the comparison here but are cognizant that future experimentation validations are required to fully understand all the mechanical properties of nuclear laminas. We note that other nuclear lamina models with different

geometries have been proposed in other works (Goldberg et al., 2008a; Goldberg et al., 2008b; Rowat et al., 2005). Since both the in situ and in vitro experiments of somatic nuclear lamina are either not feasible or too difficult to carry out (Goldberg et al., 2008a), it is hard to tell which model is more immediately related to human nuclear lamina. Since our model can in principle be readily adopted to different sets of geometries and mechanical parameters it may be used as a tool to determine which model is more realistic by comparing against future *in vivo* mechanical test in experiments. It is also noted that within our model we consider imperfections, defects, and heterogeneities simply as crack-like defects, which is a highly simplified representation since the biological model of defects can be more complex. For example, different models of the effect of the nuclear pore complex on the nuclear lamina have been discussed, and those models either consider a nuclear pore complex as a relatively weakly associated deformable unit similar to a void or strongly associated rigid complex similar to a rivet (Rowat et al., 2005). Although there is some experimental evidence that nuclear pore complexes act like rivets (Rowat et al., 2005), there is also evidence that rupture and breakdown of nuclear envelopes tend to occur around nuclear pore complexes (Djaczenk.W et al., 1973). The improvement of defect modeling of nuclear pore complexes requires more information of the interaction between the complex and nuclear lamina and has yet to be established.

The rapid propagation speed of nuclear lamina meshwork can reflect the behavior of cell nuclei in divisions from mechanical aspects. It shows that once the extreme loading condition is reached, the crack propagates in a fast (intersonic) form. This behavior can explain the experimental observations that the nuclear envelope breakdown processes during cell divisions are found be short and irreversible. For human somatic cells, the chromatin is tightly associated with the nuclear lamina, which may by some extend slow down the crack propagation. However, neither *in situ* nor *in vitro* experiments of somatic nuclear laminas are feasible for us to improve our model to suit for somatic cells nuclei. We hope our study can trigger broad interests in studying dynamic failure of cell nuclei and the more complicated somatic nuclear lamina model has yet to be established.

The multi-scale method used here provided a powerful bridge to overcome the four orders of magnitudes difference in length scales to appropriately describe the characteristic of catastrophic failure in the nuclear lamina meshwork. Based on this method, it may also be possible study the effect of disease caused by point mutations and their effect on the mechanical and failure properties of nuclear laminas. The approach used here could also be applied to other hierarchical biological materials and provide insight into their dynamical failure mechanisms. More work is needed to develop a solid theoretical foundation for fracture in discrete nonlinear systems as studied here, and to provide a deeper investigation of the effect of solvent and chromatin on crack dynamics.

In summary, we studied two different failure mechanisms of IF networks under tension. The strength of the crosslink between the filaments plays a critical role in switching the failure mechanism of the network, where the unpinning process is the key mechanism to enable this behavior. Comparing to the failure of the network with strong crosslinks, networks with relatively weak crosslinks are 23% stronger than the former. We compared this result to other materials with different mechanical responses and find this switching function

controlled by crosslink strength is only significant for strain-hardening materials. This mechanical characteristic of IFs-a significant stiffening of the material behavior with larger deformation-is indeed shared by many biological materials including spider silk, amyloids and collagen, and many others. Thus our model could have much wider applications.

# 5 The molecular mechanism of rapid aging disease

Hutchinson-Gilford progeria syndrome (HGPS) is a premature aging syndrome caused by the expression and accumulation of a mutant form of lamin A, Δ50 lamin A. As a component of the cell's nucleoskeleton, lamin A plays an important role in the mechanical stabilization of the nuclear envelope and in other nuclear functions. It is largely unknown how the characteristic 50 amino acid deletion affects the conformation of the mostly intrinsically disordered tail domain of lamin A. Here we perform replica exchange molecular dynamics simulations of the tail domain and determine an ensemble of possible conformations. Based on these structures we show that the ZMPSTE 24 cleavage site on the precursor form of the lamin A tail domain orients itself in such a way as to facilitate cleavage during the maturation process. We confirm our simulated structures by comparing the thermodynamic properties of the ensemble structures to *in vitro* stability measurements. Using this combination of techniques, we compare the size, heterogeneity of protein shape, thermodynamic stability of the Ig-fold, as well as the mechanisms of force-induced denaturation. Our data shows that the Δ50 lamin A tail domain is more compact and displays less heterogeneity than the mature lamin A tail domain. Altogether these results suggest that the altered structure and stability of the tail domain can explain changed protein-protein and protein-DNA interactions and may represent an etiology of the disease. Also, this study provides the first molecular mechanics study of the lamin A tail domain, which is confirmed by thermodynamic tests.

## 5.1 Background on rapid aging disease and function of lamin A tail

The nucleoskeleton of a cell, located at the inner surface of the inner nuclear membrane, is composed mainly of IFs made of either A-type and B-type lamin protein along with other accessory proteins (Wilson and Berk, 2010). A-type lamins, primarily lamin A and lamin C, are spliced from the *LMNA* gene. B-type lamins are encoded by *LMNB1* and *LMNB2*. Lamin A is an A-type lamin of particular mechanical interest since the loss of lamin A appears to influence nuclear mechanics more than other A-type lamins or B-type lamins (Lammerding et al., 2006). Conversely, a loss of lamin A has no apparent defect in mice aside from some nuclear weakening as long as other A-type lamins are present (such as lamin C) (Fong et al., 2006). This 'survivability' may be a reason that the *LMNA* gene has more than 100 disease-causing mutations. Mutations in different regions of the *LMNA* gene lead to alterations in different tissue types including fat, muscle, and brain as well as different aging disorders (Worman et al., 2010). This group of diseases, collectively termed laminopathies, has led to a considerable interest in lamin A. Hutchison Gilford progeria syndrome (HGPS) is a segmented premature aging syndrome caused by a mutation in *LMNA* (Goldman et al., 2004).

## 5.2 Molecular modeling of lamin A tail

The tail domain of lamin A is mostly disordered and demonstrates the characteristic qualities of intrinsically disordered proteins (Rauscher and Pomes, 2010) including a promiscuity in protein binding (Schirmer and Foisner, 2007; Zastrow et al., 2004), tendency to aggregate with a high proline and glycine content (Linding et al., 2004). It is difficult to predict how the removal of 50 amino acids in a region lacking secondary structure will affect the overall structure of the protein domain. Disordered regions are typically difficult to crystallize and take on many conformations, making traditional structural analyses such as X-ray crystallography and NMR challenging (Krimm et al., 2002). Instead, here we use REMD simulations to determine an array of semi-stable structures based on ordered secondary structures (Sugita and Okamoto, 1999). REMD has been shown to be successfully utilized as a computational method used to improve the dynamic properties of conventional Molecular Dynamics and Monte Carlo methods, aiming at obtaining global-minimum free energy states of polymers by overcoming kinetic trapping without giving any specific initial structures (Liu et al., 2005; Snow et al., 2005; Sugita and Okamoto, 1999; Zhou et al., 2001). Nevertheless, this method can reduce accuracy when it is applied to extremely large systems (Snow et al., 2005). We focus on the amino acid sequence of the tail domains and apply massively parallelized computational power to study their intrinsically disordered structures (Liu et al., 2005). When taken together, these structures represent the spectrum of conformations of the mwt LA and Δ50 LA tail domains. Then, we computationally and experimentally probe the protein stability to determine global structural changes in the tail domains. These structural changes likely impact binding, filament formation as well as protein stability. Specifically, we test the stability of the structured Ig-fold, which has previously been examined in other laminopathies (Krimm et al., 2002; Shumaker et al., 2005). However, an altered stability has only been observed for point mutations which occur in the Ig-fold. By combining data obtained from experiment and simulation, we extract information on changes in the stability of both normal and the protein mutant and develop a mechanistic model of higher-level nuclear structural and mechanical changes in diseased and normal states.

### 5.2.1 Amino acid sequence and initial structural of lamin A tail

Here we start with the sequence of Homo sapiens laminA/C (SwissProt/TrEMBL accession number P02545) for the prelamin A (AA428-664). The sequence of the mwt LA is obtained by removing 18 residues in the C-terminal, and the sequence of progerin, the mutant, is obtained by deleting the Δ50 (AA607-656) from that of the prelamin A (we will discuss the detail in section 5.3). Initially, the structure of the s-type Ig-fold of the tail domain is modeled from the starting conformation available from the protein database (PDB with ID 1IVT (Krimm et al., 2002)), and the remaining tail domain is given an initial guess of conformation. Two extreme initial structures, straight and alpha helix, has been applied in the study. The amino acids are connected by taking $\phi = 180^{\circ}$ and $\psi = 180^{\circ}$ for the straight form, and by taking $\phi = -58^{\circ}$ and $\psi = -47^{\circ}$ for the alpha-helix. Note that the parameters $\phi$ and $\psi$ are two characteristic dihedral angles that define the conformation of the protein backbone chain; these angles largely define how two neighboring amino acids are connected to one another.

### 5.2.2 Genetic cause of rapid aging disease: 50 amino acid deletion

Lamin A is a characteristic type V IF protein that contains a globular N-terminal head, a segmented coiled-coil α-helical rod domain and a C-terminal tail containing an immunoglobulin (Ig)-fold (Herrmann et al., 2007). Lamin proteins are unique from other IFs as they feature an exceptionally long C-terminal tail domain (Herrmann et al., 2007). The Ig-fold binds DNA and many other nuclear proteins (Zastrow et al., 2004). The C-terminus of the tail domain undergoes post-translational processing, where the precursor form of lamin A is farnesylated, carboxymethylated localized to the inner nuclear membrane (Coffinier et al., 2010) and then the last 18 amino acids are cleaved by an endoprotease ZMPSTE-24 to produce mature wild-type lamin A (mwt LA) (Young et al., 2005a). In HGPS, a single point mutation in the *LMNA* gene activates a cryptic splice site causing 50 amino acids encoded by exon 11 to be deleted, and the resulting mutant protein is called Δ50 lamin A (Δ50 LA) (De Sandre-Giovannoli et al., 2003). The deletion in Δ50 LA includes the ZMPSTE-24 cleavage site resulting in the retention of the C-terminal farnesylation, which is suggested to be responsible for the accumulation of Δ50 LA at the inner nuclear membrane (This mechanism will be extensively discussed in Chapter 6). Similarly, the loss of the ZMPSTE-24 protease causes an accumulation of the precursor lamin A protein, prelamin A, at the inner nuclear membrane (Navarro et al., 2004; Taimen et al., 2009). However, the retained farnesylation cannot explain all of the molecular changes in HGPS. Recently, *in vitro* binding assays have shown differential binding of Δ50 LA to nuclear proteins and chromatin (Bruston et al., 2010). Two transgenic mice models containing an unfarnesylated Δ50 LA showed varied, but present, clinical pathology (Davies et al., 2010; Leuba et al., 1994; Yang et al., 2011). These results suggest that the loss of 50 amino acids from the lamin A tail may alter the protein more than simply retaining a farnesylation (Young et al., 2006).

### 5.2.3 Replica exchange method for structure refinement

All protein structure identification is carried out by using the REMD method (Sugita and Okamoto, 1999) implemented in the CHARMM c35b1 simulation software (Brooks et al., 1983). The replica management and conformation analysis are done by using the MMTSB script package (Feig et al., 2004). REMD is a simulation method used to improve the dynamic properties of Monte Carlo method, aiming at obtaining global-minimum free energy states. REMD samples a wide conformation space and avoids getting trapped in local-minimum free energy states because of the thermal stimulation by high temperature replicas, and it allows one to find stable structures at the replica with lowest temperature. The main steps of the method are summarized in Fig. 5.1, and the inputs for this method are the peptide sequence and an initial guess of conformation. Temperatures for replicas exponentially increase from the lowest to the highest, as a function of:

$$T_i = T_{min}(T_{max}/T_{min})^{(i-1)/(n-1)} \tag{5.1}$$

where $T_{min} = 300\,K$ is the lowest sampling temperature, and $T_{max} = 800\,K$ is the maximum sampling temperature in this study.

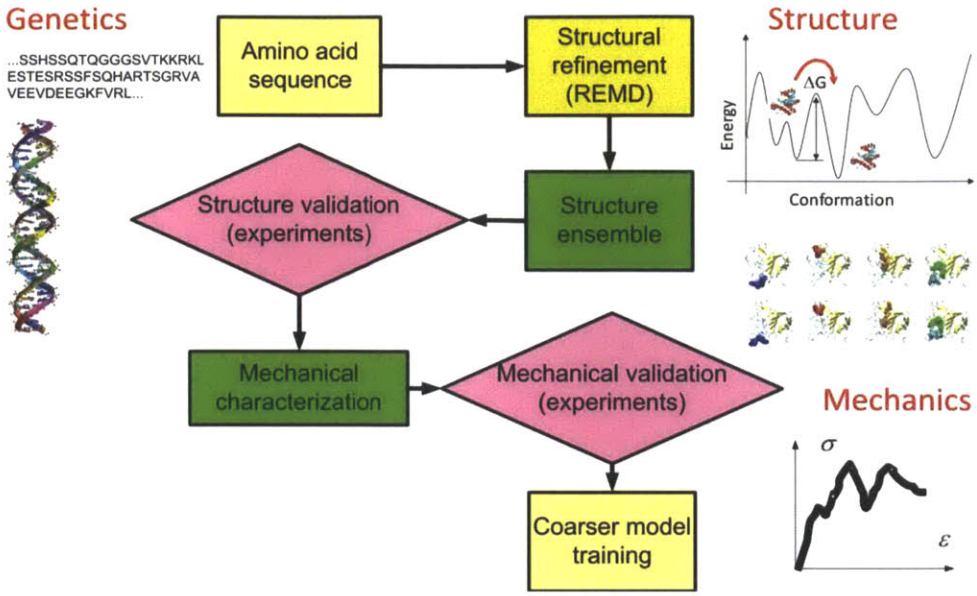


**Fig. 5.1 A schematic of the overall procedure to investigate the molecular structure and mechanical property of IFs by computational modeling and simulations and validation by comparison against experimental tests (Qin and Buehler, 2012a).**

Each REMD cycle includes an equilibrium interval and an exchange event. The equilibrium time between two exchange events (done by CHARMM) is set to be 0.5 ps. The interacting force and energy among particles is defined by the CHARMM19 all-atom energy function and an implicit Gaussian model for the water solvent. Each exchange event compares the energy of the configuration within two replicas with closest temperature. The Metropolis criterion is used to judge whether or not the configurations exchange between the higher and lower temperature replicas.

To increase the sampling speed, we apply massive parallel computing (use MPI to run many CPUs in parallel) to accomodate many replicas. For the Δ50 configuration calculation, we keep searching for structures with minimal energy by 32 replicas until the convergence of the energy. For the wild-type tail and progerin tail configuration calculation, we use 128 replicas (with 128 CPUs) to accelerate simulation for this larger model. The above setting up of the calculation provide a uniform and sufficiently large acceptance ratios (>30%) for computational efficiency.

For each structure calculation, we perform 20,000 cycles (equals to 10 ns for each replica). The conformation energy of the replica with $T_{min}$ converges within the first 10,000 cycles and we use conformations within the later 10,000 cycles of the lowest temperature (of $T_{min}$) for structure analysis. We classify the structures according to mutual similarity, and K-means algorithm is used to identify conformation clusters with root mean square deviation less than 2 Å. For each structure cluster, we select the conformation with lowest energy. The significance factor is defined as the number of conformation within a cluster divided by the total conformation number. All statistic results based on conformations are weighted by the significance factor.

## 5.3 Structure and mechanics of lamin A tail

By applying REMD, we identify folded structures of different segments within the tail domain of LA. As shown in Fig. 5.2, the segments include AA607-656 (Δ50) for the 50 amino acids coded in exon 11 that are missing in the Δ50 LA mutation (sequence in Fig. 5.2A), AA428-646 for the mwt LA tail domain (sequence in Fig. 5.2B) and AA428-614* for the Δ50 LA (sequence in Fig. 5.2C).

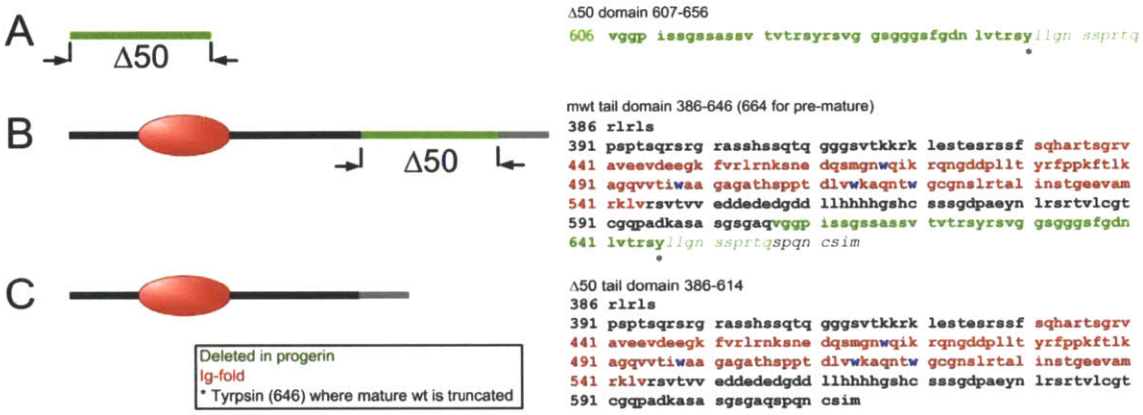


**Fig. 5.2 Schematic of the sequences of lamin tail domains investigated in this study (Qin et al., 2011).** A, The segment of amino acids deleted in the Δ50 LA tail. B, The mwt LA tail ends at tyrosine 646 (*), and the remaining residues (italics) are cleaved during posttranslational processing (these residues are included in our simulations). C, Δ50 LA, also called progerin, has lost 50 amino acids (green) including the proteolytic site. Thus, Δ50 LA ends at a different 614, which we call 614*.

### 5.3.1 Molecular structure of the 50 amino acid deletion

Since the Δ50 region from exon 11 is lost in Δ50 LA, we first examine the folded conformation of that region alone. To increase the sampling space we consider two extreme initial conformations: a straight conformation and an α-helical conformation. This strategy has been effectively performed in earlier REMD studies applied to investigate protein structures (Liu et al., 2005). Possible conformations of the Δ50 domain, that is, those associated with cluster of highest significance factors and of lowest energies in the clusters are listed in Figs. 5.3A and 5.3B. There are no dominant conformations for the structure based on the energy calculations of the different structures. The average end-to-end length of this segment is determined to be 10 ± 3.9 Å, obtained by statistical measurement of all the conformations generated. The flexibility of this segment is confirmed by comparing this end-to-end length with the contour length of 175 Å. These observations correlate with the experimental finding that the structure of this domain is amorphous and flexible (Kobayashi et al.; Krimm et al., 2002). We confirm that two sets of initially differently folded structures converged to similar conformations characterized by the secondary structure distribution as shown in Fig. 5.3C. Fig. 5.3C clearly shows that the generated structures have a secondary structure of intrinsic disorder, with >80% turns and coil. This is consistent with our collaborator's experimental

Circular dichroism (CD) measurements, which show a high glycine content (20%) in this region that may be the source of the high flexibility of this segment. We observe a relatively higher α-helix character for Δ50 segments that were initialized as a pure α-helix (Fig. 5.3B). The α-helix character is retained near the C-terminal of this Δ50 domain around AA645 (8 AAs) and 623 (6 AAs), suggesting that they are more stable than the other parts.

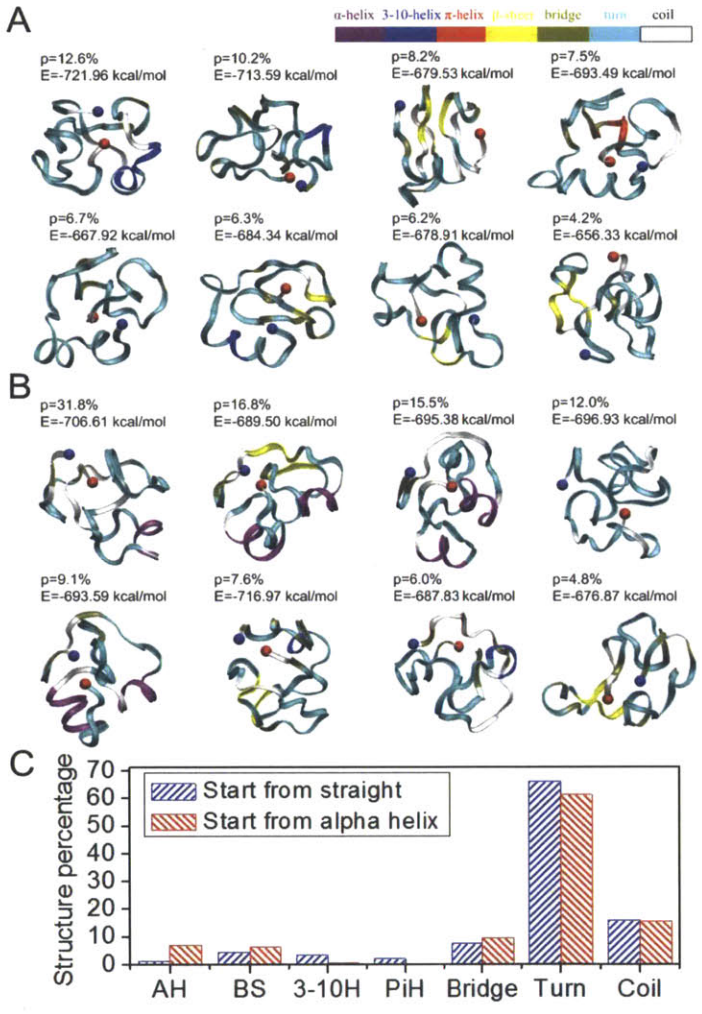


**Fig. 5.3 Conformations of the 50 amino acid segment of exon 11 with high significance factors (Qin et al., 2011).** Simulations of protein folding with initial conditions of (A) straight and (B) α-helix show similar final results, which are mostly disordered. Each amino acid is colored according to their secondary structure. The significance factor ($p$) as well as the potential energy ($E$) is marked for each conformation. The starting point (AA607) is in blue and the end point (AA656) is in red; C, Secondary structure of the 50 amino acid segment shows little structure.

Another intriguing character of the Δ50 region is that the section AA645-647 is always found on the outside of the structure with side-chains of the amino acids pointing outward (Fig. 5.3 in red). AA645-647 is regarded as the site of endoproteolytic cleavage by the protease, ZMPSTE-24, cleaving prelamin A to mwt LA (highlighted in Fig. 5.4) (Navarro et al., 2004; Taimen et al., 2009). Our computational results suggest that this "substrate" region faces outward possibly to facilitate interacting with the protease. This location may be critical to ensure the fast protease reaction kinetics of premature lamin A cleavage observed in cells (Liu et al., 2010).

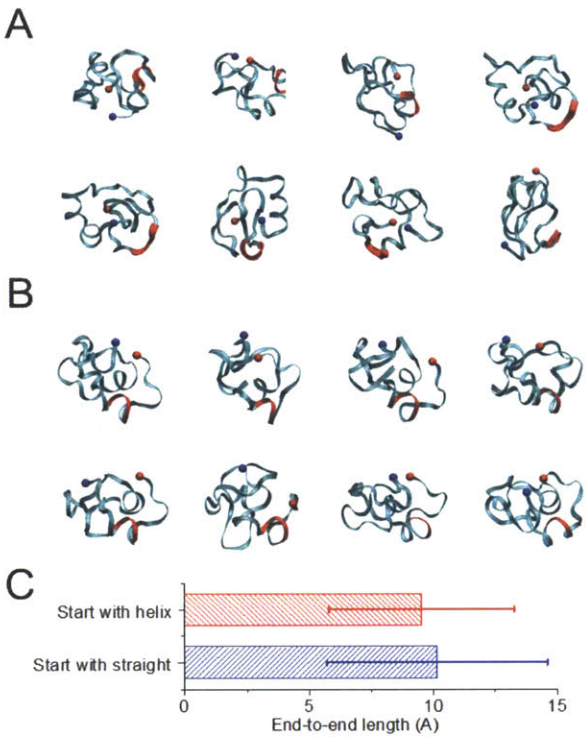


**Fig. 5.4 The conformation of the Δ50 segment, corresponding to the conformations in Fig. 5.3.** With (A) initial straight conformation or (B) initial α-helix conformation final segments appear similar. The region surround tyrosine 646 (AA645-647) is highlighted (red ribbon) and put in the front stage. The starting point (AA607) is a blue ball and end point is (AA656) a red ball. (C) The histogram of the end to end length of this Δ50 segment based on initial conformation is similar in length (error bar indicates standard deviation).

### 5.3.2 Molecular structure of mature lamin A tail and its Δ50 LA mutant

Experimentally, the tail domains of mwt LA and Δ50 LA show a β-sheet structure with random coil but no α-helix. After purification, the proteins are estimated to be ≈4.0 +/- 0.3 nm in size, as measured by our collaborator using dynamic light scattering (DLS) technique. Using the same REMD technique as used above, we predict conformations of the full tail domains of mwt LA and Δ50 LA. As expected for a mostly intrinsically disordered protein, our simulations yield an ensemble of conformations for the tail domains of mwt LA and Δ50 LA. We present the eight conformations that are most frequently visited by the replica with the lowest temperature in the order of decreasing significance (Fig. 5.5A and 5.5B). Initially, the structure of the s-type Ig-fold of the tail domain is modeled from the starting conformation available from the protein database (PDB with ID 1IVT (Krimm et al., 2002)), and the remaining tail domain is given a straight conformation. We observe that the Ig-fold maintains a majority of its β-sheet structure throughout the simulation, while other regions become disordered with a distribution of structures, but no single, dominant, equilibrium state. This intrinsic disorder is expected by the high proline and glycine content (3% proline and 16% glycine for mwt LA tail; 4% proline and 10% glycine for Δ50 LA tail). We compare the simulation result of the secondary structure against experimental measurement result given by CD as summarized in Table 5.2 and Fig. 5.6.

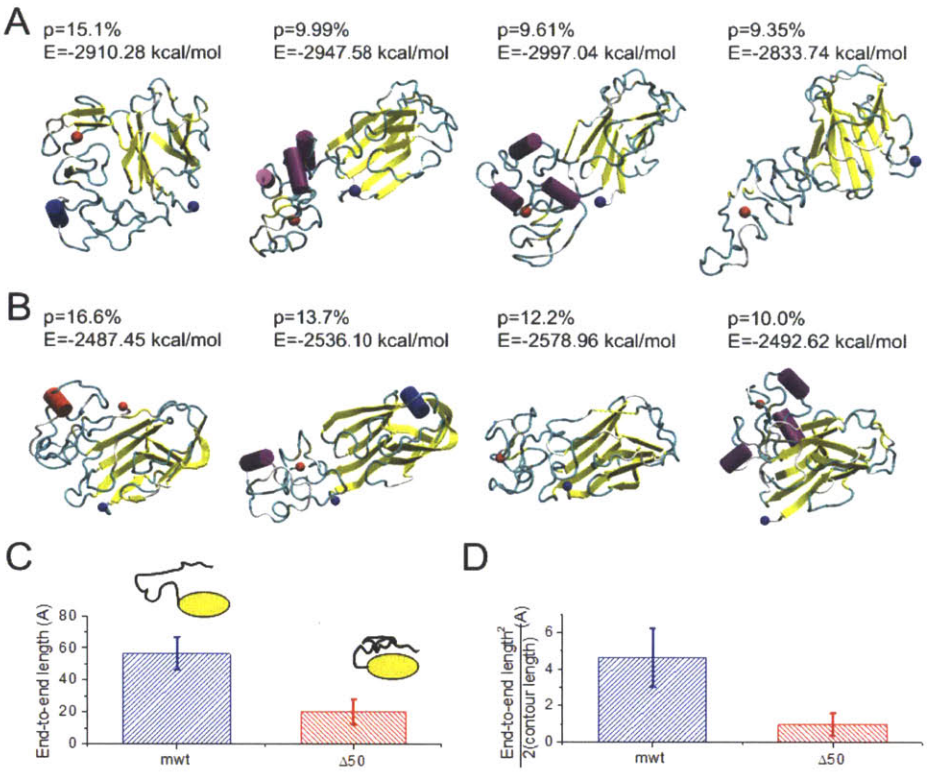


**Fig. 5.5 Conformations and structures of tail domains for normal and disease cases (Qin et al., 2011).** Conformations with high significance factors of the (A) mwt LA tail domain AA428-646 and (B) Δ50 LA tail domain, AA428-614* show different structures. The beginning amino acid is marked with a blue dot and the C-terminus is marked with a red dot. (C) The end-to-end length from the end of the Ig-fold domain (AA545) to the tail end (AA646 for mwt LA and AA614* for Δ50 LA) of all the conformations of the mwt LA and Δ50 LA tail domains, respectively. (D) Normalizing the square of the end-to-end length by the contour length reflects the persistence length of the peptide. We find that the Δ50 LA tail domain is significantly more compact, even when considering the loss of amino acids in the truncation.

We find that the folded structures of Δ50 LA tail (Fig. 5.5B) are more compact than structures of mwt LA tail (Fig. 5.5A). From these simulation results, we quantify the end-to-end length ($r_{ee}$) of this disordered domain (AA545-646 for mwt LA and AA545-614 for Δ50 LA in Fig. 5.5C). The average $r_{ee}$ for mwt LA tail was measured to be $r_{ee} = 56.5 \pm 10.2$ Å, which is much larger than that of the Δ50 LA tail ( $r_{ee} = 20.4 \pm 7.6$ Å). Some of the reduction in the $r_{ee}$ in the Δ50 LA tail, as compared to mwt LA tail counterpart, can be accounted for by the reduced contour length from the net loss of 32 amino acids. However, the contour length is only reduced by 30%, much less than their difference in $r_{ee}$. The persistence length of an isolated polypeptide chain is ≈4 Å, which is much smaller than the loss of contour length (357 Å for 102 AAs of mwt LA versus 245 Å for 70 AAs of Δ50 LA). As such, we can use the Worm-Like-Chain (WLC) model for the disordered regions (in the limit of $l \gg l_p$) (Leuba et al., 1994; Marko and Siggia, 1995)

$$l_p = \frac{<r_{ee}^2>}{2l} \tag{5.2}$$

to estimate the persistence lengths of the mwt LA tail and the Δ50 LA tail. We obtain that the persistence length of the Δ50 LA tail (1.0 ± 0.6 Å) is 78% shorter than that of the mwt LA tail (4.6 ± 1.6 Å), as shown in Fig. 5.5D. This result indicates that the tail domain of Δ50 LA is more able to adopt a greater variety of conformations. We calculate the effective radius of the molecule, and find that the diameter of Δ50 LA tail closely agrees with the experimental hydrodynamic radius from DLS. Interestingly, the deviation of the protein sizes, both by experiment and simulation, are the most striking features (Table 5.1); and the mwt LA has a more heterogeneous distribution of protein sizes.

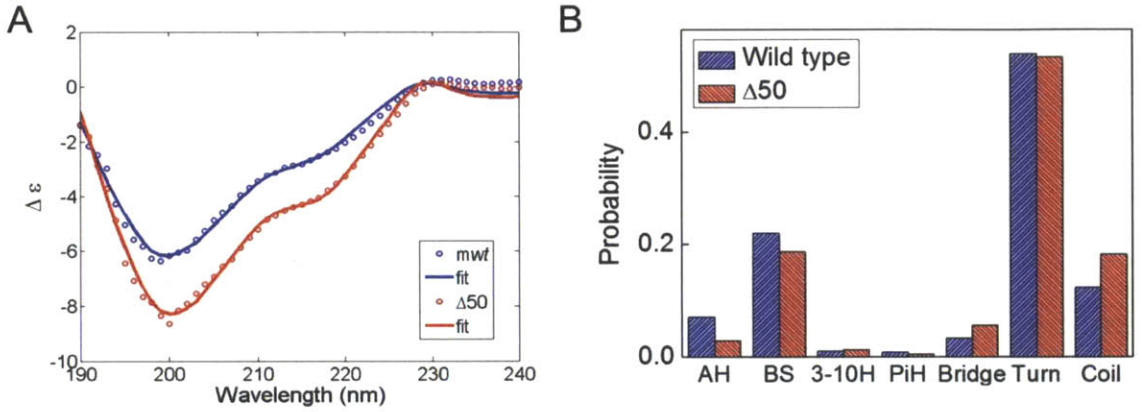


**Fig. 5.6 Secondary structure characteristic of tail domains for normal and disease cases (Qin et al., 2011).** A, experimental result given by CD measurement performed in Dahl's lab through collaboration. B, simulation result given by REMD.

**Table 5.1 Hydrodynamic radius of the tail domain measured by DLS measured by Dahl's lab through collaboration and corresponding simulation results**

| LA tail domain | DLS experiment (nm) | Simulation (nm) |
|---|---|---|
| mwt | 4.5 ± 1.3 nm | 5.0 ± 1.4 nm |
| Δ50 | 4.0 ± 0.3 nm | 3.2 ± 0.3 nm |

We quantitatively measure the overall structural composition of the mwt LA and Δ50 LA for the tail domain as shown in Fig. 5.6 and summarized in Table 5.2, and we observe that >70% of the amino acids feature turn or coil secondary structures, confirming that this domain is mostly disordered. We count the secondary structures of each amino acid and plot the ratio. Some positions in the mwt LA tail are seen to form α-helices including 562 (24 AAs), 584 (8 AAs) and 620 (20 AAs). In the Δ50 LA tail, α-helices are similar if not slightly longer for the mid segment but are missing the third segment (562 (24 AAs) and 582 (12 AAs)). Compared with random coils, a peptide with a helix structure has a much longer persistence length (≈100 Å since the backbone is stabilized by hydrogen bonds), which explains why the mwt LA tail, with net 16 more AAs in helical structure, has a longer persistence length.

**Table 5.2 Secondary structure composition of the lamin tail measured by CD in Dahl's lab through collaboration and corresponding simulation results**

| LA tail domain Secondary structure. | CD experiment (%) β-sheet | Turn+coil | Simulation (%) β-sheet | Turn+coil |
|---|---|---|---|---|
| mwt | 27 ± 5 | 66 ± 5 | 21.9 | 66 |
| Δ50 | 23 ± 7 | 70 ± 7 | 18.6 | 72 |

### 5.3.3 Molecular mechanics of mature lamin A tail and its Δ50 LA mutant under loading

To investigate protein stability in normal and mutated states, we use simulation to measure the mechanical stability of the mwt and Δ50 LA tail domains by unfolding the protein at 27°C and monitoring the conformation of the region containing the Ig-fold. We focus on the Ig-fold because: (a) the Ig-fold is the most ordered and probably most stabilized motif representing the limiting factor of mechanical strength; (b) the Ig-fold interacts with lamin binding proteins and DNA (Stierle et al., 2003; Zastrow et al., 2004); and (c) we can directly compare denaturation with experimental results based on the tryptophan residues in the Ig-fold. We apply the SMD protocol to stretch the two regions flanking the Ig-fold domain (AA428 and 545) within the full tail domain to unfold the structure and record the force-extension curve during the stretching process (Fig. 5.7A).

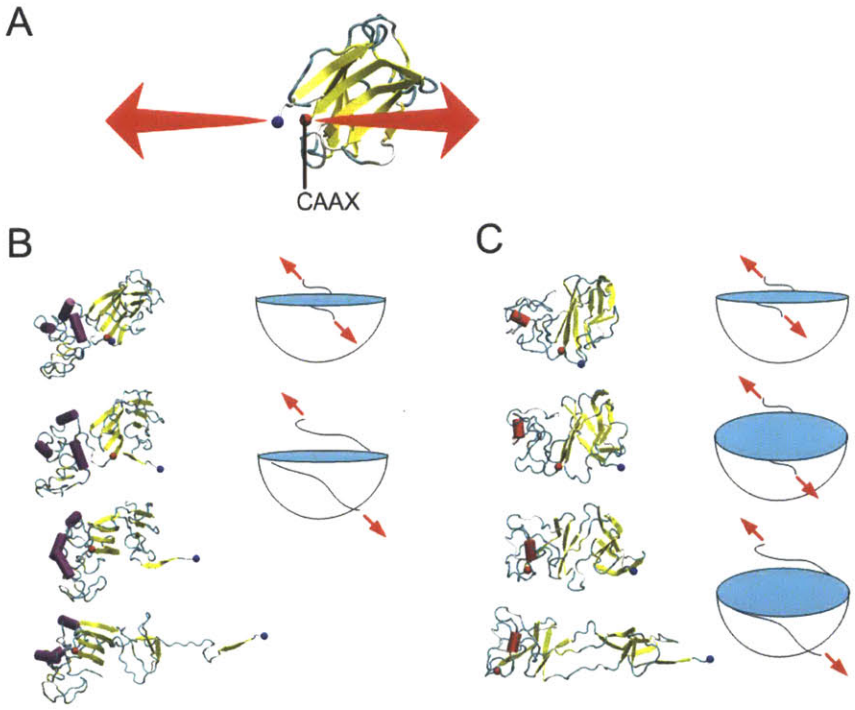


**Fig. 5.7 Results of SMD simulation of Ig-fold domain unfolding (Qin et al., 2011).** A, The β-sheet structure of the Ig-fold domain and boundary conditions used to apply the mechanical load. While the force was applied to the Ig-fold, the other amino acids were in their pseudo-equilibrium states. B, Snapshots of a mwt LA tail domain during the unfolding process, taken at extensions of 0, 15 Å, 38 Å and 75 Å, respectively show one β-strand at a time (yellow)

unfolding from a central structure. C, Snapshots of a Δ50 LA tail domain during the unfolding process, taken at extensions of 0, 15 Å, 38 Å and 75 Å, respectively. The images show an intermediate state with no "outlying" β-strands. The cartoons in panels B and C schematically describe the different deformation process of the mwt and Δ50 LA tail domains, respectively. Note the large blue binding pocket in panel C is larger for Δ50 LA tail domain, than that for mwt LA tail domain and present for larger deformations (and representing the intermediate state).

We find that the unfolding processes of the two protein segments reveal different deformation mechanisms under loading. The unfolding of the Ig-fold in the mwt LA tail shows a stepwise unwinding of the β-strands from the one end to the other end (Fig. 5.7B). However, the unfolding of the Ig-fold of the Δ50 LA tail domain reveals a two-state process. In the first state, the Ig-fold maintained secondary β-sheet structure but shows a tertiary transition, similar as opening two halves of a sandwich along an edge. This unfolding pattern opens up a β-sheet pocket. In the second stage, β-strands are peeled away from the central structure in a similar fashion as mwt LA tail (Fig. 5.7C). The two-state unfolding process of the Ig-fold domain appears to be unique to the Δ50 LA tail, which could qualitatively describe by a pocket-unwinding model as illustrated in Fig. 5.7C. This result shows that the Ig-fold of the Δ50 LA tail transforms before unfolding under loading. These results suggest altered interactions within the Ig-fold and that the mutation makes unfolding more variable. Thus, the two-state unfolding complicates a normally continuous process and may allow for more stable intermediate states.

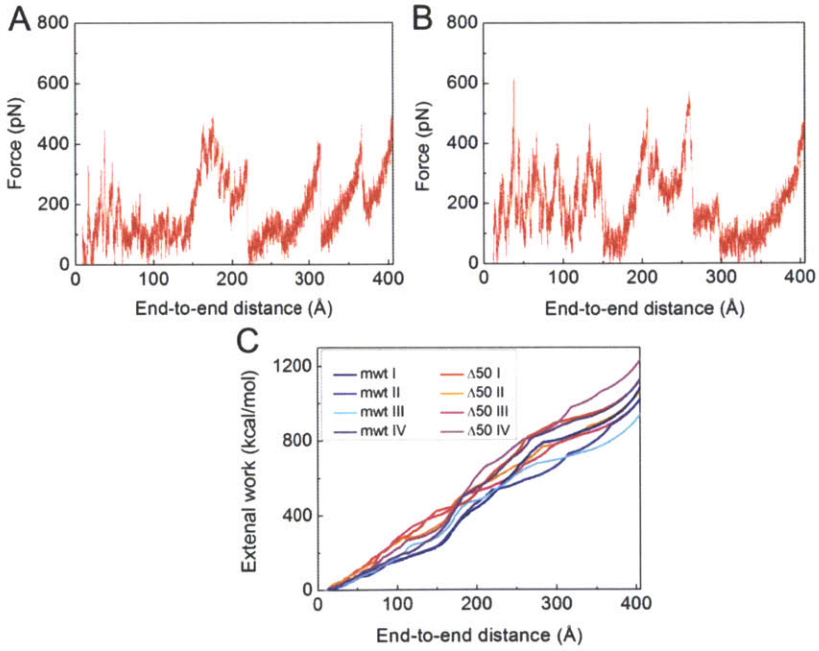


**Fig. 5.8 Force-extension curves of the unfolding of Ig-fold domains (Qin et al., 2011).** A, A force-extension curve as recorded during the unfolding process of the mwt LA Ig-fold as shown in Fig. 5.7B. B, A force-extension curve as recorded during the unfolding process of the Δ50 Ig-fold as shown in Fig. 5.7C. C, The external work on the Ig-fold domain during the unfolding process as a function of the end-to-end distance, which is computed by integrating of

the force-extension curves obtained by unfolding each of the structures shown in Fig. 5.5.

We repeat the loading process for other possible structures with highest significance factor (structures in Fig. 5.5) and collect all force-extension curves as shown in Figs. 5.8A and B from the initial conformation until the end-to-end distance equaled the contour length (≈403 Å). We can see the force-extension curves act as worm-like-chain (WLC) models stretching at the end once the structure gets totally unfolded. Initially, there were 4-5 transition peaks, each corresponding to an unfolding event of a β-strand, requiring the unfolding force of 357.8 ± 94.2 pN. After each unfolding event, the force drops and shifts rightward because the contour length has increased. We integrate the force-extension curves (Fig. 5.8C) and find that the external work to fully unfold the Δ50 LA Ig-fold was 1113.8 ± 75.1 kcal/mol and 1057.3 ± 70.2 kcal/mol for the mwt LA Ig-fold. To fully unfold the Ig-fold of the Δ50 LA tail domain, 56.5 kcal/mol more work is required than in the case of the mwt LA tail domain. We believe that this extra energy comes from the fact that the Δ50 LA tail is more compact, which stabilizes the Ig-fold and results in an increase of the unfolding energy. From Fig. 5.8C, the energy difference at 75 Å extension, corresponding to the first-stage transition shown in Fig. 5.7C, is 65 kcal/mol, suggesting that the additional energy to fully unfold the Ig-fold may primarily be required for the first-state, hinge-like transition.

## 5.4 Validation of disease mechanism in experiments

To experimentally measure the stability of the LA tails and validate the computational results our collaborators, Kalinowski and Dahl, utilize the presence of four hydrophobic tryptophan residues in the Ig-fold (Fig. 5.2) as a way to monitor protein thermal unfolding (Eftink, 1994). Here, to make the work clear, we include the detail of their experiments in the first part of this section and then we use their data for quantitative comparison against our simulation results. They monitor the intensity of protein solutions at 342 nm, the peak wavelength of the emission spectra, as a function of temperature. The intensity is then normalized assuming a fully folded state at low temperature 37°C and a fully unfolded state at high temperature 95°C. The resulting unfolding curve as a function of temperature is shown in Fig. 5.9A. Measuring the thermal stability gives us insight into the tail domains' thermal equilibrium. Using this analysis, they find that the mwt LA tail shows little sample-to-sample variation and we determine a transitional melting temperature ($T_{M,mwt}$) of 63.2 ± 0.09 °C at which 50% of the protein is unfolded. The Δ50 LA tail domain shows an increased sample-to-sample variation and shows a $T_{M,\Delta 50}$ of 65.8 ± 0.23°C (Fig. 5.9B, Table 5.3).

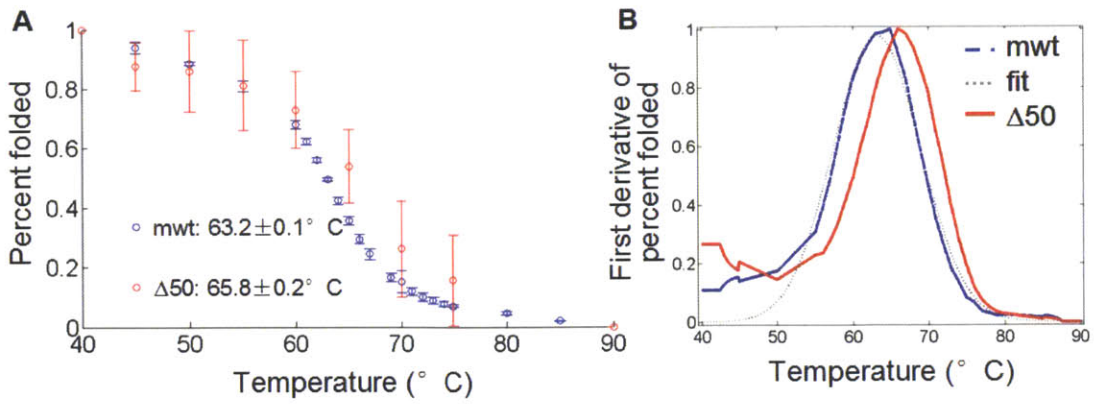


**Fig. 5.9 Thermal denaturation of Δ50 LA and mwt LA protein by measuring tryptophan fluorescence performed in Dahl's lab (Qin et al., 2011).** A, Fluorescence of maximum tryptophan signal are normalized to signals corresponding to 100% folded (measured at 37°C) and 0% folded (at 95°C). The averages of two independent runs are shown of each protein. B, To find the transition melting temperature, we take the first derivative of the signal. Interpolation, smoothing and fit to a Gaussian curve allow us to determine transition temperatures with confidence intervals.

**Table 5.3 Experimentally measured $T_M$ of lamin A tails from thermal denaturation and tryptophan fluorescence performed in Dahl's lab (Qin et al., 2011).**

| LA tail domain | $T_m$ (°C) | $r^2$ | σ (°C) | $T_m$ (°C) | $\sigma_{Tm}$ (°C) |
|---|---|---|---|---|---|
| mwt | 63.13, 63.24 | 0.96, 0.94 | 0.070, 0.055 | 63.2 | 0.09 |
| Δ50 | 65.80, 65.82 | 0.32, 0.88 | 0.215, 0.085 | 65.8 | 0.23 |

Our collaborators further confirm the melting temperature of the Δ50 LA tail by examining changes in the secondary structure using CD with increasing temperature as well as by differential scanning calorimetry (DSC). They perform these analyses on Δ50 LA tail domain since the protein is less susceptible to aggregation and the baseline protein state was more regular. The change in CD signal at 230 nm with increasing temperature normalized to room temperature and denatured points shows a characteristic denaturation when fit to a van't Hoff model

$$\ln(K_{eq}) = -\frac{\Delta H}{RT} + \frac{\Delta S}{R} \tag{5.3}$$

where the $K_{eq}$ = (fraction unfolded)/(fraction folded). From this fit they observed a characteristic $T_M$ of 63°C based on secondary structure. They confirm this transition temperature using DSC, and observed a $T_M$ of 63°C. These values are slightly below the $T_M$

proposed earlier by using thermal denaturation, the similar range of temperatures for denaturation of secondary and tertiary structure suggests robustness of the thermal stability measures. However, changes in secondary structure are limited by low signal to noise ratio (small amounts of β-sheet compared to random coil).

Using those experimental measurement results, we now qualitatively compare our *in vitro* result with the *in silico* results and find that the Δ50 LA tail is more stable in both experiment and simulation. According to the Bell-Evans model (Bell, 1978; Evans and Ritchie, 1997; Rief et al., 1998), the unfolding probability of a structure stabilized by molecular bonds is proportional to exp $(-E_b/k_BT)$ where $E_b$ is the energy barrier height and $k_BT$ is the thermal energy. Thereby, for Δ50 LA at 50% unfolding in simulation, we have

$$\exp\left(\frac{-(E_{\Delta 50}-w_{M,\Delta 50})}{k_BT_0}\right) = \exp\left(\frac{-E_{\Delta 50}}{k_BT_{M,\Delta 50}}\right) \tag{5.4}$$

Where $\langle w_{M,\Delta 50}\rangle = 551.5 \pm 40.1$ kcal/mol is the averaged external energy applied to unfold 50% of the Δ50 LA as the end-to-end length equals to half of the fully unfolded length (Fig. 5.8C) and $T_0$=300 K (27°C) is the room temperature. Eq. 5.4 means the increasing temperature has a same effect at the intermediate unfolding stage, and from this equation we obtain $E_{\Delta 50}$ = 4815.7 kcal/mol. In experiments:

$$\exp\left(\frac{-E_{\Delta 50}}{T_{M,\Delta 50}}\right) = \exp\left(\frac{-E_{mwt}}{T_{M,mwt}}\right) \tag{5.5}$$

And since both of the two structures are at the intermediate unfolding stage with a same unfolding probability. We have similar conclusion for the simulations as

$$\exp\left(\frac{-(E_{\Delta 50}-w_{M,\Delta 50})}{k_BT_0}\right) = \exp\left(\frac{-(E_{mwt}-w_{M,mwt})}{k_BT_0}\right) \tag{5.6}$$

By solving Eqs. 5.5 and 5.6, we have $\Delta w_{exp} = E_{\Delta 50}(T_{M,\Delta 50} - T_{M,mwt})/T_{M,\Delta 50} = 37.0 \pm 7.0$ kcal/mol (equals to $62 \pm 12\ k_BT$ for $T$=300 K), which corresponds to the extra energy needed to unfold 50% of the Δ50 LA more than the mwt LA. Since $\langle w_{M,mwt}\rangle = 481.7 \pm 46.1$ kcal/mol is obtained by simulation from Fig. 5.8C, we obtain the extra energy term from simulation as $\Delta w_{sim} = \langle w_{M,\Delta 50} - w_{M,mwt}\rangle = 69.8 \pm 17.4$ kcal/mol (equals to $117 \pm 29\ k_BT$ for $T$=300 K), which is in the same order of magnitude as the experimental result.

In summary, experimentally, the thermal transition midpoints are $T_{M,\Delta 50}$ =65.8 ± 0.23°C for the Δ50 LA tail domain and $T_{M,mwt}$ =63.2 ± 0.09 °C for the mwt LA tail domain, indicating that the Δ50 LA tail domain is more difficult to unfold. This experimental result agrees with the *in silico* result that additional energy was required to fully unfold the Δ50 LA tail domain structure. According to a calculation based on the Bell-Evans model (Bell, 1978; Evans and Ritchie, 1997; Rief et al., 1998), we arrive at $\Delta w_{exp} = 37.0 \pm 7.0$ kcal/mol ($62 \pm 12\ k_BT$ for $T$=300 K). This corresponds to the additional energy of $\Delta w_{sim} = 69.8 \pm 17.4$ kcal/mol ($117 \pm 29$ $k_BT$ for $T$=300 K) needed to unfold 50% of the Δ50 LA tail more than the mwt LA tail in our experimental studies. We find that the computational results are on the same order of magnitude as the experimental result. The difference between the experiment and simulation results could be caused by the intrinsic difference of the two methods. In the SMD simulation

approach, the force is applied only at the two ends of the strand with a finite loading rate, the structure unfolded along the prescribed direction and the force required to overcome the energy barriers is applied only in this one prescribed direction. In temperature mediated changes in tryptophan fluorometry, the unfolded form has more degrees of freedom and the rate of temperature increase is also intrinsically different from the loading rate used in our simulation. Also, experiments could possibly include simultaneous kinetic aggregation, which was not included in the simulation.

Using a combination of theoretical and experimental methods, we have studied atomic conformations and nanomechanical stabilities of the tail domain of the mwt LA tail and a mutant associated with HGPS (Δ50 LA tail). Our results demonstrate that the Δ50 LA tail is more compact than the mwt LA tail domain. Most importantly the unfolding of the Δ50 LA tail domain requires a higher energy barrier to overcome unfolding, likely due to transitioning through a pseudo-stable intermediate state. This phenomenon is in agreement with experimental measurements using both tryptophan fluorometry and circular dichroism methods.

These findings highlight the need to keep the protein geometry in mind when trying to understand the molecular mechanisms of the disease. Previously, experimental works of wild type and HGPS cells have shown a stiffening of nuclei from HGPS patients and resistance to mechanical pressure, and alteration in the mechanical properties is due to the presence and overaccumulation of the Δ50 LA protein and associated filaments at the inner nuclear membrane (Dahl et al., 2004; Goldman et al., 2004). The etiology of HGPS has long been thought to be a function of the retained farnesyl group alone (Capell et al., 2008; Leuba et al., 1994), but our results suggest that changes in protein stability may be contributing to the disease pathology. This finding is consistent with recent studies which show that the presence of unfarnesylated prelamin A and Δ50 LA still have cellular and organism effects whose mechanisms are not yet entirely clear (Davies et al., 2010; Verstraeten et al., 2008; Yang et al., 2011).

Furthermore, our experimental and computational results quantitatively and consistently show that the Δ50 LA tail is a more stable structure (by approximately 37-70 kcal/mol or 62-117 $k_BT$), as well as a more compact molecule. This suggests an explanation for the increased compactness of *in vitro* reconstituted filaments of full length Δ50 LA than mwt LA (Taimen et al., 2009). This compact filament structure, likely caused by a smaller and more stable Δ50 LA tail, may also partly be responsible for reduced turnover of proteins from the nucleoskeleton (Dahl et al., 2004; Goldman et al., 2004) and is thus much more than just a farnesyl-related issue. We also observe an increased propensity for Δ50 LA tail domain to form dimers, suggesting an increase in dimer-dimer interaction strength and as a result, a reduced capacity for the Δ50 LA tail domain to be reorganized by thermal fluctuations (moderated temperatures or moderate force), consisted with the extra energy and higher temperature that is required to unfold the Δ50 LA tail domain seen here. Filaments that include the more stable Δ50 LA may more readily aggregate, show reduced turnover, and due to their stronger binding appear mechanically more rigid and therefore "brittle", thereby directly explaining earlier experimental findings (Dahl et al., 2004; Dahl et al., 2006; Delbarre et al., 2006) based on the geometric and mechanistic insight developed in this study. Our results may also explain a

recent experimental report that showed that the proliferation of HGPS cells is significantly impaired (Verstraeten et al., 2008).

From a mechanistic viewpoint we have shown that the mwt LA tail unfolds by individual beta-strands being pulled away from the central structure in a sequential process. In contrast, the Δ50 LA tail domain shows a two-state transition process with a tertiary opening of the Ig-fold into two halves, which we termed a "β-sheet pocket". Within this pocket there may exist other "hidden" binding sites similar to the internal structure of the Ig-folds of titin (Marszalek et al., 1999), or fibronectin (Klotzsch et al., 2009) that may alter the affinity to binding partners. The two stage transition process may also alter the unfolding process of the assembled filament, and we hypothesize that this mechanism could imply that the unfolding of Δ50 LA lamin filament features a greater structural variability, while the process in case of wild-type lamin filament is smoother. This could explain differential binding of Δ50 LA to proteins and DNA. We suggest that there may be other differential protein-protein binding associated with Δ50 LA, but this binding may be energy dependent, such as with force or temperature.

The "structure" of intrinsically disordered proteins are described as an ensemble of conformations which may represent conformations allowing for protein-protein binding to different binding partners and have been shown to be necessary for specific mechanical functions of biological materials including spider silk and talin rods (del Rio et al., 2009; Keten et al., 2010). Here, we have demonstrated the use of an integrated experimental-computational approach to determine a group of structures to gain molecular-level insight into pathological mechanisms. Given lamin A's proposed role in mechanotransduction, and the multiple binding partners of the tail domain, further study of the conformations of the tail domain relating to mechanical function should be explored both in simulation and experiment.

# 6 Calcium affects the physiological process of lamin A tail

Lamin proteins, primarily at the inner nuclear membrane, contribute to nuclear structure and function. The posttranslational processing pathway of lamin A includes farnesylation of the C-terminus, likely to increase membrane association, and subsequent proteolytic cleavage of the C-terminus. HGPS is a premature aging disorder wherein a mutant version of lamin A, Δ50 lamin A, retains its farnesylation. We study here that membrane association of farnesylated Δ50 lamin A tail domains requires calcium. Experimental evidence and molecular dynamics simulations collectively suggest that the farnesyl group is sequestered within a hydrophobic region in the tail domain in the absence of calcium. Membrane binding in the absence of calcium could not be detected. The results suggest that a conformational change induced in Δ50 lamin A with divalent cations plays a regulatory role in the post-translational processing of lamin A, which may be important in disease pathogenesis.

## 6.1 Background on the maturation process of lamin A tail

A-type lamins, including lamin A, contribute to a variety of functions that include DNA transcription, heterochromatin regulation, cell senescence, DNA damage repair, and the sequestration of transcription factors (Dittmer and Misteli, 2011; Simon and Wilson, 2011). These type V IF proteins are also the primary structural elements of the nucleoskeleton (Dahl and Kalinowski, 2011). Lamins structurally relates to other IF proteins (Herrmann et al., 2007), but their C-terminal tail domain (TD) is much larger than that of other IFs and undergoes significant post-translational processing. *LMNA* codes for the precursor prelamin A (preLA), which is transported into the nucleus where the C-terminal CaaX domain (the last 4 amino acids, specifically, Cys-Ser-Ile-Met) is farnesylated and carboxymethylated (Barrowman et al., 2008). The modified preLA is then cleaved by the enteroprotease ZMPSTE-1 at Y646 to produce mature LA. Dysfunctions of this process including loss of ZMPSTE-1 or mutations including the Y646 cleavage site are responsible for devastating human diseases. In the premature aging syndrome Hutchinson Gilford progeria syndrome (HGPS), a point (C1824T) mutation of *LMNA* gene causes the activation of a cryptic splice site and a loss of exon 11 in the TD (Eriksson et al., 2003). The loss of the 50 amino acid segment contains the ZMPSTE-1 cleavage region. This lost causes retention of the farnesylation which in turn results in changes in thermodynamic stability of the mutant protein, Δ50 LA or progerin (Qin et al., 2011). At a much lower frequency than in HGPS, activation of the cryptic splice site that produces Δ50 LA occurs sporadically in normal cells, and this defect accumulates with aging (Scaffidi and Misteli, 2006).

The biochemistry of LA TD processing has been determined, but the biological benefits of the complex processing pathway and the regulation of its individual steps are so are unclear (Davies et al., 2011). Although farnesyl transferases have been found in both the endoplasmic

reticulum and the nucleus, farnesylation of the protein likely occurs in the nucleus (Barrowman et al., 2008). The farnesyl modification is suggested to increase the association of preLA with the inner nuclear membrane (Hennekes and Nigg, 1994; Lutz et al., 1992). Similarly, the pathologies associated with the expression of Δ50 LA in HGPS result, in part, from the farnesylation causing overaccumulation of structural proteins at the inner nuclear membrane (Dahl et al., 2006; Goldman et al., 2004). Indeed, mislocalization of LA and LA-associated proteins at the inner nuclear membrane results in altered DNA repair, transcription and signaling (Reddy and Comai, 2012), as well as changes in protein-protein interactions (Kubben et al., 2012). On the other hand, a single farnesylation is insufficient to confer permanent membrane association of proteins in other systems (Nadolski and Linder, 2007; Philips, 2012; Silvius and l'Heureux, 1994). Therefore, it is unclear if the presence of the farnesyl is sufficient for the cellular pathological phenotype or if additional factors, including altered protein-protein interactions (Kubben et al., 2012) or altered protein packing are involved (Qin et al., 2011; Taimen et al., 2009).

## 6.2 Molecular modeling of ion effect on lamin A tail structure

Structure refinements in explicit solvent and ionic environment are carried out by the REMD method in explicit solvent environment in the NAMD 2.7b2 package (Nelson et al., 1996; Sugita and Okamoto, 1999). The reason we do not use implicit solvent as we have done in the last chapter is that there are difficulties to model ion in implicit solvent. For example, EEF1 does not have ion models or proper description of their dynamics, Poisson-Boltzmann method is numerically too expensive for MD simulation and the Generalized Born method does not distinguish the ion type. The TIP3P explicit atomistic water model implemented in simulations requires much more computing time than other implicit solvent models. However, it has been found to be most reliable to accurately reproduce experimental structural properties and ions are properly described in this solvent condition.

### 6.2.1 Replica exchange method in explicit solvent with ions

Using the explicit solvent model, we can quantitatively address the ion effect in simulations. The interacting force and energy among particles is defined by the CHARMM27 all-atom energy function for protein and solvent models. The simulation time step is 2 fs with rigid bonds model for all the covalent bonds between hydrogen atoms and other heavy atoms. We use particle mesh ewald (PME) function with a grid width <1 Å to calculate the electronic interaction because and it is an efficient method to accurately include all the long-distance electrostatics interactions. The initial structure of the lamin A tail is obtained by using the sequence of *Homo sapiens* laminA/C (SwissProt/TrEMBL accession number P02545) for the prelamin A and the protein folding result performed by of REMD calculation in implicit solvent model (given in Chapter 5). The initial structure is solvated in the solvent box with water and different ionic conditions (NaCl, $CaCl_2$). The net charge of the system is zero and each ion is initially distributed randomly in water that at least 5 Å from the protein structure. Classic MD simulations are performed on these systems in the NPT ensemble with the shrinkable volume (NPT, constant pressure of 1 atmosphere, constant temperature of 310 K) for 10 ns in the purpose of getting an equilibrated solvent condition. The parameters of the

simulation set up are summarized as following. We perform the REMD simulation by using canonical ensemble (NVT) for each replica which has been more widely applied in studying protein foldings than the grand canonical ensemble because the fluctuating system volume affects the energy calculation and the pressure has little effect on the proteins' secondary structure (Paschek et al., 2005). Constant temperature for each replica within the range of $T_{min} = 310$ K and $T_{max} = 600$ K. The minimum temperature is selected for the physiological condition. The maximum temperature is selected basing on that we want to satisfy the condition $\omega_0 \exp\left[-E_b/(k_B T_{max})\right] > 1$, where $E_b \sim 9$ kcal mol$^{-1}$ can be used to estimate the hydrogen-bond energy and $\omega_0 = 10^{13}$ s$^{-1}$ is the natural vibration frequency, to ensure that there can be conformation change that involves hydrogen-bond breaking during simulations. Temperatures for replicas exponentially increase from the lowest to the highest, as a function of $T_i = T_{min}(T_{max}/T_{min})^{(i-1)/(n-1)}$ where $n$ is the number of replicas for REMD method (Feig et al., 2004). Here $n$ is decided by a using a function (Nadler and Hansmann, 2008)

$$n^{opt} = 1 + 0.594\sqrt{C/k_B}\ln\left(T_{max}/T_{min}\right) \tag{6.1}$$

to find the replica number that can give optimal performance for the REMD simulation, where $C = 9.07 k_B N$ givens the specific heat of the solvent system with $N = 14{,}656$ water molecules. According to this estimation, we use 128 replicas in our simulations. The simulation requires at least 128 CPUs to run in parallel, but 1024 CPUs (8 CPUs for each replica) have been tested for our simulations in Teragrid and there is no efficiency lost. The acceptance ratio, which is defined by the ratio of successful exchange event between two neighboring replicas in temperature, is 37%±14%, which is a high value that means our simulation set up can give efficient structural prediction. As the simulation starts, each REMD cycle includes an equilibrium interval and an exchange event. The equilibrium time between two exchange events is set to be 2 ps. Each exchange event compares the energy of the configuration within two replicas with closest temperature. The Metropolis criterion is used to judge whether or not the configurations exchange between the higher and lower temperature replicas. For each solvent condition, we run for 3,000 cycles to make sure that there is no future change in energy. We again classify all the conformations of the protein in this structure refinement according to mutual similarity (share similar detail as in section 5.2.3). For each structure cluster, we select the representative conformations with lowest energy.

### 6.2.2 Metadynamics method

We apply well-tempered metadynamics to study the free energy landscape as a function of the dihedral angle of the Ig-fold (Barducci et al., 2008). This technique enhances the sampling in molecular simulations. The metadynamics simulations are performed by NAMD and the PLUMED package (Bonomi et al., 2009; Nelson et al., 1996). This method enhances the sampling speed in simulations by adding bias potentials during simulation and has the advantage of ensuring the convergence of the energy landscape without requiring an initial estimate. We choose the biased collective variable to be the dihedral angle among the center of 4 amino acids (S429, S437, I497, and L478 at the edge of the Ig-fold in lamin A tail). The simulations are run with an initial configuration of the fully equilibrated lamin A tail obtained after REMD simulation. Other parameters include the enhanced temperature of 900 K where

the collective variable is sampled, and Gaussian hills with the width of 5° are added to bias the energy of the collective variable at a rate of 0.01 kcal/mol for every 0.2 ps, corresponding to a deposition rate of 0.05 kcal/mol/ps. Each of the well-tempered metadynamics runs is 1000 ps long and the convergence of the energy landscape is confirmed.

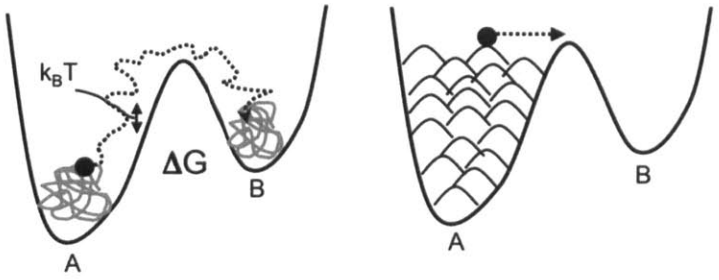


**Fig. 6.1 A schematic of the computing the free energy landscape by using metadynamics method (Barducci et al., 2008).**

### 6.2.3 Modeling of Farnesyl Diphosphate

We need to model the structure and interaction scheme of the farnesyl diphosphate (FPP), which is not defined in the standard CHARMM27 force field. We set up the initial conformation of FPP according to its atomic coordinates as found in protein data bank (with ID 1KZO) (Berman, 2008). The interactions (covalent bond, angle, dihedral, electrostatic and vdW interactions) among the atoms in FPP are defined in the CHARMM General force field 2b6 (Vanommeslaeghe et al., 2010). We update the CHARMM27 force field to incorporate the section of the definition of FPP as is found in CHARMM General force field as has been performed before (Janosi and Gorfe, 2010). We validate our force field by setting up a small molecule of the CaaX decorated by the FPP end and running equilibrium for 2 ns in NPT ensemble in solvent. We compare the equilibrated FPP structure in this simulation to the atomic structure solved by experiments (structures of farnesyl group in protein data bank with IDs of 1KZO, 1KZP, 2H6F, 2H6H) by statistical calculating the end-to-end distance and bending angle of this FPP molecule, and the conformation of our FPP structure agrees to those experimental solutions, as shown in Fig. 6.2. We include the force field of this domain in the Appendix part in the CHARMM format.

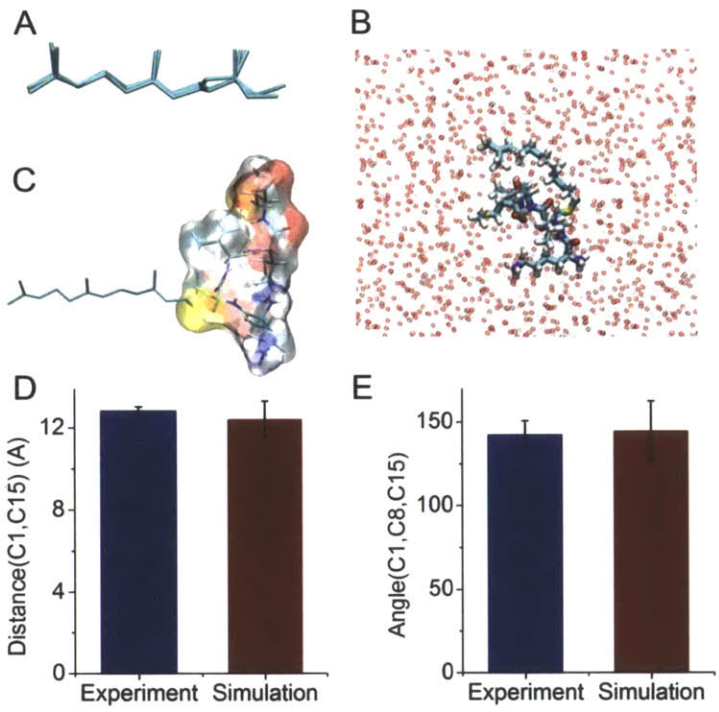


**Fig. 6.2 Modeling and validation of the FPP domain.** A, the initial configuration of the farnesyl group in PDB with IDs of 1KZO, 1KZP, 2H6F, 2H6H. B, equilibration of the farnesyl group and CaaX peptide in solvent for 2 ns. C, snapshot of farnesyl group (left chain) and CxxX peptide (shown by crystal) at equilibrium. D, end-to-end length of the FPP domain comparing to the experimental measurements (in PDB with IDs of 1KZO, 1KZP, 2H6F, 2H6H). E, bending angle of the FPP domain comparing to the experimental measurements.

## 6.3 Calcium alters the lamin A tail structural

To obtain a deeper insight into the structural responses of the lamin A tail to $Ca^{2+}$, we perform MD simulations of the proteins in solvent. To deal with the high degree of intrinsic disorder, we simulate multiple low-energy, pseudo-equilibrated structures with REMD (Sugita and Okamoto, 1999; Swendsen and Wang, 1986). Starting with amino acid chains with extreme initial structures (fully extended form) except for the structured Ig-fold region taken from the protein database (Dhe-Paganon et al., 2002), we allow the protein to relax freely in an implicit solvent environment (check Chapter 5 for detail). To enhance the sampling speed as well as to ensure that structures reach a relevant local energy minima, we investigate numerous independent structures with implicit-solvent REMD to find as many low-energy states as possible. Results are categorized according to their structural similarity, and the four most significant conformations were chosen for further studies of the structural impact of ions (Qin et al., 2011). These four conformations are further refined in REMD simulations with explicit solvent (see 6.2.1) under various ion conditions. We also use metadynamics method to discuss the mechanism of how $Ca^{2+}$ alters the molecular structure of lamin A tail (see 6.2.2).

### 6.3.1 Molecular structure of lamin A tail in different solvent conditions

To quantify the TD's structural response to ion exposure, we focuse on four peripheral amino acids (S429, S439, L478 and I497), which form orthogonal extremes of the two β-sheets that form the Ig-fold (Fig. 6.3A). From the positions of these four amino acids, we determine an orientation angle between the two β-sheets. The Ig-fold is slightly more open ($\theta$ is

systematically larger) in the presence of $Ca^{2+}$ (Fig. 6.3B). We computationally include a farnesyl group to the LA-TDs and pre-equilibrated the farnesyl group within the hydrophobic core of the protein (see 6.2.3). Both Δ50LA-TD and preLA-TD are more open if get farnesylated, and exposure to $Ca^{2+}$ opens the fold further up by a larger angle than with the unfarnesylated proteins (Fig. 6.3C). Since the average distance between I497 and L478 is > 1.7 nm, an increase in the orientation angle $\theta$ indicates that the space between the two β-sheets accommodates more water (with a van der Waals radius of 0.14 nm) in the presence of the ion than in its absence.

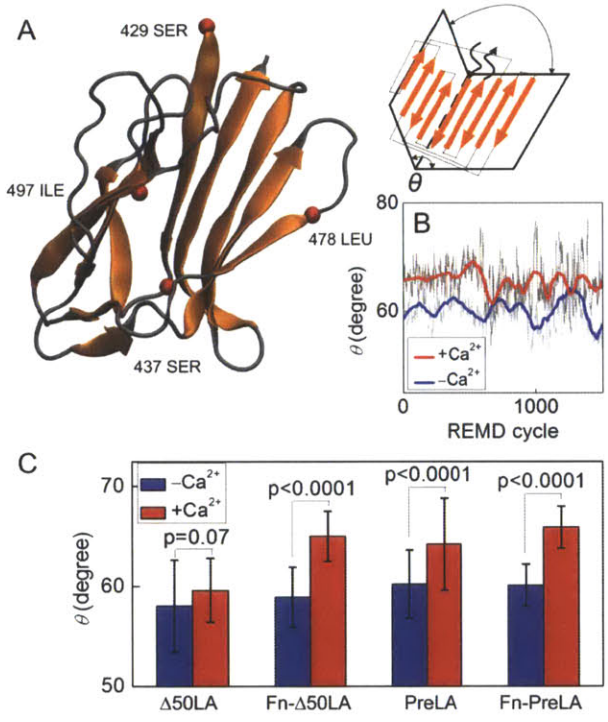


**Fig. 6.3 Altered Ig-fold structures of preLA-TD and Δ50LA-TD exposed to calcium (Kalinowski et al., in revision).** A, We determine the dihedral angle between the two β-sheets of the Ig-fold, $\theta$, from the $C_\alpha$-carbon of 4 periphery amino acids within the full tail. B, We track the fluctuations of the dihedral angle $\theta$ for the preLA-TA conformation in the replica with lowest temperature after each exchange event in equilibrium. The angle is always larger in the presence of $Ca^{2+}$. C, Statistical comparison of the dihedral angle of the Ig-fold for numerous pseudo-equilibrated protein structures for preLA-TD, fn-preLA-TD, Δ50LA-TD and fn-Δ50LA-TD showes increases in $\theta$ with $Ca^{2+}$.

REMD simulations also provide insight into the mechanism by which calcium triggers membrane binding of farnesylated lamin A tail domains. We observe that $Ca^{2+}$ bound spontaneously to the C-terminal CaaX motif, and the interaction persisted through the entire REMD simulation (cyan $Ca^{2+}$ to red CSIM in Fig. 6.4A). Generally, $Ca^{2+}$ binding increases the fluctuation and mobility of the C-terminal region for both Δ50LA-TD (beyond 610'; the prime refers to the new amino acid number for the deletion) and preLA-TD (beyond 660) by 30% and 39%, respectively (Fig. 6.4B).

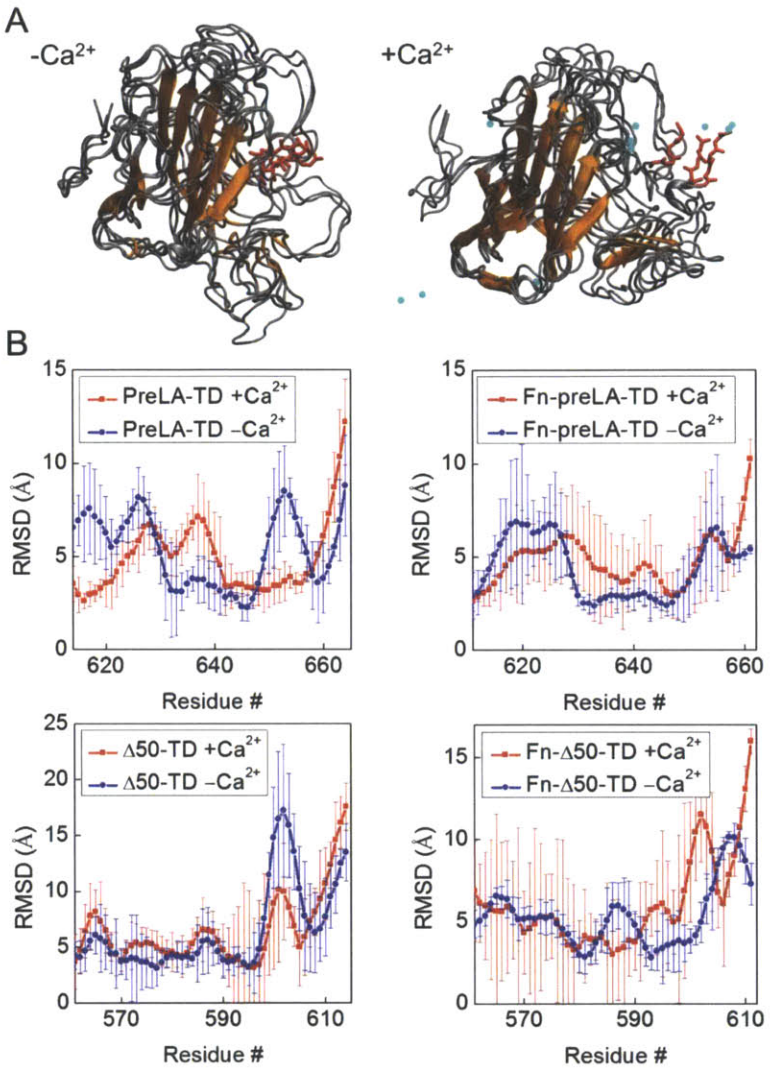


**Fig. 6.4 Dynamics of the C-terminus of preLA-TD and Δ50LA-TD exposed to calcium (Kalinowski et al., in revision).** A, We examine all pseudo-equilibrated conformations of unfarnesylated preLA-TD produced in explicit-solvent REMD simulations and acquire snapshots of the lowest energy conformations (overlaid). In the presence of explicit water and sodium, the C-terminus CSIM (red) is located inside the preLA tail structure. With the addition of $Ca^{2+}$ (cyan), the C-terminus points away from the protein. B, The C-terminal amino acids for each of the four TDs for 10 ns of MD simulation show altered fluctuations or root mean square displacement (REMD) from initial coordinates in the presence of $Ca^{2+}$. For each TD and ionic condition we repeat the simulation for the four lowest energy conformations and statistically compare the results. For the last 3~6 residues, $Ca^{2+}$ causes a substantial increase in amino acid fluctuation. The $Ca^{2+}$-induced fluctuation changes are more substantial for farnesylated proteins, which show reduced C-terminal fluctuations in the absence of $Ca^{2+}$.

C-terminal motility is reduced when the protein gets farnesylated (Fig. 6.4B), and the $Ca^{2+}$ mediated motility increase is enhanced for farnesylated proteins (Fig. 6.4B) by 89% for fn-preLA-TD and 120% for fn-Δ50LA-TD. In the absence of $Ca^{2+}$, the farnesyl (Fig. 6.5, red)

maintains association with the hydrophobic core (Fig. 6.4A, -$Ca^{2+}$). In the presence of $Ca^{2+}$, the farnesyl group "escapes" from the hydrophobic interior of the protein and gets found at the periphery of the pseudo-equilibrated structures (Fig. 6.5A, +$Ca^{2+}$). This is quantified by the increase in solvent available surface area (SASA) of the farnesyl group in the presence of $Ca^{2+}$ (Fig. 6.5B) and increases end-to-end length of the TDs (Fig. 6.5C). We suggest that the farnesyl group associates with the hydrophobic protein core, and the association of $Ca^{2+}$ to the CaaX causes increased probability of farnesyl solvent exposure for membrane association.

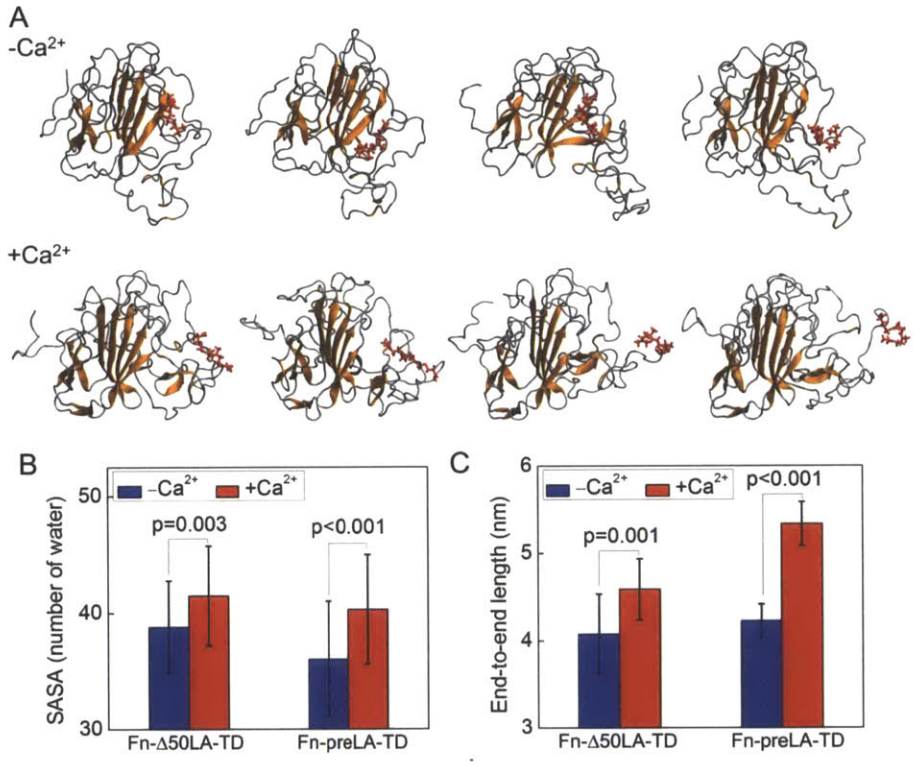


**Fig. 6.5 Simulation of farnesyl dynamics of preLA and Δ50LA TD (Kalinowski et al., in revision).** We pre-equilibrate the farnesyl group within the hydrophobic interior of the respective TDs and allow equilibration in explicit solvent with 50 mM NaCl or 50 mM NaCl + 2 mM $CaCl_2$. A, Comparison of four most significant pseudo-equilibrated structures of fn-preLA-TD. With no $Ca^{2+}$ the farnesyl group (red) is found within the molecule. In the presence of $Ca^{2+}$, the farnesyl group escapes from the TD. B, The solvent accessible surface area (SASA) of the farnesyl group, given by the number of water molecules in contacting with the surface of farnesyl group (threshold distance of 0.38 nm), of fn-Δ50LA-TD and fn-preLA-TD increased in $Ca^{2+}$. C, The end-to-end length of the entire TD of fn-Δ50LA-TD and fn-preLA-TD also increases, suggesting that the $Ca^{2+}$ makes the C-terminus more extended.

In Dahl's *in vitro* experiments, it is found that fn-Δ50LA-TD binds to purified membrane bilayers with a $K_D \sim 2$ μM. This binding coefficient is markedly weaker than most biological binding coefficients. Basing on this, it can be suggested that this weak binding affinity allows protein-membrane association while not causing irreversible association. In the case of lamin A, it is suggested that the farnesyl group weakly associates the protein to the membrane, and

transmembrane lamin binding proteins then more permanently connect lamin A to the inner nuclear membrane. This weak binding is similar to qualitative observations that farnesyl groups are insufficient to stably associate proteins with membranes (Nadolski and Linder, 2007; Philips, 2012; Silvius and l'Heureux, 1994). During normal processing, lamin TDs, and other CaaX-domain proteins, are farnesylated, the aaX residues are cleaved, and the terminus is methylated.(Young et al., 2005b) The proteolysis and methylation steps may play an additional role in stabilizing membrane association by increasing hydrophobicity. However, there have been conflicting reports regarding the additional stability conferred by methylation (Hancock et al., 1991; Leung et al., 2007; Parish et al., 1996).

The association of the fn-Δ50LA-TD is dependent on $Ca^{2+}$. There have been previous studies examining qualitative membrane association of fn-preLA (Polychronidou et al., 2010), but we note that the solvent used contained the divalent cation magnesium. Similarly, recoverin has a $Ca^{2+}$ induced conformational switch to expose the myristoyl group, which is responsible for membrane association (Xu et al., 2011). Unlike recoverin, lamin A tail domains are mostly disordered, so the conformational switch is much less obvious. We demonstrated in the next section through experiments and simulations to discuss the mechanism of how Δ50LA-TD and pre-LA TD undergo a conformational change induced by $Ca^{2+}$ that "opens" the Ig-fold and increases the exposure and mobility of the farnesylated C-terminus.

### 6.3.2 Molecular mechanism of conformational changes in the lamin A tail induced by calcium

By using the well-tempered metadynamics method (Barducci et al., 2008), we are able to obtain the free energy landscape of this Ig-fold structure as a function of the dihedral angle (among the peripheral amino acids S429, S439, L478 and I497). We start by solvating the lamin A tail in the solvent of 50 mM NaCl without calcium. From this free energy landscape we obtain the dihedral angle of minimum free energy and this result corresponds to the equilibrated dihedral angle of the Ig-fold. We repeat such measurement for the Ig-fold of lamin A tail in the constant $Na^+$ number while altering $Ca^{2+}$ concentration that ranges from 0 to 240 mM, as illustrated in Fig. 6.6A. Each simulation system keeps electrionic neutral as we control the $Cl^-$ number accordingly. To reach a more accurate estimation of the calcium concentration, we count the number of calcium ions within 12 Å as the minimum distance to the lamin tail surface during the simulation. It is found that the increasing calcium number around the lamin tail increases the dihedral angle of the Ig-fold as shown in Fig. 6.6B, while the angle reaches its asymptotic value for high calcium concentration as shown in Fig. 6.6C.

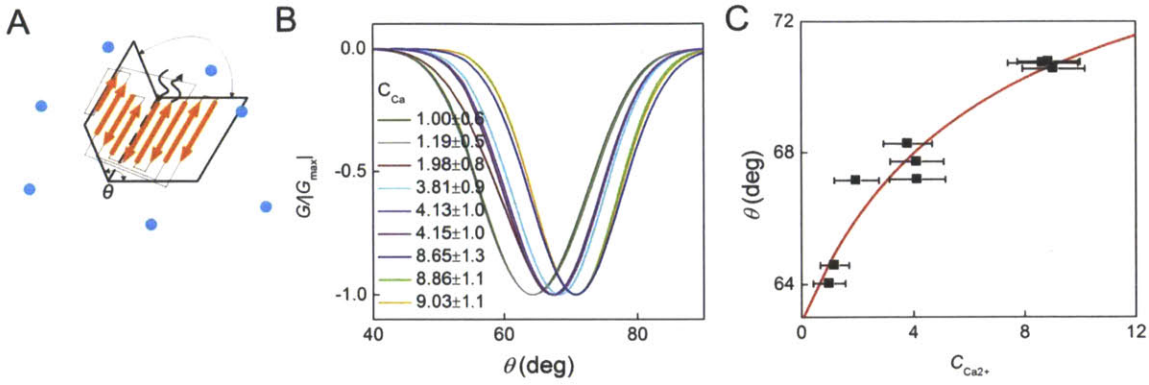


**Fig. 6.6 The molecular mechanism of conformational changes in the lamin A tail induced by $Ca^{2+}$.** A, Schematic of calcium ions around the lamin A tail. B, the multiple free energy landscapes of the dihedral angle of the Ig-fold, each is given by different calcium concentration, as measured during well-tempered metadynamics simulations. C, the summary of the dihedral angle of minimum free energy as a function of the calcium concentration, and Hill function is used to fit the simulation result as given by the solid curve.

We use Hill model to analysis the dependence of the dihedral angle on the calcium concentration. This model has the equation as

$$\frac{d\theta}{\theta_0} = \frac{[\mathrm{Ca}^{2+}]^{\mathrm{n}}}{K_d + [\mathrm{Ca}^{2+}]^{\mathrm{n}}} \tag{6.2}$$

Where $K_d$ is the binding affinity of calcium to protein and $n$ is the stoichiometry of binding. We take $n$=1 because the calcium ion is much smaller than lamin A tail in size and each ions binding to the tail surface is nearly completely independent. Based on the series of metadynamics simulation result, we obtain the binding affinity as $K_d$=6.53, which means 6~7 calcium ions close to the lamin A tail induce the structure transition at the Ig-fold.

To make it easier for comparison, we relate this simulation result to the physiological condition applied in the experiments. Considering that in experiment the protein (lamin A tail) concentration is 5 uM, the necessary calcium concentration for structural transition thereby yields $I_{\mathrm{Ca}^{2+}} = I_{LA}K_d = 32.7$ μM. This relative low value explains why the lamin tail structure is so sensitive to the small amount of calcium add to the solvent. The local concentration of calcium near the protein yields $I_{\mathrm{Ca}^{2+}\_\mathrm{local}} = K_d/\mathrm{N_A}/\mathrm{V} = 900.7$ μM.

## 6.4 Validation of calcium effect in experiments

We extensively compare our simulation results against those of the experimental measurements performed by Kalinowski in Dahl's lab and Lösche's lab by tryptophan fluorescent. In this section, the experimental detail will be first introduced and then we explicitly give how we carry out those comparisons. The tryptophan amino acid residue has inherent fluorescent properties that have long-been used as probes to reflect protein conformation (Vivian and Callis, 2001). LA-TD has four tryptophan residues all of which are

located on or near the Ig-fold (highlighted in bold below). The peak emission intensity is at 342 nm, after excitation at 298 nm to minimize excitation of other aromatic residues. A peak emission at 342 nm indicates that the tryptophan residues are neither in a completely hydrophobic environment, nor are they fully solvent exposed (Chen and Barkley, 1998; Vivian and Callis, 2001). When calcium is titrated into the solution with LA-TD, the protein undergoes a conformational change with a substantial loss in intensity, called quenching, and a slight 2 nm blue shift. The resultant quenching of tryptophan emission indicates a change in the molecular environment that could be due to an increase in solvent exposure, but not an overall change in the polarity of the environment.

The experiments were performed with 5 μM purified unmodified protein dialyzed into 50-700 mM NaCl (Slide-A-Lyzer Dialysis Cassettes, Pierce). 300 μL samples were excited at 295 nm in a 1 cm pathlength polished cell in a Fluorolog-3 (Jobin Yvon-spex, Instruments) and the fluorescence emission spectra were recorded from 310 nm-400 nm. The peak emission intensity at 342 nm (with the background intensity from the buffer subtracted) was used for analysis and normalized by the peak intensity without $Ca^{2+}$ for each sample. The binding affinity and stoichiometry of $Ca^{2+}$ association with the LA TD was determined by fitting the change in fluorescence intensity at 342 nm as a function of $Ca^{2+}$ concentration to a Hill model. For this system where the ligand is the $Ca^{2+}$ and the conformational change is assumed to be proportional to the change in fluorescence intensity at the emission peak, $\Delta I$ (342 nm), normalized by the peak emission at 342 nm without Ca2+ in the solution, $I_0$, the Hill equation is $I/I_0 = [Ca^{2+}]^n/(KD+[Ca^{2+}]^n)$ gives a binding affinity of the protein to calcium $K_D$, as well as the stoichiometry of binding, $n$.

To investigate the mechanism by which $Ca^{2+}$ induces membrane association, we considered $Ca^{2+}$-induced conformational changes of the TD. The TD is intrinsically disordered except for the s-type Ig-fold (Dhe-Paganon et al., 2002; Krimm et al., 2002), therefore, direct structural examination via traditional methods (e.g., crystallography) are not possible. Conformational changes of Δ50LA-TD and preLA-TD were followed by monitoring the fluorescence of their four Trp residues located within and near the Ig-fold (W467, W498, W514, W520; see full sequence in Fig. 5.2). The chemical environment of Trp, including its solvent accessibility, affects the emission quantum yield, and exposure to the solvent has been shown to quench Trp fluorescence (Chen and Barkley, 1998; Vivian and Callis, 2001). Previously, we investigated thermal denaturation of LA-TD and Δ50LA-TD tertiary structure by monitoring Trp fluorescence, confirming that protein denaturation reduces Trp fluorescence (Qin et al., 2011).

The observed fluorescence emission band between 310 and 400 nm was broad, presumably because multiple Trp residues in different microenvironments contribute to the band shape. We observed that the emission decreased with CaCl2 concentration (Figs. 6.7A and B) and saturated for $[CaCl_2] \approx 1$ mM at ~ 30% of the original intensity. Fitting to a two-parameter Hill model indicated a Ca2+ affinity of 261 ± 49 μM for Δ50LA-TD and 286 ± 27 μM for pre-LA TD, both with 1:1 stoichiometries (± 10%) (Fig. 6.7C). These results suggest that Trp residues of the two TDs become more exposed to buffer upon Ca2+ binding. High concentrations of NaCl (> 200 mM) also reduced Trp emission, but Ca2+-induced effects occur at 6 orders of magnitude lower salt concentration (100 μM), independent of

NaCl.

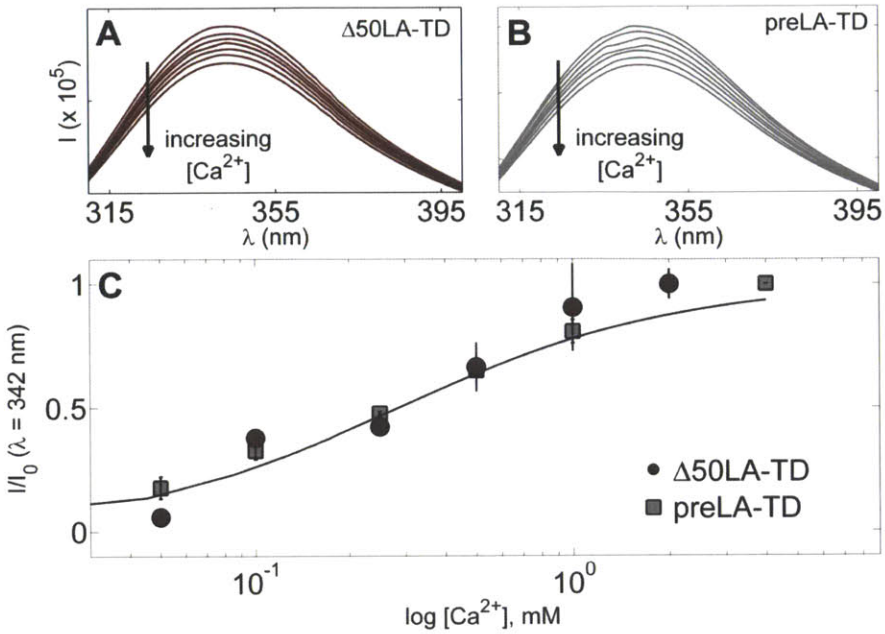


**Fig. 6.7 Calcium caused a conformational change to Δ50LA-TD and preLA-TD (Kalinowski et al., in revision).** The emission spectra of tryptophan residues for purified (A) Δ50LA-TD in 50 mM NaCl and (B) preLA-TD in 500 mM NaCl excited at 295 nm were measured for increasing $Ca^{2+}$ concentration. For $Ca^{2+}$ concentration above 1 mM, there was no change in intensity, indicating no more substantial conformational change induced by $Ca^{2+}$. (C) From plots of emission intensity at 342 nm versus $Ca^{2+}$ concentration, we determined $Ca^{2+}$ dissociation constant ($K_D$~ 250 -300 μM) and binding stoichiometry (1:1). The $I/I_0$ (342 nm) is averaged for 2-3 samples and in NaCl concentrations 50-700 mM NaCl for a given $CaCl_2$ concentration. The $Ca^{2+}$ dissociation constant did not change with the NaCl concentration of the solution.

Based on those experimental measurements, we carry out validation for our simulation results. We set up two models: 1. to relate the atomistic measurement of calcium concentration ($I_{Ca^{2+}}$ and $I_{Ca^{2+}\_local}$ as obtained in the last section) to average calcium concentration as used in experimental and 2. to relate the dihedral angle with the quenching rate as experimentally measured. By doing so, we obtain qualitative understanding of how simulation results comparing to experimental observations.

We assume the calcium concentration distributes according to exponential function as

$$C(x) = \left(I_{Ca^{2+}\_local} - I_{Ca^{2+}}\right) \exp\left(-\frac{x}{x_0}\right) + I_{Ca^{2+}} \tag{6.3}$$

Where $x_0 = 693$ Å is the average distance of protein with concentration of 5 μM. The average concentration is thereby estimated via

$$\bar{C} = \int_{x=0}^{x_0} C(x)\, 4\pi x^2 dx/[4\pi x_0^3/3] = 3(I_{\mathrm{Ca^{2+}\_local}} - I_{Ca^{2+}})[2 - 5\exp(-1)] + I_{Ca^{2+}} \qquad (6.4)$$

Where $I_{\mathrm{Ca^{2+}}} = I_{LA}[\mathrm{Ca^{2+}}]$, and $I_{\mathrm{Ca^{2+}\_local}} = [\mathrm{Ca^{2+}}]/\mathrm{N_A}/\mathrm{V}$, where $[\mathrm{Ca^{2+}}]$ is the total number of calcium ions within 12 Å as the minimum distance to the lamin tail surface. We also derive the quenching rate as a function of the dihedral angle of the Ig-fold as

$$I/I_0 = \frac{K_s V_{wat}\rho}{1+K_s V_{wat}\rho} \qquad (6.5)$$

Where $K_s = 11.6\ \mathrm{mol}^{-1}$ is the average quenching rate for the tryptophan (Badley, 1975), $V_{wat} = L_1 L_2 L_3 \sin(\theta)$ is the volume of water within the Ig-fold and $\rho = 55.4\ \mathrm{mol/L}$ is the density of the liquid water. Basing on the two above equations, we convert the result as shown in Fig. 6.6C into the $\bar{C} - I/I_0$ relation as given in by the experiment. The result is as summarized in Fig. 6.8. The concentration of calcium for structural transition (measured by quenching rate) yields $K_{d\_simulation} = 300\ \mu\mathrm{M}$ in simulation. This result agrees to the experimental measurement as $K_{d\_experiment} = 250 - 300\ \mu\mathrm{M}$, giving the evidence that our simulation catches the physics mechanism of this calcium-induced structural transition process.

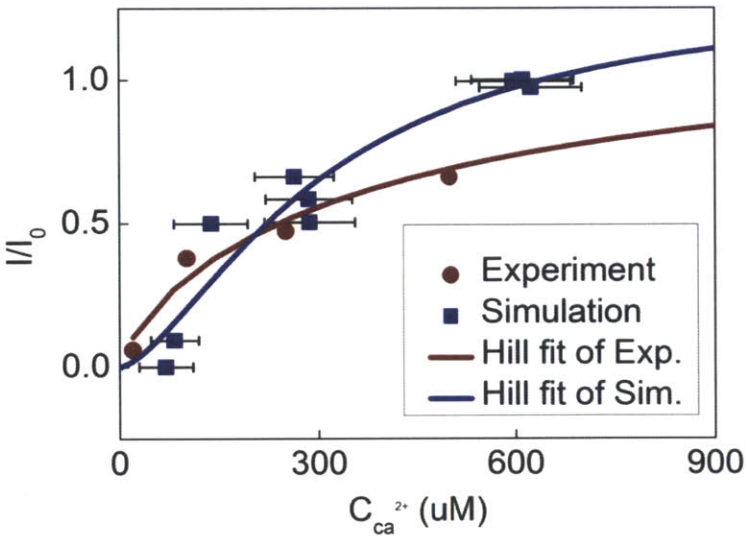


**Fig. 6.8 Comparison between simulation result and experimental result of the quenching rate of the Ig-fold as a function of the concentration of calcium in solution (Kalinowski et al., in revision).**

## 6.5 Conclusions in understanding of lamin A maturation

In experiments it is found that fn-Δ50LA-TD binds to purified membrane bilayers with a $K_D \sim 2\ \mu\mathrm{M}$. This binding coefficient is markedly weaker than most biological binding coefficients. This weak binding affinity may allow protein-membrane association while not causing irreversible association. For lamin A, the farnesyl group weakly associates the protein to the membrane, and transmembrane lamin binding proteins then more permanently connect lamin A to the inner nuclear membrane. This weak binding is similar to qualitative observations that farnesyl groups are insufficient to stably associate proteins with membranes

(Nadolski and Linder, 2007; Philips, 2012; Silvius and l'Heureux, 1994). During normal processing, lamin TDs, and other CaaX-domain proteins, are farnesylated, the aaX residues are cleaved, and the terminus is methylated (Young et al., 2005a). The proteolysis and methylation steps may play an additional role in stabilizing membrane association by increasing hydrophobicity. There have been previous studies examining qualitative membrane association of fn-preLA (Polychronidou et al., 2010), but we note that the solvent condition used contained the divalent cation magnesium. Similarly, recoverin has a $Ca^{2+}$ induced conformational switch to expose the myristoyl group, which is responsible for membrane association (Xu et al., 2011). Unlike recoverin, lamin A tail domains are mostly disordered, so the conformational switch is much less obvious. We demonstrated through simulations and experiments that Δ50LA-TD and pre-LA TD undergo a conformational change induced by $Ca^{2+}$ that "opens" the Ig-fold and increases the exposure and mobility of the farnesylated C-terminus, as illustrated in Fig. 6.9.

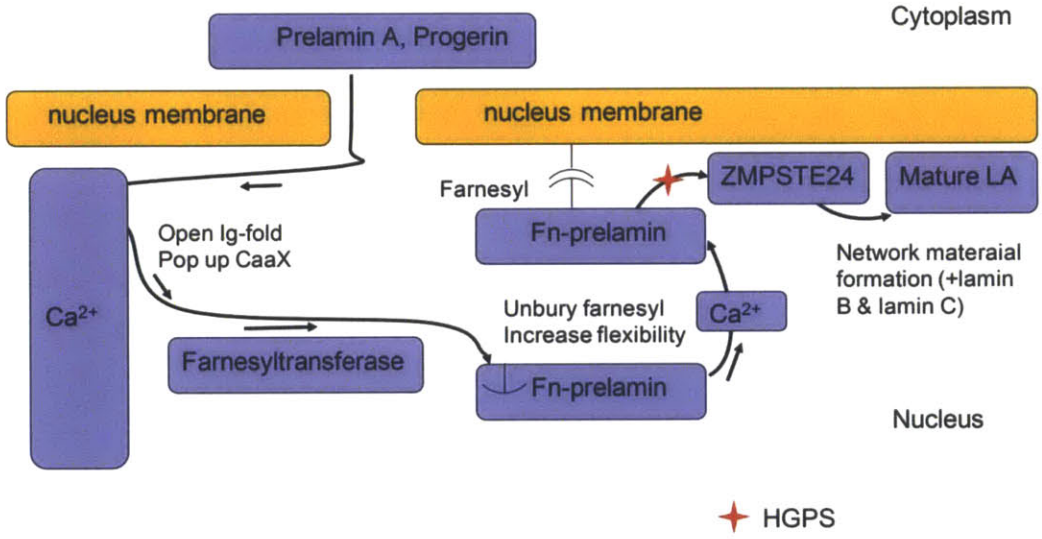


**Fig. 6.9 The schematic of the maturation process of lamin A.** Calcium play an important role in altering the protein conformation and responsible for membrane association (Kalinowski et al., in revision).

The $Ca^{2+}$-induced conformational change may also regulate protein-membrane interactions, protein-DNA or protein-protein interactions. The large size, intrinsic disorder, and Ig-fold binding pocket of the tail domain may all allow for promiscuous binding and may be at least partially responsible for the ability of lamin A tail to bind different partners (Simon and Wilson, 2011). Here, we have shown $Ca^{2+}$ induced conformational changes, and protein binding to the lamin A of one of the many lamin A associated proteins may also induce conformational changes in the tail domain. We find that ions, similar to $Ca^{2+}$, $Mg^{2+}$ can facilitate the IF assembly and contribute to the interfilament crosslinking (Lin et al., 2010b), play important role in governing the membrane association of lamin A. Its *in vivo* application to cells and tissues is the subject of future work.

# 7 Summary and discussion

The objective of this research is to develop an in-depth nanomechanical understanding on the hierarchical structural and mechanical property of IFs, as well as how those characteristics relate to IFs' physiological functions. This research consists of a number of computational simulations and experimental validations. MD simulations have been extensively used to understand how IF folds into a specific structure by given sequence and environment, as well as how to relate IF structures to their mechanical properties, thermal stabilities and binding affinities. We have developed the multiple-scale model in describing the IF network behavior at larger scale with computational efficiency as well as remaining the secondary structure information from the atomistic model. We have compared the results obtained from simulations against experimental results from literature as well as our collaborators. Through this research, we understand the basic nanoscopic structure and mechanical property, as well as some physiological functions of IFs under extreme conditions. Many agreements have been found between the simulations and experiments, showing the capabilities of *in silico* modeling. In addition, our study provides mechanistic insight into a biological material complex as IFs and quantitatively characterizes its material properties in the scope of materiomics.

## 7.1 Summary of main results

IFs, in addition to microtubules and microfilaments, are one of the three major components of the cytoskeleton in eukaryotic cells, playing a vital role in mechanotransduction and in providing mechanical stability to cells. Here we utilize a novel multiple-scale study of the structural and mechanical property, as well as the disease mechanism of IFs. Our research is based on a bottom-up approach that starts with atomistic simulations which provide most fundamental understanding of IF's mechanical behavior.

By identifying the links between structures and deformation mechanisms at distinct hierarchical levels, we show that the multi-scale structure of IFs is crucial for their characteristic mechanical properties, in particular their ability to undergo severe deformation of ≈300% strain without breaking. We observe a transition from α-helices to β-sheets with subsequent interdimer sliding, which has been inferred previously from experiments. We have extensively discussed the mechanism of this structural transition, *i.e.*, how intact α-helices unfold and rearrange into form of β-sheets, and found this process is size dependent.

By upscaling our results, we report for the first time, a quantitative comparison to experimental results of IF mechanics, showing good agreements. According to the structure and mechanical response of IFs obtained from atomistic simulations, we build a mesoscopic IF network model following the finer-trains-coarser principle. We use this model to study the mechanical behavior of nuclear lamina and uncover the physical basis of the material design of nuclear lamina that enables it to withstand extreme mechanical deformation of >100% strain despite the presence of structural defects. We demonstrate that this is due to nanoscale

mechanisms including protein unfolding, alpha-to-beta transition, and sliding, resulting in a characteristic nonlinear force-extension curve. At the larger microscale this leads to an extreme delocalization of mechanical energy dissipation, preventing catastrophic crack propagation. Yet, when catastrophic failure occurs under extreme loading, individual protein filaments are sacrificed rather than the entire meshwork. This mechanism is theoretically explained by a characteristic change of the tangent stress-strain hardening exponent under increasing strain. We theoretically investigate the role of cross-link in nuclear lamina and find that weak crosslink leads to a more flaw tolerant network that is 23% stronger than the one with strong crosslink. This finding suggests that the mechanical properties of interfacial components are critical for materials' mechanical properties.

It has been revealed that the IF tail plays an important role in network assembling but its mechanism is not clear. We focus on this issue by investigating the molecular mechanism of Hutchinson–Gilford progeria syndrome. We combine REMD simulations and computational techniques to compare the geometry and thermodynamic stability of the mature lamin A tail against its mutant. Our results demonstrate that the Δ50 LA tail is more compact than the mwt LA tail domain. Most importantly the unfolding of the Δ50 LA tail domain requires a higher energy barrier to overcome unfolding, likely due to transitioning through a pseudo-stable intermediate state. The altered structure and stability of the tail domain provide a molecular mechanism of the disease. We study the membrane association of lamin A tail domains by focusing on the role of calcium. We find calcium binds to the tail domain with an affinity $K_d = 250{\sim}300\ \mu M$ where it alters the structure of the Ig-fold and increases the solvent accessibility of the C-terminus. Our result shows that calcium plays an effective regulatory role in the post-translational processing of lamin A by changing the conformation of lamin A tail. The finding provides a pull pathway of lamin maturation as well as the disease pathogenesis of this specific IF.

## 7.2 Conclusions and impacts: *in silico* study of protein materials

By studying the mechanical and biological properties of IFs from a bottom-up perspective, we have shown the power of computational modeling as a tool to fill in the gap between genotype and phenotype of IFs by setting up bridges of the molecular structure, mechanism and the materials functions. Establishing such links is critical to reach a better understanding of the complete gene expression and modification path, which is not limited to IFs but may be generally applicable to other proteins structures in studying their mechanical properties. With the multi-scale modeling scheme and computational tools, we may rationally design novel polymer materials with greater reliability and tunable material properties by adjusting their compositions and microscopic structures.

The strength of this methodology is that it makes it possible to simulate a system with tens of micrometers dimension while retaining information about molecular details and mechanisms. As single point mutations in protein materials represent typical sources that create flaws in biological systems, it is very important to understand the pathway of the disease because the designs of effective treatments of genetic diseases. Over 4000 known human diseases are estimated to be caused by single gene defects that can be either inherent

or accumulated. Since experimental methods are limited both in time and space resolution, computational modeling has an advantage to investigate biological systems in a bottom-up fashion. In the multiple-scale modeling, quantum effects, thermal fluctuations, chemical reactions, structure stabilities, conformities and interaction networks can all be considered for quantitative understanding of material functions and processes, which are features rooted in the nanoscale realm and extended to the macro realm. By combining with the experimental and clinical effort, we hope that this methodology could facilitate breakthroughs in biomedical and biomaterial innovation in future applications.

### 7.2.1 The advantage in multiple-scale modeling of hierarchical materials

We study the hierarchical structure of IFs and investigate their material behaviors at multiple scales. Our analysis illustrates the opportunities associated with a computational approach in describing complex biological materials. The study reported here provides a new way forward in carrying out molecular-level studies of IF structure-property relationships. This may be particularly important to probe the effects of the variability of the structure and associated changes in chemical and intermolecular interactions. Defects can be introduced at different hierarchical levels of the structure of IFs, and the effects on the biomechanical performance can provide important insight into physiological and diseased states of IFs. This specifically includes the possibility of probing the effect of mutations using *in silico* materiomics methods, enabling pathogenesis studies of severe medical conditions associated with IF. The model sets the stage for studies ranging from point mutation events to investigating the effects of cross-link strength on IF mechanics. Due to the emerging significance of IFs in a variety of cellular process, the results of our study also contribute to improved understanding of cell deformation, cell adhesion and mechanotransduction. IFs could also be considered a model system that may enable us to fabricate *de novo* engineered materials that display a high sensitivity to applied forces, show resilient mechanical properties, and provide biological compatibility.

### 7.2.2 Coupling of structure and mechanics in protein materials

We study the nonlinear mechanical response of vimentin dimer and tetramer under stretching and systematically probe the mechanism inside this process. Our results provide a critical geometrical condition of the secondary structure transition and associated molecular-level effects. The concept put forth in our simple model may be used to explain other structural transitions, stability, and flexibility in proteins or polymers, and as such, may find future applications in bottom-up materials design. The insight into the critical length scales may have applications in the design of novel peptide-based materials with high stiffness, novel hierarchical fibers, and materials with high extreme absorption capacity.

### 7.2.3 The flaw tolerance of IF networks

Using a mesoscopic model we identified the physical basis of the material design of nuclear lamina that enables it to withstand extreme mechanical deformation of more than 100% strain, despite the presence of structural defects. Our study shows that its superior robustness is caused by mechanisms that act at multiple scales. This is facilitated by a combination of softening-stiffening-softening of filament mechanics, which is generated by protein unfolding,

an alpha-to-beta transition, and intermolecular sliding under mechanical loading. This particular S-shape stress-strain law facilitates an extremely delocalized deformation before yielding and a highly localized failure at failure strains. The delocalized deformation vastly increases the energy absorbing capacity, while the localized failure during crack extension provides an important mechanism to ensure localized damage. This mechanism ensures that few protein filaments are sacrificed rather than the entire meshwork. As an important barrier to protect genetic material crucial to life, the nuclear lamina indeed is a reliable structure that can tolerate extreme mechanical conditions. The general mechanism to create such flaw-tolerant behavior revealed here may also apply to other natural and synthetic materials, and could enable us to fabricate novel bio-inspired materials with flaw tolerance. This opens the possibility that by designing the molecular structure of the material the particular material robustness can be achieved.

### 7.2.4 The fundamental understanding of genetic disease

Using a combination of theoretical and experimental methods, we have studied atomic conformations and nanomechanical stabilities of the tail domain of the mwt LA tail and a mutant associated with HGPS (at Δ50 LA tail). Our computational and experimental results quantitatively and consistently show that the Δ50 LA tail is a more stable structure (by approximately 37–70 kcal/mol or 62–117 kBT), as well as a more compact molecule. This suggests an explanation for the increased compactness of in vitro reconstituted filaments of full length Δ50 LA than mwt LA (Taimen et al., 2009). This compact filament structure, likely caused by a smaller and more stable Δ50 LA tail, may also partly be responsible for reduced turnover of proteins from the nucleoskeleton (Dahl et al., 2004; Goldman et al., 2004). Filaments that include the more stable Δ50 LA may more readily aggregate, show reduced turnover, and due to their stronger binding appear mechanically more rigid and therefore "brittle", thereby directly explaining earlier experimental findings (Dahl et al., 2004; Dahl et al., 2006; Delbarre et al., 2006) based on the geometric and mechanistic insight developed in this study.

Using REMD method, we are able to describe the "structure" of intrinsically disordered proteins by an ensemble of conformations. Those may represent conformations allowing for protein–protein binding to different binding partners and have been shown to be necessary for specific mechanical functions of biological materials including spider silk and talin rods (del Rio et al., 2009; Keten et al., 2010). Given lamin A's proposed role in mechanotransduction, and the multiple binding partners of the tail domain, further study of the conformations of the tail domain relating to mechanical function and pathological mechanisms of diseases can be explored by using the integrated experimental-computational approach.

### 7.2.5 The tunable lamin A tail function

We investigate the maturation process of lamin A tail by focusing on the calcium effect on its conformation. Our results suggest a potential lifetime of prelamin A is produced in the ribosome. After transcription the C-terminal CaaX domain is "hidden" inside the tail of prelamin A. The prelamin A is transported into the nucleus without premature binding. In the nucleus, the higher levels of charge from DNA and counter ions induce a conformational change that exposes the CaaX for farnesylation and other modifications leading to insertion

into the inner nuclear membrane. Our results show that these farnesyl groups may incorporate into the Ig-fold until they are exposed to high $Ca^{2+}$ levels. This mechanism demonstrates that calcium plays an important role as a switch to tune the binding interaction between prelamin A tail and cell's nuclear membrane. This collaborative work between simulation group and experiment group demonstrates the scientific advantage of molecular simulation in studying the mechanical and biochemical function of intrinsically disordered proteins that cannot be crystallized and are laborious for structural analyze.

## 7.3 Future work: bio-inspired material design

In this thesis we focus on IFs and present many mechanical aspects of this biological material. Different mechanisms are presented in describing the mechanical behavior of this specific kind of material, such as secondary structural transition from α-helix to β-sheet in coiled-coils, flaw tolerance of IF nuclear lamina, crosslink rupture versus filament rupture for IF network fracture, stabilization effect versus destabilization effect caused by mutation on lamin A tail, mechanical conformation and function of lamin A tail tuned by ionic conditions. We use tools with clear physical background and basic physical concepts to observe and explain them. Here we discuss those findings in the concept of a broad materials science. We expect that with future efforts, those principles can be applied in material design and have broader applications.

### 7.3.1 Design and fabrication of protein hydrogel

The investigation of IF network in this thesis demonstrates that by using the multiple-scale computational method we are able to reveal its biochemical and mechanical properties in a bottom-up fashion. This provides a foundation for *in silico* design of the protein based hydrogel as well as the procedure for material fabrication. The investigation procedure, mainly as illustrated in Figs. 1.3 and 5.1, provides a rational way to quantitatively understand the material behavior of hydrogel. Starting from MD simulations implemented by DFT calculations for molecules with unknown chemical function, the mechanics of those protein molecules and their interacting strengths can be precisely measured. The mesoscopic model is ready to be trained for each molecule (or a group of molecules) according to the atomistic simulation. Simulations based on this mesoscopic model will be used to study the material assembly and mechanical characterization under various force conditions. Using this research scheme, the mechanical property of many protein hydrogel can be predicted. Protein sequence adjustment and optimization will help to find material with better performance. Experimental validation of simulation results will base on structural analyses, thermal denaturation and rheology tests correspondingly.

### 7.3.2 Bio-mineralized composite materials

Bio-mineralized materials, such as bone and nacre, have shown many mechanical advantages in the aspects of high strength, robustness and energy absorbance. Fabrication of artificial composite materials with similar mechanical function of those biological materials will largely improve the current manufacturing and yield more reliable products. For example, to combine the silk-like soft polymer phase with ceramic-like hard material and fabricate the

body of cars and aircrafts. Interactions at interfaces among different material phases are critical to combine different materials and largely determine the material performance under extreme conditions such as fracture and impact loading. By using atomistic model, the interfacial interaction between organic and inorganic phases could be precisely obtained. By carefully designing the chemical function of the polymer phase, different material phases can perfectly integrate together. Moreover, by controlling the ratio and distribution geometry of those materials phases, materials properties, including Young's modulus, yield strength, ultimate strength and fracture toughness would be under fully control.

### 7.3.3 Material design with tunable mechanical function

Each of those conventional engineering materials, *e.g.*, metal, plastic and glass, has been designed for a single mechanical function with a specific set of Young's modulus, yield strength, ultimate strength and fracture toughness. They have been widely used in industrial, construction and manufacturing because of their clear functions and controllable reliability. However, as the development of nanotechnology, more insightful views of materials nanomechanics have been discovered and it is known that a material's mechanical property is not a simple function of its predominant chemical bonds. For example, the mechanical property of hydrogels and porous materials are strongly depends on the environment, including pH, temperature and ionic conditions. The chemical interaction happens between the environment and the microscopic structure of materials by affecting the atomistic bonding. This effect starts at the nanoscopic scale but its effect extends to the macroscopic scale. Utilizing computational modeling, those effects could be captured and principles could be generated accordingly to quantify the ability to alter the material's mechanical property. Materiomics theories follow computational modeling and simulations would play an important role in understanding and designing the function of those materials.

### 7.3.4 Develop knowledge-based rational protein material design

Material design based on proteins requires tremendous care. Its variation in its basic unit makes its sequence have $20^N$ possibilities for a total length of $N$. In addition, it may have hierarchical structure, making its folded structure difficult to obtain purely depends on computational simulations. However, one may design protein materials based on the existing protein structure database. So far there are 86,172 protein structures available in the giant protein data bank, most of those structures are obtained in experiments by X-ray or NMR and represent stable protein structures. Their atomistic coordinates and secondary structures are available but their mechanical functions are not included in any database. We can use MD simulations to investigate the mechanical property of each of those structures, form a large database and take each of them as a building block to form higher order assembly of materials. Using principles of machine learning, how the protein mechanics relates to its sequence may be obtained from this database. Moreover, point mutations or biochemical decoration may be designed on the surface of protein structures. Those mutations do not significantly alter the protein structures but could have huge effect on protein assembly. Both of the structures and interfacial interactions are important in defining the material property. The protein assembly can be studied by properly training coarse-grained models with same stiffness and normal modes while much fewer degree of freedom.

Computation modeling and simulations have been successfully applied in industrial and architecture design. For instance, the finite element method is widely used to simulate the material behavior under external force and design the property and safety of cars and buildings, the computational fluid dynamics is used to simulate the fluid structure and force distribution around the wings and design the geometry of aircrafts. We hope this research could also grow into a standard procedure and be useful for protein material design.

### 7.3.5 New opportunities for manufacturing and scientific fields

Protein materials have many fascinating advantages that cannot be reached by using engineering materials. Successful design and fabrication of those materials will have giant impact to manufacturing and scientific fields. For example, their biocompatibility and robustness make them ideal materials for biomedical applications, such as implant for plastic surgeries, artificial artery, matrix material for neural repair or carriers of imbedded electronics in human body. The first three has already been widely applied by using other artificial materials but the biocompatibility of protein materials could help to decrease the allergic reactions. The forth one has not been widely applied but it is of great potential to help disable person as well as creating a seamless interface between human and computer. In addition, the self-healing characteristic of some biological materials would contribute to increasing the material's lifespan, making the material recover from a state with buckling or small cracks to a normal status in a suitable environment. Moreover, based on their tunable mechanical properties, biological materials may have the potential to be used with the purpose of energy harvest. It absorbs chemical energy in environments and turns it into kinetic energy. Large array of those units would produce enough power to drive many devices such as artificial heart.

### 7.3.6 Impact on other disciplines

Although all the proposed investigations focus on material study, they would hopefully have potential to affect other disciplines. Fabricating of rigid material through biomineralization may improve the technique in producing artificial materials like cement by decreasing the energy consumption and emission of carbon dioxide, reducing pressure on environment. Systematically investigation of protein structures requires more accurate force field and more efficient algorithm of *ab-initio* calculation, which could drive the development of quantum chemistry on protein structures. Insightful knowledge of molecular structure and mechanics would facilitate the development of computational molecular biology, which may provide quantitative understand of the pathogenesis of disease and makes it possible to design drugs or strategies to block the diseases pathway. The method we used to study the material behavior, by learning the collective property from interactions among subunits, may migrate to simulate the collective behavior of other group of individuals, including animal flocks and behavior of human society. Larger scale simulations and data processing require massive storage space and computing power, driving the development of computer hardware such as quantum computer as well as the computing algorithm.

# 8 Outlook

By exploring the history of the first two industrial revolutions, it is seen that they were both triggered by developments of new materials and wide applications of new energies. The development of new materials had largely changed the manufacturing method and increased the production capacity. With the understanding of the fundamental mechanism of materials, computational material design becomes feasible, which may become a driving force of the next industrial revolution in four regards: First, the development of computational and informational technologies provides massive computing power and big data processing capacity, enabling this *in silico* investigation of materials. Second, computational material design would avoid many repeating trails and greatly shorten the time for material development, satisfying people's growing demand for various products. Third, the digitalized computational material design enables fully customized product design to accommodate many specific requirements. Those products have differences not only in appearance, but also in material property. Forth, energy consumption and carbon emission could be significantly reduced by designing more efficient ways to produce the material and the final product rather than conventional methods.

In this thesis basic physical, chemical and biological sciences are combined with an engineering perspective on materials design. The tools of atomistic simulations and multiple-scale modeling enable us to learn the structural and mechanical properties from IFs. The principles learned from this research would add value to providing guidance in producing high performance protein-based materials and composites from economical and sustainable sources.

Microfluidic techniques, as pioneered by Weitz and others (Agresti et al., 2010; Dammann et al., 2012; Kinahan et al., 2011) may provide a feasible way to synthesize the protein-based materials after well design and optimization by computational simulations. Those techniques enable one to make different molecules well mixed and produce new materials. The chemical environments as well as the stress conditions inside the micro-channels are well controlled, ensuring the homogeneity of the material. Large arrays of micro-channels have the capacity for qualitative production. This assembly technique, combining with 3D printers with high resolutions, may be used to produce materials with defined hierarchical structure features.

In addition to the long-term impact in material engineering, biology and medicine, this research would eventually contribute to our in-depth understanding of how protein structure, mechanics and pathogenesis of related disease interact with one another. As has been discussed in Section 7.3.6, this thesis may have impact on other disciplines and the approach used in material research and optimization may transform to apply in social, economic and management science.

# 9 List of abbreviations and mathematical symbols

| Abbreviation | Description |
|---|---|
| IF | intermediate filament |
| MT | microtubule |
| MF | microfilament |
| MD | Molecular Dynamics |
| REMD | Replica Exchange Method |
| SMD | Steered Molecular Dynamics |
| PDB | Protein Data Bank |
| DFT | Density Functional Theory |
| VMD | Visual Molecular Dynamics |
| CHARMM | Chemistry at HARvard Molecular Mechanics |
| NAMD | Not (just) Another Molecular Dynamics program |
| LAMMPS | Large-scale Atomic/Molecular Massively Parallel Simulator |
| GPU | Graphics Processing Unit |
| CPU | Central Processing Unit |
| VDW | van Der Waals |
| LJ (potential) | Lennard-Jones (potential) |
| H-bond | Hydrogen-bond |
| MPICH | High-performance and Portable MPI |
| RMSD | Root Mean Square Deviation |
| RDF | Radial Distribution Function |
| AFM | Atomic force microscopy |
| HGPS | Hutchinson-Gilford progeria syndrome |
| WLC (model) | Worm-Like-Chain (model) |
| PME | Particle mesh Ewald |
| NPT | Isothermal–isobaric ensemble of constant temperature and constant pressure |
| NVT | Canonical ensemble of constant volume and constant temperature |
| CD | Circular dichroism |
| DLS | Dynamic light scattering |
| DSC | Differential scanning calorimetry |

# 10 References


Ackbarow, T., and M.J. Buehler, 2007. Superelasticity, energy dissipation and strain hardening of vimentin coiled-coil intermediate filaments: atomistic and continuum studies. Journal of Materials Science 42: 8771-8787.

Ackbarow, T., and M.J. Buehler, 2009. Molecular Mechanics of Stutter Defects in Vimentin Intermediate Filaments. Experimental Mechanics 49: 79-89.

Ackbarow, T., X. Chen, S. Keten, and M.J. Buehler, 2007. Hierarchies, multiple energy barriers, and robustness govern the fracture mechanics of alpha-helical and beta-sheet protein domains. Proceedings of the National Academy of Sciences of the United States of America 104: 16410-16415.

Ackbarow, T., D. Sen, C. Thaulow, and M.J. Buehler, 2009. Alpha-helical protein networks are self-protective and flaw-tolerant. PLoS ONE 4: e6015.

Aebi, U., J. Cohn, L. Buhle, and L. Gerace, 1986. The Nuclear Lamina Is a Meshwork of Intermediate-Type Filaments. Nature 323: 560-564.

Agresti, J.J., E. Antipov, A.R. Abate, K. Ahn, A.C. Rowat, J.C. Baret, M. Marquez, A.M. Klibanov, A.D. Griffiths, and D.A. Weitz, 2010. Ultrahigh-throughput screening in drop-based microfluidics for directed evolution. Proc Natl Acad Sci U S A 107: 4004-9.

Alberts, B., J.H. Wilson, and T. Hunt, 2008. Molecular biology of the cell. 5th ed. Garland Science, New York.

Apgar, J.R., K.N. Gutwin, and A.E. Keating, 2008. Predicting helix orientation for coiled-coil dimers. Proteins-Structure Function and Bioinformatics 72: 1048-1065.

Aziz, A., J.F. Hess, M.S. Budamagunta, J.C. Voss, A.P. Kuzin, Y.P.J. Huang, R. Xiao, G.T. Montelione, P.G. FitzGerald, and J.F. Hunt, 2012. The Structure of Vimentin Linker 1 and Rod 1B Domains Characterized by Site-directed Spin-labeling Electron Paramagnetic Resonance (SDSL-EPR) and X-ray Crystallography. Journal of Biological Chemistry 287: 28349-28361.

Badley, R.A., 1975. The location of protein in serum lipoproteins: a fluorescence quenching study. Biochim Biophys Acta 379: 517-28.

Bar, H., N. Mucke, A. Kostareva, G. Sjoberg, U. Aebi, and H. Herrmann, 2005. Severe muscle disease-causing desmin mutations interfere with in vitro filament assembly at distinct stages. Proc Natl Acad Sci U S A 102: 15099-104.

Barducci, A., G. Bussi, and M. Parrinello, 2008. Well-tempered metadynamics: A smoothly converging and tunable free-energy method. Physical Review Letters 100: 020603.

Barrowman, J., C. Hamblet, C.M. George, and S. Michaelis, 2008. Analysis of prelamin A biogenesis reveals the nucleus to be a CaaX processing compartment. Mol Biol Cell 19: 5398-408.

Batchelor, G.K., 2000. An introduction to fluid dynamics. 1st Cambridge Mathematical Library ed. Cambridge University Press, Cambridge, U.K. ; New York, NY.

Baumberger, T., C. Caroli, and D. Martina, 2006. Solvent control of crack dynamics in a reversible hydrogel. Nature Materials 5: 552-555.

Beaudouin, J., D. Gerlich, N. Daigle, R. Eils, and J. Ellenberg, 2002. Nuclear envelope breakdown proceeds by microtubule-induced tearing of the lamina. Cell 108: 83-96.

Bell, G.I., 1978. Models for the specific adhesion of cells to cells. Science 200: 618-27.

Berman, H.M., 2008. The Protein Data Bank: a historical perspective. Acta Crystallogr A 64: 88-95.

Berman, H.M., J. Westbrook, Z. Feng, G. Gilliland, T.N. Bhat, H. Weissig, I.N. Shindyalov, and P.E. Bourne, 2000. The Protein Data Bank. Nucleic Acids Research 28: 235-242.

Bertaud, J., Z. Qin, and M.J. Buehler, 2009. Atomistically Informed Mesoscale Model of Alpha-Helical Protein Domains. International Journal for Multiscale Computational Engineering 7: 237-250.

Bertaud, J., Z. Qin, and M.J. Buehler, 2010. Intermediate filament-deficient cells are mechanically softer at large deformation: A multi-scale simulation study. Acta Biomaterialia 6: 2457-2466.

Best, R.B., K.A. Merchant, I.V. Gopich, B. Schuler, A. Bax, and W.A. Eaton, 2007. Effect of flexibility and cis residues in single-molecule FRET studies of polyproline. Proc Natl Acad Sci U S A 104: 18964-9.

Bhattacharya, R., A.M. Gonzalez, P.J. Debiase, H.E. Trejo, R.D. Goldman, F.W. Flitney, and J.C. Jones, 2009. Recruitment of vimentin to the cell surface by beta3 integrin and plectin mediates adhesion strength. J Cell Sci 122: 1390-400.

Bonomi, M., D. Branduardi, G. Bussi, C. Camilloni, D. Provasi, P. Raiteri, D. Donadio, F. Marinelli, F. Pietrucci, R.A. Broglia, and M. Parrinello, 2009. PLUMED: a portable plugin for free-energy calculations with molecular dynamics. Computer Physics Communications 180: 1961-1972.

Brändén, C.-I., and J. Tooze, 1999. Introduction to protein structure. 2nd ed. Garland Pub., New York.

Brenner, M., A.B. Johnson, O. Boespflug-Tanguy, D. Rodriguez, J.E. Goldman, and A. Messing, 2001. Mutations in GFAP, encoding glial fibrillary acidic protein, are associated with Alexander disease. Nature Genetics 27: 117-120.

Brooks, B.R., R.E. Bruccoleri, B.D. Olafson, D.J. States, S. Swaminathan, and M. Karplus, 1983. Charmm - a Program for Macromolecular Energy, Minimization, and Dynamics Calculations. Journal of Computational Chemistry 4: 187-217.

Brown, J.H., C. Cohen, and D.A. Parry, 1996. Heptad breaks in alpha-helical coiled coils: stutters and stammers. Proteins 26: 134-45.

Bruston, F., E. Delbarre, C. Ostlund, H.J. Worman, B. Buendia, and I. Duband-Goulet, 2010. Loss of a DNA binding site within the tail of prelamin A contributes to altered heterochromatin anchorage by progerin. FEBS Lett 584: 2999-3004.

Buehler, M.J., and H.J. Gao, 2006. Dynamical fracture instabilities due to local hyperelasticity at crack tips. Nature 439: 307-310.

Buehler, M.J., and T. Ackbarow, 2008. Nanomechanical strength mechanisms of hierarchical biological materials and tissues. Comput Methods Biomech Biomed Engin 11: 595-607.

Buehler, M.J., and Y.C. Yung, 2009. Deformation and failure of protein materials in physiologically extreme conditions and disease. Nature Materials 8: 175-188.

Buehler, M.J., F.F. Abraham, and H.J. Gao, 2003. Hyperelasticity governs dynamic fracture at a critical length scale. Nature 426: 141-146.

Buehler, M.J., A.C.T. van Duin, and W.A. Goddard, 2006. Multiparadigm modeling of dynamical crack propagation in silicon using a reactive force field. Physical Review Letters 96: 095505.

Buehler, M.J., H. Tang, A.C.T. van Duin, and W.A. Goddard, 2007. Threshold crack speed controls dynamical fracture of silicon single crystals. Physical Review Letters 99: 165502.

Burke, B., and C.L. Stewart, 2002. Life at the edge: the nuclear envelope and human disease. Nat Rev Mol Cell Biol 3: 575-585.

Capell, B.C., M. Olive, M.R. Erdos, K. Cao, D.A. Faddah, U.L. Tavarez, K.N. Conneely, X. Qu, H. San, S.K. Ganesh, X. Chen, H. Avallone, F.D. Kolodgie, R. Virmani, E.G. Nabel, and F.S. Collins, 2008. A farnesyltransferase inhibitor prevents both the onset and late progression of cardiovascular disease in a progeria mouse model. Proceedings of the National Academy of Sciences of the United States of America 105: 15902-7.

Chang, L., and R.D. Goldman, 2004. Intermediate filaments mediate cytoskeletal crosstalk. Nature Reviews Molecular Cell Biology 5: 601-613.

Chang, L., Y. Shav-Tal, T. Trcek, R.H. Singer, and R.D. Goldman, 2006. Assembling an intermediate filament network by dynamic cotranslation. Journal of Cell Biology 172: 747-758.

Chen, Y., and M.D. Barkley, 1998. Toward understanding tryptophan fluorescence in proteins. Biochemistry 37: 9976-82.

Chernyatina, A.A., S. Nicolet, U. Aebi, H. Herrmann, and S.V. Strelkov, 2012. Atomic structure of the vimentin central alpha-helical domain and its implications for intermediate filament assembly. Proceedings of the National Academy of Sciences of the United States of America 109: 13620-13625.

Church, J.S., G.L. Corino, and A.L. Woodhead, 1998. The effects of stretching on wool fibres as monitored by FT-Raman spectroscopy. Journal of Molecular Structure 440: 15-23.

Coffinier, C., H.J. Jung, Z. Li, C. Nobumori, U.J. Yun, E.A. Farber, B.S. Davies, M.M.

Weinstein, S.H. Yang, J. Lammerding, J.N. Farahani, L.A. Bentolila, L.G. Fong, and S.G. Young, 2010. Direct synthesis of lamin A, bypassing prelamin a processing, causes misshapen nuclei in fibroblasts but no detectable pathology in mice. J Biol Chem 285: 20818-26.

Cohen, T.V., L. Hernandez, and C.L. Stewart, 2008. Functions of the nuclear envelope and lamina in development and disease. Biochemical Society Transactions 36: 1329-1334.

Cornell, W.D., P. Cieplak, C.I. Bayly, I.R. Gould, K.M. Merz, D.M. Ferguson, D.C. Spellmeyer, T. Fox, J.W. Caldwell, and P.A. Kollman, 1996. A second generation force field for the simulation of proteins, nucleic acids, and organic molecules (vol 117, pg 5179, 1995). Journal of the American Chemical Society 118: 2309-2309.

Dahl, K.N., and A. Kalinowski, 2011. Nucleoskeleton mechanics at a glance. J Cell Sci 124: 675-8.

Dahl, K.N., S.M. Kahn, K.L. Wilson, and D.E. Discher, 2004. The nuclear envelope lamina network has elasticity and a compressibility limit suggestive of a molecular shock absorber. J Cell Sci 117: 4779-4786.

Dahl, K.N., P. Scaffidi, M.F. Islam, A.G. Yodh, K.L. Wilson, and T. Misteli, 2006. Distinct structural and mechanical properties of the nuclear lamina in Hutchinson-Gilford progeria syndrome. Proceedings of the National Academy of Sciences of the United States of America 103: 10271-10276.

Daidone, I., F. Simona, D. Roccatano, R.A. Broglia, G. Tiana, G. Colombo, and A. Di Nola, 2004. beta-hairpin conformation of fibrillogenic peptides: Structure and alpha-beta transition mechanism revealed by molecular dynamics simulations. Proteins-Structure Function and Bioinformatics 57: 198-204.

Dammann, C., B. Noding, and S. Koster, 2012. Vimentin networks at tunable ion-concentration in microfluidic drops. Biomicrofluidics 6: 022009.

Dauberosguthorpe, P., V.A. Roberts, D.J. Osguthorpe, J. Wolff, M. Genest, and A.T. Hagler, 1988. Structure and Energetics of Ligand-Binding to Proteins - Escherichia-Coli Dihydrofolate Reductase Trimethoprim, a Drug-Receptor System. Proteins-Structure Function and Genetics 4: 31-47.

Davies, B.S., C. Coffinier, S.H. Yang, R.H. Barnes, 2nd, H.J. Jung, S.G. Young, and L.G. Fong, 2011. Investigating the purpose of prelamin A processing. Nucleus 2: 4-9.

Davies, B.S., R.H. Barnes, 2nd, Y. Tu, S. Ren, D.A. Andres, H.P. Spielmann, J. Lammerding, Y. Wang, S.G. Young, and L.G. Fong, 2010. An accumulation of non-farnesylated prelamin A causes cardiomyopathy but not progeria. Hum Mol Genet 19: 2682-94.

De Sandre-Giovannoli, A., R. Bernard, P. Cau, C. Navarro, J. Amiel, I. Boccaccio, S. Lyonnet, C.L. Stewart, A. Munnich, M. Le Merrer, and N. Levy, 2003. Lamin a truncation in Hutchinson-Gilford progeria. Science 300: 2055.

del Rio, A., R. Perez-Jimenez, R.C. Liu, P. Roca-Cusachs, J.M. Fernandez, and M.P. Sheetz,

2009. Stretching Single Talin Rod Molecules Activates Vinculin Binding. Science 323: 638-641.

Delbarre, E., M. Tramier, M. Coppey-Moisan, C. Gaillard, J.C. Courvalin, and B. Buendia, 2006. The truncated prelamin A in Hutchinson-Gilford progeria syndrome alters segregation of A-type and B-type lamin homopolymers. Human Molecular Genetics 15: 1113-22.

Dhe-Paganon, S., E.D. Werner, Y.I. Chi, and S.E. Shoelson, 2002. Structure of the globular tail of nuclear lamin. J Biol Chem 277: 17381-4.

Dietz, H., and M. Rief, 2008. Elastic bond network model for protein unfolding mechanics. Physical Review Letters 100: 098101.

Ding, F., J.M. Borreguero, S.V. Buldyrey, H.E. Stanley, and N.V. Dokholyan, 2003. Mechanism for the alpha-helix to beta-hairpin transition. Proteins-Structure Function and Genetics 53: 220-228.

Dittmer, T.A., and T. Misteli, 2011. The lamin protein family. Genome Biol 12: 222.

Djaczenk.W, H. Starzyk, and Z. Rzucidlo, 1973. X-Ray-Irradiation Induced Changes of Nuclear Membrane of Kirkman-Robbins Tumor-Cells. Experientia 29: 83-84.

Eftink, M.R., 1994. The use of fluorescence methods to monitor unfolding transitions in proteins. Biophys J 66: 482-501.

Eriksson, M., W.T. Brown, L.B. Gordon, M.W. Glynn, J. Singer, L. Scott, M.R. Erdos, C.M. Robbins, T.Y. Moses, P. Berglund, A. Dutra, E. Pak, S. Durkin, A.B. Csoka, M. Boehnke, T.W. Glover, and F.S. Collins, 2003. Recurrent de novo point mutations in lamin A cause Hutchinson-Gilford progeria syndrome. Nature 423: 293-298.

Esue, O., A.A. Carson, Y. Tseng, and D. Wirtz, 2006. A direct interaction between actin and vimentin filaments mediated by the tail domain of vimentin. Journal of Biological Chemistry 281: 30393-30399.

Evans, E., 2001. Probing the relation between force - Lifetime - and chemistry in single molecular bonds. Annual Review of Biophysics and Biomolecular Structure 30: 105-128.

Evans, E., and K. Ritchie, 1997. Dynamic strength of molecular adhesion bonds. Biophysical Journal 72: 1541-1555.

Fabry, B., G.N. Maksym, J.P. Butler, M. Glogauer, D. Navajas, and J.J. Fredberg, 2001. Scaling the microrheology of living cells. Physical Review Letters 87: 148102.

Falvo, M.R., S. Washburn, R. Superfine, M. Finch, F.P. Brooks, V. Chi, and R.M. Taylor, 1997. Manipulation of individual viruses: Friction and mechanical properties. Biophysical Journal 72: 1396-1403.

Feig, M., J. Karanicolas, and C.L. Brooks, 3rd, 2004. MMTSB Tool Set: enhanced sampling and multiscale modeling methods for applications in structural biology. J Mol Graph Model 22: 377-95.

Fogolari, F., P. Zuccato, G. Esposito, and P. Viglino, 1999. Biomolecular electrostatics with

the linearized Poisson-Boltzmann equation. Biophys J 76: 1-16.

Fong, L.G., J.K. Ng, J. Lammerding, T.A. Vickers, M. Meta, N. Cote, B. Gavino, X. Qiao, S.Y. Chang, S.R. Young, S.H. Yang, C.L. Stewart, R.T. Lee, C.F. Bennett, M.O. Bergo, and S.G. Young, 2006. Prelamin A and lamin A appear to be dispensable in the nuclear lamina. Journal of Clinical Investigation 116: 743-52.

Freund, L.B., 1990. Dynamic fracture mechanics CUP, Cambridge.

Frishman, D., and P. Argos, 1995. Knowledge-based protein secondary structure assignment. Proteins-Structure Function and Genetics 23: 566-579.

Fuchs, E., and K. Weber, 1994. Intermediate filaments: structure, dynamics, function, and disease. Annu Rev Biochem 63: 345-82.

Fudge, D., D. Russell, D. Beriault, W. Moore, E.B. Lane, and A.W. Vogl, 2008. The intermediate filament network in cultured human keratinocytes is remarkably extensible and resilient. PLoS ONE 3: e2327.

Fudge, D.S., K.H. Gardner, V.T. Forsyth, C. Riekel, and J.M. Gosline, 2003. The mechanical properties of hydrated intermediate filaments: Insights from hagfish slime threads. Biophysical Journal 85: 2015-2027.

Georgakopoulou, S., D. Moller, N. Sachs, H. Herrmann, and U. Aebi, 2009. Near-UV circular dichroism reveals structural transitions of vimentin subunits during intermediate filament assembly. J Mol Biol 386: 544-53.

Gittes, F., B. Mickey, J. Nettleton, and J. Howard, 1993. Flexural Rigidity of Microtubules and Actin-Filaments Measured from Thermal Fluctuations in Shape. Journal of Cell Biology 120: 923-934.

Goldberg, M.W., I. Huttenlauch, C.J. Hutchison, and R. Stick, 2008a. Filaments made from A- and B-type lamins differ in structure and organization. Journal of Cell Science 121: 215-225.

Goldberg, M.W., J. Fiserova, I. Huttenlauch, and R. Stick, 2008b. A new model for nuclear lamina organization. Biochemical Society Transactions 36: 1339-1343.

Goldie, K.N., T. Wedig, A.K. Mitra, U. Aebi, H. Herrmann, and A. Hoenger, 2007. Dissecting the 3-D structure of vimentin intermediate filaments by cryo-electron tomography. Journal of Structural Biology 158: 378-385.

Goldman, R.D., D.K. Shumaker, M.R. Erdos, M. Eriksson, A.E. Goldman, L.B. Gordon, Y. Gruenbaum, S. Khuon, M. Mendez, R. Varga, and F.S. Collins, 2004. Accumulation of mutant lamin A causes progressive changes in nuclear architecture in Hutchinson-Gilford progeria syndrome. Proceedings of the National Academy of Sciences of the United States of America 101: 8963-8.

Gross, M., 2000. Proteins that Convert from alpha Helix to beta Sheet: Implications for Folding and Disease. Current Protein & Peptide Science 1: 339-347.

Guthold, M., W. Liu, B. Stephens, S.T. Lord, R.R. Hantgan, D.A. Erie, R.M. Taylor, and R. Superfine, 2004. Visualization and mechanical manipulations of individual fibrin fibers suggest that fiber cross section has fractal dimension 1.3. Biophysical Journal 87: 4226-4236.

Guttinger, S., E. Laurell, and U. Kutay, 2009. Orchestrating nuclear envelope disassembly and reassembly during mitosis. Nat Rev Mol Cell Biol 10: 178-191.

Guzman, C., S. Jeney, L. Kreplak, S. Kasas, A.J. Kulik, U. Aebi, and L. Forro, 2006. Exploring the mechanical properties of single vimentin intermediate filaments by atomic force microscopy. Journal of Molecular Biology 360: 623-630.

Hancock, J.F., K. Cadwallader, H. Paterson, and C.J. Marshall, 1991. A CAAX or a CAAL motif and a second signal are sufficient for plasma membrane targeting of ras proteins. EMBO J 10: 4033-9.

Hearle, J.W.S., 2000. A critical review of the structural mechanics of wool and hair fibres. International Journal of Biological Macromolecules 27: 123-138.

Hegele, R.A., 2003. Lamin mutations come of age. Nat Med 9: 644-5.

Hegele, R.A., 2007. Phenomics, lamin A/C, and metabolic disease. J Clin Endocrinol Metab 92: 4566-8.

Hennekes, H., and E.A. Nigg, 1994. The role of isoprenylation in membrane attachment of nuclear lamins. A single point mutation prevents proteolytic cleavage of the lamin A precursor and confers membrane binding properties. J Cell Sci 107 ( Pt 4): 1019-29.

Herrmann, H., and U. Aebi, 1998. Intermediate filament assembly: fibrillogenesis is driven by decisive dimer-dimer interactions. Curr Opin Struct Biol 8: 177-85.

Herrmann, H., and U. Aebi, 2004. Intermediate filaments: molecular structure, assembly mechanism, and integration into functionally distinct intracellular Scaffolds. Annu Rev Biochem 73: 749-89.

Herrmann, H., M. Haner, M. Brettel, N.O. Ku, and U. Aebi, 1999. Characterization of distinct early assembly units of different intermediate filament proteins. J Mol Biol 286: 1403-20.

Herrmann, H., H. Bar, L. Kreplak, S.V. Strelkov, and U. Aebi, 2007. Intermediate filaments: from cell architecture to nanomechanics. Nature Reviews Molecular Cell Biology 8: 562-573.

Herrmann, H., M. Haner, M. Brettel, S.A. Muller, K.N. Goldie, B. Fedtke, A. Lustig, W.W. Franke, and U. Aebi, 1996. Structure and assembly properties of the intermediate filament protein vimentin: The role of its head, rod and tail domains. Journal of Molecular Biology 264: 933-953.

Hess, J.F., M.S. Budamagunta, J.C. Voss, and P.G. FitzGerald, 2006. Characterization of the linker 1-2 region in human vimentin using site Directed Spin Labeling and Electron Paramagnetic Resonance. Faseb Journal 20: A96-A96.

Humphrey, W., A. Dalke, and K. Schulten, 1996. VMD: visual molecular dynamics. J Mol Graph 14: 33-8, 27-8.

Hutchison, C.J., 2002. Lamins: building blocks or regulators of gene expression? Nat Rev Mol Cell Biol 3: 848-58.

Ingber, D.E., 1993. Cellular Tensegrity - Defining New Rules of Biological Design That Govern the Cytoskeleton. Journal of Cell Science 104: 613-627.

Ishikawa, H., R. Bischoff, and H. Holtzer, 1968. Mitosis and Intermediate-Sized Filaments in Developing Skeletal Muscle. Journal of Cell Biology 38: 538-555.

Jafari, S.S., W.L. Maxwell, M. Neilson, and D.I. Graham, 1997. Axonal cytoskeletal changes after non-disruptive axonal injury. Journal of Neurocytology 26: 207-221.

Janmey, P.A., U. Euteneuer, P. Traub, and M. Schliwa, 1991. Viscoelastic properties of vimentin compared with other filamentous biopolymer networks. J Cell Biol 113: 155-160.

Janosi, L., and A.A. Gorfe, 2010. Segregation of Negatively Charged Phospholipids by the Polycationic and Farnesylated Membrane Anchor of Kras. Biophysical Journal 99: 3666-3674.

Jennings, B.R., and K. Parslow, 1988. Particle-Size Measurement - the Equivalent Spherical Diameter. Proceedings of the Royal Society of London Series a-Mathematical Physical and Engineering Sciences 419: 137-149.

Jones, M.K., A. Catte, J.C. Patterson, F.F. Gu, J.G. Chen, L. Li, and J.P. Segrest, 2009. Thermal Stability of Apolipoprotein A-I in High-Density Lipoproteins by Molecular Dynamics. Biophysical Journal 96: 354-371.

Jorgensen, W.L., D.S. Maxwell, and J. TiradoRives, 1996. Development and testing of the OPLS all-atom force field on conformational energetics and properties of organic liquids. Journal of the American Chemical Society 118: 11225-11236.

Kalinowski, A., Z. Qin, K. Coffey, R. Kodali, M.J. Buehler, M. Lösche, and K.N. Dahl, in revision. Calcium causes a conformational change in lamin A tail domain that promotes farnesyl-mediated membrane association

Keten, S., and M.J. Buehler, 2008a. Geometric confinement governs the rupture strength of H-bond assemblies at a critical length scale. Nano Letters 8: 743-748.

Keten, S., and M.J. Buehler, 2008b. Asymptotic strength limit of hydrogen-bond assemblies in proteins at vanishing pulling rates. Physical Review Letters 100: 198301.

Keten, S., Z.P. Xu, B. Ihle, and M.J. Buehler, 2010. Nanoconfinement controls stiffness, strength and mechanical toughness of beta-sheet crystals in silk. Nature Materials 9: 359-367.

Khatib, F., F. DiMaio, S. Cooper, M. Kazmierczyk, M. Gilski, S. Krzywda, H. Zabranska, I. Pichova, J. Thompson, Z. Popovic, M. Jaskolski, D. Baker, F.C. Grp, and F.V.C. Grp, 2011. Crystal structure of a monomeric retroviral protease solved by protein folding game players. Nature Structural & Molecular Biology 18: 1175-1177.

Kim, H., F. Nakamura, W. Lee, Y. Shifrin, P. Arora, and C.A. McCulloch, 2010. Filamin A is required for vimentin-mediated cell adhesion and spreading. American Journal of

Physiology-Cell Physiology 298: C221-C236.

Kinahan, M.E., E. Filippidi, S. Koster, X. Hu, H.M. Evans, T. Pfohl, D.L. Kaplan, and J. Wong, 2011. Tunable Silk: Using Microfluidics to Fabricate Silk Fibers with Controllable Properties. Biomacromolecules 12: 1504-1511.

Kirmse, R., S. Portet, N. Mucke, U. Aebi, H. Herrmann, and J. Langowski, 2007. A quantitative kinetic model for the in vitro assembly of intermediate filaments from tetrameric vimentin. J Biol Chem 282: 18563-72.

Klotzsch, E., M.L. Smith, K.E. Kubow, S. Muntwyler, W.C. Little, F. Beyeler, D. Gourdon, B.J. Nelson, and V. Vogel, 2009. Fibronectin forms the most extensible biological fibers displaying switchable force-exposed cryptic binding sites. Proc Natl Acad Sci U S A 106: 18267-72.

Kobayashi, N., T. Kigawa, S. Koshiba, M. Inoue, and S. Yokoyama, Solution structure of immunoglobulin like domain of mouse nuclear lamin. RCSB Protein Database DOI:10.2210/pdb1ufg/pdb

Koga, T., K. Taguchi, Y. Kobuke, T. Kinoshita, and M. Higuchi, 2003. Structural regulation of a peptide-conjugated graft copolymer: A simple model for amyloid formation. Chemistry-a European Journal 9: 1146-1156.

Koster, S., Y.C. Lin, H. Herrmann, and D.A. Weitz, 2010. Nanomechanics of vimentin intermediate filament networks. Soft Matter 6: 1910-1914.

Kreplak, L., and D. Fudge, 2007. Biomechanical properties of intermediate filaments: from tissues to single filaments and back. Bioessays 29: 26-35.

Kreplak, L., and H. Bar, 2009a. Severe Myopathy Mutations Modify the Nanomechanics of Desmin Intermediate Filaments. Journal Of Molecular Biology 385: 1043-1051.

Kreplak, L., and H. Bar, 2009b. Severe myopathy mutations modify the nanomechanics of desmin intermediate filaments. J Mol Biol 385: 1043-51.

Kreplak, L., U. Aebi, and H. Herrmann, 2004a. Molecular mechanisms underlying the assembly of intermediate filaments. Exp Cell Res 301: 77-83.

Kreplak, L., H. Herrmann, and U. Aebi, 2008. Tensile properties of single desmin intermediate filaments. Biophysical Journal 94: 2790-2799.

Kreplak, L., J. Doucet, P. Dumas, and F. Briki, 2004b. New aspects of the alpha-helix to beta-sheet transition in stretched hard alpha-keratin fibers. Biophysical Journal 87: 640-647.

Kreplak, L., H. Bar, J.F. Leterrier, H. Herrmann, and U. Aebi, 2005. Exploring the mechanical behavior of single intermediate filaments. Journal of Molecular Biology 354: 569-577.

Kreplak, L., A. Franbourg, F. Briki, F. Leroy, D. Dalle, and J. Doucet, 2002. A new deformation model of hard alpha-keratin fibers at the nanometer scale: Implications for hard alpha-keratin intermediate filament mechanical properties. Biophysical Journal 82:

2265-2274.

Krimm, I., C. Ostlund, B. Gilquin, J. Couprie, P. Hossenlopp, J.P. Mornon, G. Bonne, J.C. Courvalin, H.J. Worman, and S. Zinn-Justin, 2002. The Ig-like structure of the c-terminal domain of lamin A/C, mutated in muscular dystrophies, cardiomyopathy, and partial lipodystrophy. Structure 10: 811-823.

Kubben, N., M. Adriaens, W. Meuleman, J.W. Voncken, B. van Steensel, and T. Misteli, 2012. Mapping of lamin A- and progerin-interacting genome regions. Chromosoma 121: 447-64.

Lammerding, J., L.G. Fong, J.Y. Ji, K. Reue, C.L. Stewart, S.G. Young, and R.T. Lee, 2006. Lamins A and C but not lamin B1 regulate nuclear mechanics. Journal of Biological Chemistry 281: 25768-80.

Lazaridis, T., and M. Karplus, 1997. "New view" of protein folding reconciled with the old through multiple unfolding simulations. Science 278: 1928-1931.

Lazaridis, T., and M. Karplus, 1999. Effective energy function for proteins in solution. Proteins-Structure Function and Genetics 35: 133-152.

Lee, H.L.D., S.J. Sahl, M.D. Lew, and W.E. Moerner, 2012. The double-helix microscope super-resolves extended biological structures by localizing single blinking molecules in three dimensions with nanoscale precision. Applied Physics Letters 100: 153701.

Leterrier, J.F., J. Kas, J. Hartwig, R. Vegners, and P.A. Janmey, 1996. Mechanical effects of neurofilament cross-bridges. Modulation by phosphorylation, lipids, and interactions with F-actin. J Biol Chem 271: 15687-94.

Leuba, S.H., G.L. Yang, C. Robert, B. Samori, K. Vanholde, J. Zlatanova, and C. Bustamante, 1994. 3-Dimensional Structure of Extended Chromatin Fibers as Revealed by Tapping-Mode Scanning Force Microscopy. Proceedings of the National Academy of Sciences of the United States of America 91: 11621-11625.

Leung, K.F., R. Baron, B.R. Ali, A.I. Magee, and M.C. Seabra, 2007. Rab GTPases containing a CAAX motif are processed post-geranylgeranylation by proteolysis and methylation. J Biol Chem 282: 1487-97.

Lewis, M.K., P.C. Nahirney, V. Chen, B.B. Adhikari, J. Wright, M.K. Reedy, A.H. Bass, and K. Wang, 2003. Concentric intermediate filament lattice links to specialized Z-band junctional complexes in sonic muscle fibers of the type I male midshipman fish. J Struct Biol 143: 56-71.

Li, S., and B. Sun. 2012. Advances in cell mechanics. Springer, Heidelberg.

Lin, Y.C., N.Y. Yao, C.P. Broedersz, H. Herrmann, F.C. MacKintosh, and D.A. Weitz, 2010a. Origins of Elasticity in Intermediate Filament Networks. Physical Review Letters 104: 058101.

Lin, Y.C., C.P. Broedersz, A.C. Rowat, T. Wedig, H. Herrmann, F.C. MacKintosh, and D.A. Weitz, 2010b. Divalent Cations Crosslink Vimentin Intermediate Filament Tail Domains to Regulate Network Mechanics. Journal of Molecular Biology 399: 637-644.

Linding, R., J. Schymkowitz, F. Rousseau, F. Diella, and L. Serrano, 2004. A comparative study of the relationship between protein structure and beta-aggregation in globular and intrinsically disordered proteins. Journal of Molecular Biology 342: 345-353.

Liu, P., B. Kim, R.A. Friesner, and B.J. Berne, 2005. Replica exchange with solute tempering: a method for sampling biological systems in explicit water. Proc Natl Acad Sci U S A 102: 13749-54.

Liu, Q., D.I. Kim, J. Syme, P. LuValle, B. Burke, and K.J. Roux, 2010. Dynamics of lamin-A processing following precursor accumulation. PLoS One 5: e10874.

Luca, S., W.M. Yau, R. Leapman, and R. Tycko, 2007. Peptide conformation and supramolecular organization in amylin fibrils: Constraints from solid-state NMR. Biochemistry 46: 13505-13522.

Lutz, R.J., M.A. Trujillo, K.S. Denham, L. Wenger, and M. Sinensky, 1992. Nucleoplasmic localization of prelamin A: implications for prenylation-dependent lamin A assembly into the nuclear lamina. Proc Natl Acad Sci U S A 89: 3000-4.

Ma, L.L., J.Y. Xu, P.A. Coulombe, and D. Wirtz, 1999. Keratin filament suspensions show unique micromechanical properties. Journal of Biological Chemistry 274: 19145-19151.

MacCallum, J.L., M.S. Moghaddam, H.S. Chan, and D.P. Tieleman, 2007. Hydrophobic association of alpha-helices, steric dewetting, and enthalpic barriers to protein folding. Proc Natl Acad Sci U S A 104: 6206-10.

MacKerell, A.D., D. Bashford, M. Bellott, R.L. Dunbrack, J.D. Evanseck, M.J. Field, S. Fischer, J. Gao, H. Guo, S. Ha, D. Joseph-McCarthy, L. Kuchnir, K. Kuczera, F.T.K. Lau, C. Mattos, S. Michnick, T. Ngo, D.T. Nguyen, B. Prodhom, W.E. Reiher, B. Roux, M. Schlenkrich, J.C. Smith, R. Stote, J. Straub, M. Watanabe, J. Wiorkiewicz-Kuczera, D. Yin, and M. Karplus, 1998. All-atom empirical potential for molecular modeling and dynamics studies of proteins. Journal of Physical Chemistry B 102: 3586-3616.

Maniotis, A.J., C.S. Chen, and D.E. Ingber, 1997. Demonstration of mechanical connections between integrins cytoskeletal filaments, and nucleoplasm that stabilize nuclear structure. Proceedings of the National Academy of Sciences of the United States of America 94: 849-854.

Marko, J.F., and E.D. Siggia, 1995. Stretching DNA. Macromolecules 28: 8759-8770.

Marszalek, P.E., H. Lu, H. Li, M. Carrion-Vazquez, A.F. Oberhauser, K. Schulten, and J.M. Fernandez, 1999. Mechanical unfolding intermediates in titin modules. Nature 402: 100-3.

Mayo, S.L., B.D. Olafson, and W.A. Goddard, 1990. Dreiding - a Generic Force-Field for Molecular Simulations. Journal of Physical Chemistry 94: 8897-8909.

Meier, M., and J. Seelig, 2008. Length dependence of the coil reversible arrow beta-sheet transition in a membrane environment. Journal of the American Chemical Society 130: 1017-1024.

Minor, D.L., and P.S. Kim, 1994. Measurement of the Beta-Sheet-Forming Propensities of

Amino-Acids. Nature 367: 660-663.

Miteva, M.A., J.M. Brugge, J. Rosing, G.A. Nicolaes, and B.O. Villoutreix, 2004. Theoretical and experimental study of the D2194G mutation in the C2 domain of coagulation factor V. Biophys J 86: 488-98.

Moll, R., M. Divo, and L. Langbein, 2008. The human keratins: biology and pathology. Histochemistry and Cell Biology 129: 705-733.

Monticelli, L., S.K. Kandasamy, X. Periole, R.G. Larson, D.P. Tieleman, and S.J. Marrink, 2008. The MARTINI coarse-grained force field: Extension to proteins. Journal of Chemical Theory and Computation 4: 819-834.

Mucke, N., R. Kirmse, T. Wedig, J.F. Leterrier, and L. Kreplak, 2005. Investigation of the morphology of intermediate filaments adsorbed to different solid supports. Journal of Structural Biology 150: 268-276.

Mucke, N., L. Kreplak, R. Kirmse, T. Wedig, H. Herrmann, U. Aebi, and J. Langowski, 2004a. Assessing the flexibility of intermediate filaments by atomic force microscopy. Journal of Molecular Biology 335: 1241-1250.

Mucke, N., T. Wedig, A. Burer, L.N. Marekov, P.M. Steinert, J. Langowski, U. Aebi, and H. Herrmann, 2004b. Molecular and biophysical characterization of assembly-starter units of human vimentin. J Mol Biol 340: 97-114.

Munro, T.R., 1970. Relative Radiosensitivity of Nucleus and Cytoplasm of Chinese Hamster Fibroblasts. Radiation Research 42: 451-470.

Na, S., F. Chowdhury, B. Tay, M.X. Ouyang, M. Gregor, Y.X. Wang, G. Wiche, and N. Wang, 2009. Plectin contributes to mechanical properties of living cells. American Journal of Physiology-Cell Physiology 296: C868-C877.

Nadler, W., and U.H.E. Hansmann, 2008. Optimized explicit-solvent replica exchange molecular dynamics from scratch. Journal of Physical Chemistry B 112: 10386-10387.

Nadolski, M.J., and M.E. Linder, 2007. Protein lipidation. FEBS J 274: 5202-10.

Navarro, C.L., A. De Sandre-Giovannoli, R. Bernard, I. Boccaccio, A. Boyer, D. Genevieve, S. Hadj-Rabia, C. Gaudy-Marqueste, H.S. Smitt, P. Vabres, L. Faivre, A. Verloes, T. Van Essen, E. Flori, R. Hennekam, F.A. Beemer, N. Laurent, M. Le Merrer, P. Cau, and N. Levy, 2004. Lamin A and ZMPSTE24 (FACE-1) defects cause nuclear disorganization and identify restrictive dermopathy as a lethal neonatal laminopathy. Hum Mol Genet 13: 2493-503.

Nelson, M.T., W. Humphrey, A. Gursoy, A. Dalke, L.V. Kale, R.D. Skeel, and K. Schulten, 1996. NAMD: A parallel, object oriented molecular dynamics program. International Journal of Supercomputer Applications and High Performance Computing 10: 251-268.

Nicolet, S., H. Herrmann, U. Aebi, and S.V. Strelkov, 2010. Atomic structure of vimentin coil 2. Journal of Structural Biology 170: 369-376.

Nymeyer, H., and A.E. Garcia, 2003. Simulation of the folding equilibrium of alpha-helical

peptides: a comparison of the generalized Born approximation with explicit solvent. Proc Natl Acad Sci U S A 100: 13934-9.

Oberhauser, A.F., C. Badilla-Fernandez, M. Carrion-Vazquez, and J.M. Fernandez, 2002. The mechanical hierarchies of fibronectin observed with single-molecule AFM. Journal of Molecular Biology 319: 433-447.

Omary, M.B., 2009. "IF-pathies": a broad spectrum of intermediate filament-associated diseases. Journal of Clinical Investigation 119: 1756-1762.

Omary, M.B., P.A. Coulombe, and W.H.I. McLean, 2004. Mechanisms of disease: Intermediate filament proteins and their associated diseases. New England Journal of Medicine 351: 2087-2100.

Oostenbrink, C., A. Villa, A.E. Mark, and W.F. van Gunsteren, 2004. A biomolecular force field based on the free enthalpy of hydration and solvation: the GROMOS force-field parameter sets 53A5 and 53A6. J Comput Chem 25: 1656-76.

Ostlund, C., E.S. Folker, J.C. Choi, E.R. Gomes, G.G. Gundersen, and H.J. Worman, 2009. Dynamics and molecular interactions of linker of nucleoskeleton and cytoskeleton (LINC) complex proteins. Journal of Cell Science 122: 4099-4108.

Paci, E., and M. Karplus, 1999. Forced unfolding of fibronectin type 3 modules: an analysis by biased molecular dynamics simulations. J Mol Biol 288: 441-59.

Paci, E., and M. Karplus, 2000. Unfolding proteins by external forces and temperature: the importance of topology and energetics. Proc Natl Acad Sci U S A 97: 6521-6.

Panorchan, P., B.W. Schafer, D. Wirtz, and Y. Tseng, 2004. Nuclear envelope breakdown requires overcoming the mechanical integrity of the nuclear lamina. J Biol Chem 279: 43462-43467.

Parish, C.A., A.V. Smrcka, and R.R. Rando, 1996. The role of G protein methylation in the function of a geranylgeranylated beta gamma isoform. Biochemistry 35: 7499-505.

Parry, D.A.D., 2006. Hendecad repeat in segment 2A and linker L2 of intermediate filament chains implies the possibility of a right-handed coiled-coil structure. Journal of Structural Biology 155: 370-374.

Parry, D.A.D., and P.M. Steinert, 1999. Intermediate filaments: molecular architecture, assembly, dynamics and polymorphism. Quarterly Reviews of Biophysics 32: 99-187.

Parry, D.A.D., S.V. Strelkov, P. Burkhard, U. Aebi, and H. Herrmann, 2007. Towards a molecular description of intermediate filament structure and assembly. Experimental Cell Research 313: 2204-2216.

Paschek, D., S. Gnanakaran, and A.E. Garcia, 2005. Simulations of the pressure and temperature unfolding of an alpha-helical peptide. Proceedings of the National Academy of Sciences of the United States of America 102: 6765-6770.

Pelletier, V., N. Gal, P. Fournier, and M.L. Kilfoil, 2009. Microrheology of Microtubule

Solutions and Actin-Microtubule Composite Networks. Physical Review Letters 102: 188303.

Petersan, P.J., R.D. Deegan, M. Marder, and H.L. Swinney, 2004. Cracks in Rubber under Tension Exceed the Shear Wave Speed. Physical Review Letters 93: 015504.

Philips, M.R., 2012. Ras hitchhikes on PDE6delta. Nat Cell Biol 14: 128-9.

Plimpton, S., 1995. Fast Parallel Algorithms for Short-Range Molecular-Dynamics. Journal of Computational Physics 117: 1-19.

Polychronidou, M., A. Hellwig, and J. Grosshans, 2010. Farnesylated nuclear proteins Kugelkern and lamin Dm0 affect nuclear morphology by directly interacting with the nuclear membrane. Mol Biol Cell 21: 3409-20.

Pugno, N., A. Carpinteri, M. Ippolito, A. Mattoni, and L. Colombo, 2008. Atomistic fracture: QFM vs. MD. Engineering Fracture Mechanics 75: 1794-1803.

Qin, Z., and M.J. Buehler, 2010a. Structure and dynamics of human vimentin intermediate filament dimer and tetramer in explicit and implicit solvent models. J Mol Model 17: 37-48.

Qin, Z., and M.J. Buehler, 2010b. Cooperative deformation of hydrogen bonds in beta-strands and beta-sheet nanocrystals. Physical Review E 82: 061906.

Qin, Z., and M.J. Buehler, 2010c. Molecular dynamics simulation of the alpha-helix to beta-sheet transition in coiled protein filaments: evidence for a critical filament length scale. Phys Rev Lett 104: 198304.

Qin, Z., and M.J. Buehler, 2011a. Flaw Tolerance of Nuclear Intermediate Filament Lamina under Extreme Mechanical Deformation. Acs Nano 5: 3034-3042.

Qin, Z., and M. Buehler, 2011b. Dynamic Failure of a Lamina Meshwork in Cell Nuclei under Extreme Mechanical Deformation. BioNanoScience 1: 14-23.

Qin, Z., and M.J. Buehler, 2012a. Computational and theoretical modeling of intermediate filament networks: Structure, mechanics and disease. Acta Mechanica Sinica 28: 941-950.

Qin, Z., and M.J. Buehler, 2012b. Mechanical properties of crosslinks controls failure mechanism of hierarchical intermediate filament networks. Theoretical and Applied Mechanics Letters 2: 014005.

Qin, Z., and M.J. Buehler, 2012c. Cooperativity governs the size and structure of biological interfaces. J Biomech 45: 2778-83.

Qin, Z., L. Kreplak, and M.J. Buehler, 2009a. Nanomechanical properties of vimentin intermediate filament dimers. Nanotechnology 20: 425101.

Qin, Z., L. Kreplak, and M.J. Buehler, 2009b. Hierarchical structure controls nanomechanical properties of vimentin intermediate filaments. PLoS ONE 4: e7294.

Qin, Z., M.J. Buehler, and L. Kreplak, 2010. A multi-scale approach to understand the mechanobiology of intermediate filaments. J Biomech 43: 15-22.

Qin, Z., S. Cranford, T. Ackbarow, and M.J. Buehler, 2009c. Robustness-strength performance of hierachical alpha-helical protein filaments. International Journal of Applied Mechanics 1: 85-112.

Qin, Z., A. Kalinowski, K.N. Dahl, and M.J. Buehler, 2011. Structure and stability of the lamin A tail domain and HGPS mutant. Journal of Structural Biology 175: 425-433.

Rafik, M.E., J. Doucet, and F. Briki, 2004. The intermediate filament architecture as determined by X-ray diffraction modeling of hard alpha-keratin. Biophysical Journal 86: 3893-3904.

Ramachandran, G.N., C. Ramakrishnan, and V. Sasisekharan, 1963. Stereochemistry of polypeptide chain configurations. Journal of Molecular Biology 7: 95-9.

Rauscher, S., and R. Pomes, 2010. Molecular simulations of protein disorder. Biochemistry and Cell Biology-Biochimie Et Biologie Cellulaire 88: 269-290.

Reddy, S., and L. Comai, 2012. Lamin A, farnesylation and aging. Exp Cell Res 318: 1-7.

Rice, J.R., and G.F. Rosengren, 1968. Plane strain deformation near a crack tip in a power-law hardening material. Journal of the Mechanics and Physics of Solids 16: 1-12.

Rief, M., J.M. Fernandez, and H.E. Gaub, 1998. Elastically coupled two-level systems as a model for biopolymer extensibility. Physical Review Letters 81: 4764-4767.

Root, D.D., V.K. Yadavalli, J.G. Forbes, and K. Wang, 2006. Coiled-coil nanomechanics and uncoiling and unfolding of the superhelix and alpha-helices of myosin. Biophysical Journal 90: 2852-2866.

Rose, A., and I. Meier, 2004. Scaffolds, levers, rods and springs: diverse cellular functions of long coiled-coil proteins. Cellular and Molecular Life Sciences 61: 1996-2009.

Rowat, A.C., L.J. Foster, M.M. Nielsen, M. Weiss, and J.H. Ipsen, 2005. Characterization of the elastic properties of the nuclear envelope. J R Soc Interface 2: 63-69.

Scaffidi, P., and T. Misteli, 2006. Lamin A-dependent nuclear defects in human aging. Science 312: 1059-1063.

Schermelleh, L., P.M. Carlton, S. Haase, L. Shao, L. Winoto, P. Kner, B. Burke, M.C. Cardoso, D.A. Agard, M.G. Gustafsson, H. Leonhardt, and J.W. Sedat, 2008. Subdiffraction multicolor imaging of the nuclear periphery with 3D structured illumination microscopy. Science 320: 1332-1336.

Schirmer, E.C., and R. Foisner, 2007. Proteins that associate with lamins: many faces, many functions. Experimental Cell Research 313: 2167-2179.

Schopferer, M., H. Bar, B. Hochstein, S. Sharma, N. Mucke, H. Herrmann, and N. Willenbacher, 2009. Desmin and Vimentin Intermediate Filament Networks: Their Viscoelastic Properties Investigated by Mechanical Rheometry. Journal of Molecular Biology 388: 133-143.

Schoumacher, M., R.D. Goldman, D. Louvard, and D.M. Vignjevic, 2010. Actin,

microtubules, and vimentin intermediate filaments cooperate for elongation of invadopodia. Journal of Cell Biology 189: 541-556.

Schwaiger, I., C. Sattler, D.R. Hostetter, and M. Rief, 2002. The myosin coiled-coil is a truly elastic protein structure. Nature Materials 1: 232-235.

Shumaker, D.K., R.I. Lopez-Soler, S.A. Adam, H. Herrmann, R.D. Moir, T.P. Spann, and R.D. Goldman, 2005. Functions and dysfunctions of the nuclear lamin Ig-fold domain in nuclear assembly, growth, and Emery-Dreifuss muscular dystrophy. Proc Natl Acad Sci U S A 102: 15494-9.

Silvius, J.R., and F. l'Heureux, 1994. Fluorimetric evaluation of the affinities of isoprenylated peptides for lipid bilayers. Biochemistry 33: 3014-22.

Simon, D.N., and K.L. Wilson, 2011. The nucleoskeleton as a genome-associated dynamic 'network of networks'. Nat Rev Mol Cell Biol 12: 695-708.

Sivaramakrishnan, S., J.V. DeGiulio, L. Lorand, R.D. Goldman, and K.M. Ridge, 2008. Micromechanical properties of keratin intermediate filament networks. Proc Natl Acad Sci U S A 105: 889-94.

Smith, T.A., S.V. Strelkov, P. Burkhard, U. Aebi, and D.A. Parry, 2002. Sequence comparisons of intermediate filament chains: evidence of a unique functional/structural role for coiled-coil segment 1A and linker L1. J Struct Biol 137: 128-45.

Snow, C.D., E.J. Sorin, Y.M. Rhee, and V.S. Pande, 2005. How well can simulation predict protein folding kinetics and thermodynamics? Annual Review of Biophysics and Biomolecular Structure 34: 43-69.

Sokolova, A.V., L. Kreplak, T. Wedig, N. Mucke, D.I. Svergun, H. Herrmann, U. Aebi, and S.V. Strelkov, 2006. Monitoring intermediate filament assembly by small-angle x-ray scattering reveals the molecular architecture of assembly intermediates. Proc Natl Acad Sci U S A 103: 16206-11.

Sotomayor, M., and K. Schulten, 2007. Single-molecule experiments in vitro and in silico. Science 316: 1144-1148.

Spassov, V.Z., L. Yan, and S. Szalma, 2002. Introducing an implicit membrane in generalized Born/solvent accessibility continuum solvent models. Journal of Physical Chemistry B 106: 8726-8738.

Steinert, P.M., L.N. Marekov, and D.A. Parry, 1993. Diversity of intermediate filament structure. Evidence that the alignment of coiled-coil molecules in vimentin is different from that in keratin intermediate filaments. J Biol Chem 268: 24916-25.

Stierle, V., J. Couprie, C. Ostlund, I. Krimm, S. Zinn-Justin, P. Hossenlopp, H.J. Worman, J.C. Courvalin, and I. Duband-Goulet, 2003. The carboxyl-terminal region common to lamins A and C contains a DNA binding domain. Biochemistry 42: 4819-28.

Storm, C., J.J. Pastore, F.C. MacKintosh, T.C. Lubensky, and P.A. Janmey, 2005. Nonlinear elasticity in biological gels. Nature 435: 191-194.

Strelkov, S.V., H. Herrmann, and U. Aebi, 2003. Molecular architecture of intermediate filaments. Bioessays 25: 243-251.

Strelkov, S.V., H. Herrmann, N. Geisler, T. Wedig, R. Zimbelmann, U. Aebi, and P. Burkhard, 2002. Conserved segments 1A and 2B of the intermediate filament dimer: their atomic structures and role in filament assembly. Embo Journal 21: 1255-1266.

Strelkov, S.V., H. Herrmann, N. Geisler, A. Lustig, S. Ivaninskii, R. Zimbelmann, P. Burkhard, and U. Aebi, 2001. Divide-and-conquer crystallographic approach towards an atomic structure of intermediate filaments. Journal of Molecular Biology 306: 773-781.

Sugita, Y., and Y. Okamoto, 1999. Replica-exchange molecular dynamics method for protein folding. Chemical Physics Letters 314: 141-151.

Sulkowska, J.I., and M. Cieplak, 2007. Mechanical stretching of proteins - a theoretical survey of the Protein Data Bank. Journal of Physics-Condensed Matter 19: 283201.

Sun, H., 1998. COMPASS: An ab initio force-field optimized for condensed-phase applications - Overview with details on alkane and benzene compounds. Journal of Physical Chemistry B 102: 7338-7364.

Swendsen, R.H., and J.S. Wang, 1986. Replica Monte Carlo simulation of spin glasses. Phys Rev Lett 57: 2607-2609.

Sylvius, N., and F. Tesson, 2006. Lamin A/C and cardiac diseases. Curr Opin Cardiol 21: 159-65.

Szekely, J.G., T.P. Copps, and B.D. Morash, 1980. Radiation-Induced Invagination of the Nuclear-Envelope. Radiation Research 83: 621-632.

Taimen, P., K. Pfleghaar, T. Shimi, D. Moller, K. Ben-Harush, M.R. Erdos, S.A. Adam, H. Herrmann, O. Medalia, F.S. Collins, A.E. Goldman, and R.D. Goldman, 2009. A progeria mutation reveals functions for lamin A in nuclear assembly, architecture, and chromosome organization. Proc Natl Acad Sci U S A 106: 20788-93.

Tsemekhman, K., L. Goldschmidt, D. Eisenberg, and D. Baker, 2007. Cooperative hydrogen bonding in amyloid formation. Protein Science 16: 761-764.

van der Kooi, A.J., G. Bonne, B. Eymard, D. Duboc, B. Talim, M. Van der Valk, P. Reiss, P. Richard, L. Demay, L. Merlini, K. Schwartz, H.F. Busch, and M. de Visser, 2002. Lamin A/C mutations with lipodystrophy, cardiac abnormalities, and muscular dystrophy. Neurology 59: 620-3.

van Duin, A.C.T., S. Dasgupta, F. Lorant, and W.A. Goddard, 2001. ReaxFF: A reactive force field for hydrocarbons. Journal of Physical Chemistry A 105: 9396-9409.

Vanommeslaeghe, K., E. Hatcher, C. Acharya, S. Kundu, S. Zhong, J. Shim, E. Darian, O. Guvench, P. Lopes, I. Vorobyov, and A.D. MacKerell, 2010. CHARMM General Force Field: A Force Field for Drug-Like Molecules Compatible with the CHARMM All-Atom Additive Biological Force Fields. Journal of Computational Chemistry 31: 671-690.

Verstraeten, V.L., J.Y. Ji, K.S. Cummings, R.T. Lee, and J. Lammerding, 2008. Increased mechanosensitivity and nuclear stiffness in Hutchinson-Gilford progeria cells: effects of farnesyltransferase inhibitors. Aging Cell 7: 383-93.

Vivian, J.T., and P.R. Callis, 2001. Mechanisms of tryptophan fluorescence shifts in proteins. Biophys J 80: 2093-109.

Vlcek, S., and R. Foisner, 2007. Lamins and lamin-associated proteins in aging and disease. Curr Opin Cell Biol 19: 298-304.

Wang, K., and R. Ramirezmitchell, 1983. A Network of Transverse and Longitudinal Intermediate Filaments Is Associated with Sarcomeres of Adult Vertebrate Skeletal-Muscle. Journal of Cell Biology 96: 562-570.

Wang, K., R. Mccarter, J. Wright, J. Beverly, and R. Ramirezmitchell, 1993a. Viscoelasticity of the Sarcomere Matrix of Skeletal-Muscles - the Titin Myosin Composite Filament Is a Dual-Stage Molecular Spring. Biophysical Journal 64: 1161-1177.

Wang, N., and D. Stamenovic, 2000. Contribution of intermediate filaments to cell stiffness, stiffening, and growth. American Journal of Physiology-Cell Physiology 279: C188-C194.

Wang, N., and D. Stamenovic, 2002. Mechanics of vimentin intermediate filaments. J Muscle Res Cell Motil 23: 535-40.

Wang, N., J.P. Butler, and D.E. Ingber, 1993b. Mechanotransduction across the Cell-Surface and through the Cytoskeleton. Science 260: 1124-1127.

Wiche, G., 1998. Role of plectin in cytoskeleton organization and dynamics. Journal of Cell Science 111: 2477-2486.

Wilhelmsen, K., S.H.M. Litjens, I. Kuikman, N. Tshimbalanga, H. Janssen, I. van den Bout, K. Raymond, and A. Sonnenberg, 2005. Nesprin-3, a novel outer nuclear membrane protein, associates with the cytoskeletal linker protein plectin. Journal of Cell Biology 171: 799-810.

Wilson, K.L., and J.M. Berk, 2010. The nuclear envelope at a glance. J Cell Sci 123: 1973-8.

Wilson, K.L., M.S. Zastrow, and K.K. Lee, 2001. Lamins and disease: Insights into nuclear infrastructure. Cell 104: 647-650.

Wirtz, D., 2009. Particle-Tracking Microrheology of Living Cells: Principles and Applications. Annual Review of Biophysics 38: 301-326.

Worman, H.J., C. Ostlund, and Y. Wang, 2010. Diseases of the nuclear envelope. Cold Spring Harb Perspect Biol 2: a000760.

Xu, X., R. Ishima, and J.B. Ames, 2011. Conformational dynamics of recoverin's Ca2+-myristoyl switch probed by 15N NMR relaxation dispersion and chemical shift analysis. Proteins 79: 1910-22.

Xu, Z.P., R. Paparcone, and M.J. Buehler, 2010. Alzheimer's A beta(1-40) Amyloid Fibrils Feature Size-Dependent Mechanical Properties. Biophysical Journal 98: 2053-2062.

Yamada, S., D. Wirtz, and P.A. Coulombe, 2003. The mechanical properties of simple epithelial keratins 8 and 18: discriminating between interfacial and bulk elasticities. Journal of Structural Biology 143: 45-55.

Yang, S.H., S.Y. Chang, S.X. Ren, Y.B. Wang, D.A. Andres, H.P. Spielmann, L.G. Fong, and S.G. Young, 2011. Absence of progeria-like disease phenotypes in knock-in mice expressing a non-farnesylated version of progerin. Human Molecular Genetics 20: 436-444.

Young, S.G., L.G. Fong, and S. Michaelis, 2005a. Prelamin A, Zmpste24, misshapen cell nuclei, and progeria--new evidence suggesting that protein farnesylation could be important for disease pathogenesis. Journal of Lipid Research 46: 2531-58.

Young, S.G., L.G. Fong, and S. Michaelis, 2005b. Prelamin A, Zmpste24, misshapen cell nuclei, and progeria--new evidence suggesting that protein farnesylation could be important for disease pathogenesis. J Lipid Res 46: 2531-58.

Young, S.G., M. Meta, S.H. Yang, and L.G. Fong, 2006. Prelamin A farnesylation and progeroid syndromes. Journal of Biological Chemistry 281: 39741-5.

Zagrovic, B., C.D. Snow, M.R. Shirts, and V.S. Pande, 2002. Simulation of folding of a small alpha-helical protein in atomistic detail using worldwide-distributed computing. Journal of Molecular Biology 323: 927-937.

Zastrow, M.S., S. Vlcek, and K.L. Wilson, 2004. Proteins that bind A-type lamins: integrating isolated clues. Journal of Cell Science 117: 979-87.

Zhang, H., T. Ackbarow, and M.J. Buehler, 2008. Muscle dystrophy single point mutation in the 2B segment of lamin A does not affect the mechanical properties at the dimer level. Journal of biomechanics 41: 1295-1301.

Zhou, R.H., and B.J. Berne, 2002. Can a continuum solvent model reproduce the free energy landscape of a beta-hairpin folding in water? Proceedings of the National Academy of Sciences of the United States of America 99: 12777-12782.

Zhou, R.H., B.J. Berne, and R. Germain, 2001. The free energy landscape for beta hairpin folding in explicit water. Proceedings of the National Academy of Sciences of the United States of America 98: 14931-14936.

# 11 APPENDIX

## 11.1 The mesoscopic model of nuclear lamina

To address the failure mechanism of the intermediate filament meshwork, the interpretation of the dynamic fracture property of the intermediate filament meshwork requires a large scale meshwork model (in the order of μm) as well as accurate representation of the dynamical property of each filament and their interactions with atomic interaction detail (in the order of $Å^2$). Thereby, the multi-scale modeling can be a strategy combining accuracy and efficiency, which includes the full atomic modeling for single filaments and the mesoscopic model for intermediate filament meshwork. The full atomic model provides an accurate description of the physical mechanisms governing the yielding (unfolding of alpha-helics) and stiffening (structural transition) process of each filament under loading, and records the accurate description of the force-extension relation of the single filament during the loading history. The mesoscopic model inherits the physical properties of the former and provides a faithful estimation of dynamic fracture property in the large scale.

Similar model has been used in earlier studies of fracture mechanism in crystalline materials and provides an effective way to describe the nonlinear constitutive behavior based on computationally effective pair potential functions. It is noted that this model does not include the nonbonded interaction because the intermediate filament studied here is fully polymerized with a uniform diameter of 10 nm, which is true for most of intermediate filaments. Therefore the intermolecular interaction is much weaker than its tensile or bending resistance.

**Modeling method.** The mesoscopic model used here is set up based on a combination of experimental and full atomistic data (Aebi et al., 1986; Goldberg et al., 2008b; Qin et al., 2009b; Xu et al., 2010). We use a simple mesoscopic model describing each intermediate filament as a series of beads interacting according to nonlinear interparticle multibody potentials. The model is designed by our desire to develop a simple model to derive generic insight into the mechanical properties and mechanisms. We note that even though such a simple model formulation does not allow us to derive quantitative conclusions for phenomena pertaining to specific types of nuclear laminas, it does enable us to understand universal, generic relationships between underlying molecular mechanisms, resulting nonlinear properties of the material, and the failure behavior of intermediate filament meshworks.

The total energy is given by:

$$E_x = E_T + E_B, \tag{11.1}$$

The total energy is given by the sum over all pair wise and three-body interactions:

$$E_T = \sum_{\text{pair}} \varphi_T(r) \tag{11.2}$$

and

$$E_B = \sum_{\text{triplets}} \varphi_B(\theta) \tag{11.3}$$

Here we approximate the nonlinear force-extension behavior under tensile loading with a multi-polynomial potential model that has been used successfully in the earlier study of deformation of cytoplasm single filament(Bertaud et al., 2010). The tensile force between two particles (beads as illustrated in Fig. S1c) is described as:

$$F_T(r) = -\partial\varphi_T(r)/\partial r \tag{11.4}$$

where

$$\frac{\partial\varphi_T(r)}{\partial r} = \left[\exp\left(\frac{r-r_b}{r_b}\Xi\right)+1\right]^{-1}\begin{cases} k_1(r-r_0) & r < r_1 \\ R_1 + k_2(r-r_1) & r < r_2 \\ R_2 + k_3^1(r-r_2) + k_3^2(r-r_2)^2 + k_3^3(r-r_2)^3 & r < r_3 \\ R_3 & r \geq r_3 \end{cases} \tag{11.5}$$

In Eq. 11.5, $k_i$ and $r_i$ are spring constants that derived directly from the force-extension curve of the tension test of full atomic model. The Fermi–Dirac distribution function introduces two additional parameters $r_b$ and $\Xi$ (Buehler and Gao, 2006). The parameter $r_b$ denotes the critical separation distance for breaking of the filament and the parameter $\Xi$ describes the amount of smoothing around the breaking point (the smaller $\Xi$, the smoother the curve becomes). Similar strategy to model the potential near rupture for numerical analyses has been done in earlier work.

The bending energy (as illustrated in Fig. S1d) is given by:

$$\varphi_B(\theta) = \frac{1}{2}k_B(\theta-\theta_0)^2 \tag{11.6}$$

with $k_B$ relating to the bending stiffness of the intermediate filament $EI$ through $k_B = 3EI/r_0$. The parameter $EI$ relates to the intermediate filament persistence length $L_P$ through $EI = L_P K_B T$, where $K_B$ is the Boltzmann constant and $T$ is the temperature.

The geometry of the meshwork is obtained from experimental observations of the nuclear lamina of *Xenopus* oocytes (Aebi et al., 1986). The meshwork is composed of two sets of near-orthogonal intermediate filaments with a lattice constant of $d$=50 nm, and we use $d$ to normalize the crack length and that value gives the size of defects. We use mesoscopic beads to model the each intermediate filament within the meshwork and use $r_0 = 5$ nm, this length is much smaller than the persistence length of the full length filament (~1 μm), and it equals to the radius of the full length filament.

**Computational experiments.** Calculations are carried out in two steps, 1) relaxation followed by 2) loading. Relaxation is achieved by heating up the system, then annealing the

structure at temperature of 300 K, followed by energy minimization. After relaxation, we keep the system at 300 K in an NVT ensemble (constant temperature, constant volume, and constant number of particles) and apply loading by displacement boundary conditions (by fixing one single layer of beads near the meshwork boundary and apply the load in normal directions. This set-up resembles linear rails with guides clamped to the boundary, resulting in biaxial deformation independently(Petersan et al., 2004)), continuously displacing particles in the boundary in a speed of 0.01 Å/ps. Studies with varying loading rates were carried out based on the mesoscopic model of single filaments. By comparing with force-extension curves obtained from atomic model of vimentin intermediate filaments and experiments of general intermediate filaments near equilibrium(Qin et al., 2009b), the loading rate of 0.01 Å/ps eliminates the difference between the mechanical response of the mesoscopic model and those earlier results. It is confirmed that the loading rate chosen here leads to quasi static deformation conditions.

**Damping.** Damping effects are included in the model by considering the energy dissipation of the intermediate filament in motion caused by the viscosity of water environment. We note because of the small character dimension of the intermediate filament, the Reynolds number $\ll 2300$ (Batchelor, 2000) and the drag force is approximately proportional to particle velocity (laminar flow). We use the Stokes' law to measure the drag force by (Batchelor, 2000):

$$f_{\text{drag}} = -6\pi\mu R v \tag{11.7}$$

where $\mu = 8.6 \times 10^{-4}$ Pa · s is the fluid viscosity constant of water at room temperature, $R$ is the equivalent spherical radius of the mesoscopic bead, which equals to the radius of a sphere of equivalent volume given by (Jennings and Parslow, 1988)

$$R = \left(\frac{3}{16} b^2 r_0\right)^{1/3} \tag{11.8}$$

with geometry parameters of the mesoscopic bead given as $R = 4.5$ nm. The parameter $v$ denotes the relative velocity of particle motion in the continuous viscous fluid.

**Parameters.** In Eq. 11.5, $k_i$ and $r_i$ are spring constants that derived directly from the force-extension curve of the tension test of full atomic model, without empirical fitting. $r_0$ is the equilibrium distance between pair beads. α-helix domains within the filament are intact before the extension reaches $r_1 - r_0$ and the slope of the force-extension curve is constant as $k_1$. The extension beyond $r_1 - r_0$ leads to the unfolding of the alpha-helix domains until they become nearly fully unfolded at $r_2 - r_0$, and in this extension region the force-extension curve is linear with a slope of $k_2$. The third broad region before the extension of $r_3 - r_0$ corresponds to the stiffening of the material because of the alpha-beta transition, and the nonlinearity of the force extension curve is expressed by the polynomial function with stiffness parameters $k_3^1$, $k_3^2$ and $k_3^3$. For the forth region, the subunits within the filament slide against each other under a constant force. The parameters $R_1$, $R_2$ and $R_3$ are calculated from force continuity conditions. The values of these parameters are given in Table 1.

**Table 11.1 Geometric and mechanical parameters for the model.**

| Parameter and units | Numerical value |
|---|---|
| Equilibrium bead distance $r_0$ (in Å) | 50 |
| Critical distances $r_1, r_2, r_3$ (in Å) | 75, 95, 138, 180 |
| Tensile stiffness parameters $k_1$, $k_2$ (in kcal/mol/Å$^2$) | 0.1595, 0.0324, |
| Tensile stiffness parameters for the nonlinear region $k_3^1$ (in kcal/mol/Å$^2$), $k_3^1$ (in kcal/mol/Å$^3$), $k_3^1$ (in kcal/mol/Å$^4$) | 0.2044, 0.0146, $9.2465 \times 10^{-4}$ |
| Force continuity conditions $R_1$, $R_2$ and $R_3$ (in kcal/mol/Å) | 3.9877, 4.6357, 113.9364 |
| Bond breaking distance $r_b$ (in Å) | 180 |
| Equilibrium angle $\theta_0$ (in rad) | $\pi$ |
| Bending stiffness parameter $k_B$ (in kcal/mol/rad$^2$) | 169.51 |
| Mass of each mesoscale particle (in amu) | 230913 |
| Switch function $\Xi$ | 300 |

## 11.2 The force field of the farnesyl group

Topology file (inserted in file top_all27_prot_lipid.rtf)

```
RESI CYF          0.00 ! Farnesylated CYS amino acid, always at the end of the peptide, combine
charmm27 with cgenff
GROUP
ATOM N    NH1    -0.47 !      |
ATOM HN   H       0.31 !  HN-N
ATOM CA   CT1     0.07 !      |   HB1
ATOM HA   HB      0.09 !      |   |
GROUP                  !  HA-CA--CB--SG--
ATOM CB   CT2    -0.13 !      |   |
ATOM HB1  HA      0.09 !      |   HB2
ATOM HB2  HA      0.09 !   O=C
ATOM SG   S      -0.10 !      |
GROUP
ATOM C1   CG321  -0.13 !
ATOM H11  HGA2    0.09 !
ATOM H12  HGA2    0.09 !
GROUP
ATOM C2   CG2D1  -0.15 !
```

```
ATOM H21   HGA4     0.15  ! H141H142H143                  H41 H42 H43
GROUP                    !   \|/                           \|/
ATOM C3    CG2D1    0.00  !     C14      H121 H91    H61 H62   C4   H21
GROUP                    !       \       |     |       \/     |    /
ATOM C4    CG331   -0.27  !         C13=C12   C9-H92    C6      C3=C2    (SG)--CYS
ATOM H41   HGA3     0.09  !        /       \  /  \       /  \  /       \  /
ATOM H42   HGA3     0.09  !H151-C15        C11      C8=C7    C5          C1
ATOM H43   HGA3     0.09  !     /\       /  \     |    \  /  \       /  \
GROUP                    ! H152H153 H111H112   C10 H71H51 H52   H11 H12
ATOM C5    CG321   -0.18  !                        /|\
ATOM H51   HGA2     0.09  !                    H101H102H103
ATOM H52   HGA2     0.09  !
GROUP
ATOM C6    CG321   -0.18
ATOM H61   HGA2     0.09
ATOM H62   HGA2     0.09
GROUP
ATOM C7    CG2D1   -0.15
ATOM H71   HGA4     0.15
GROUP
ATOM C8    CG2D1    0.00
GROUP
ATOM C9    CG321   -0.18
ATOM H91   HGA2     0.09
ATOM H92   HGA2     0.09
GROUP
ATOM   C10 CG331   -0.27
ATOM H101 HGA3     0.09
ATOM H102 HGA3     0.09
ATOM H103 HGA3     0.09
GROUP
ATOM   C11 CG321   -0.18
ATOM H111 HGA2     0.09
ATOM H112 HGA2     0.09
GROUP
ATOM   C12 CG2D1   -0.15
ATOM H121 HGA4     0.15
GROUP
ATOM   C13 CG2D1    0.00
GROUP
ATOM   C14 CG331   -0.27
ATOM H141 HGA3     0.09
ATOM H142 HGA3     0.09
ATOM H143 HGA3     0.09
```

```
GROUP
ATOM   C15 CG331   -0.27
ATOM H151 HGA3      0.09
ATOM H152 HGA3      0.09
ATOM H153 HGA3      0.09
GROUP
ATOM C      C          0.51
ATOM O      O         -0.51
BOND CB CA    SG CB    N HN   N   CA
BOND C   CA    C +N   CA HA   CB HB1
BOND CB HB2   SG C1   C1 H11   C1 H12
BOND C1 C2   C2 H21
DOUBLE O   C
DOUBLE C2 C3
BOND C3 C4   C4 H41   C4 H42
BOND C4 H43   C3 C5   C5 H51   C5 H52
BOND C5 C6   C6 H61   C6 H62   C6 C7
BOND C7 H71
DOUBLE C7 C8
BOND C8 C10   C10 H101   C10 H102
BOND C10 H103   C8 C9   C9 H91   C9 H92
BOND C9 C11   C11 H111   C11 H112   C11 C12
BOND C12 H121
DOUBLE C12 C13
BOND C13 C14   C14 H141   C14 H142
BOND C14 H143   C13 C15   C15 H151   C15 H152
BOND C15 H153
IMPR N -C CA HN   C CA +N O
CMAP -C   N   CA   C    N   CA   C   +N
DONOR HN N
ACCEPTOR O C
IC -C    CA    *N    HN     1.3479 123.9300   180.0000 114.7700   0.9982
IC -C    N     CA    C      1.3479 123.9300   180.0000 105.8900   1.5202
IC N     CA    C     +N     1.4533 105.8900   180.0000 118.3000   1.3498
IC +N    CA    *C    O      1.3498 118.3000   180.0000 120.5900   1.2306
IC CA    C     +N    +CA    1.5202 118.3000   180.0000 124.5000   1.4548
IC N     C     *CA   CB     1.4533 105.8900   121.7900 111.9800   1.5584
IC N     C     *CA   HA     1.4533 105.8900  -116.3400 107.7100   1.0837
IC N     CA    CB    SG     1.4533 111.5600   180.0000 113.8700   1.8359
IC SG    CA    *CB   HB1    1.8359 113.8700   119.9100 107.2400   1.1134
IC SG    CA    *CB   HB2    1.8359 113.8700  -125.3200 109.8200   1.1124
IC CA    CB    SG    C1     1.5584 113.8700   176.9600  97.1500   1.3341
IC CB    SG    C1    C2     1.5584 113.8700   176.9600  97.1500   1.3341
IC H11   SG    *C1   C2     1.1134 107.2400   180.0000 129.6000   1.5519
```

```
IC H12   SG   *C1   C2     1.1134   77.2400   180.0000 129.6000   1.5519
IC SG    C1   C2   C3     1.8359   77.2400   180.0000 129.6000   1.3597
IC H21   C2   C3   C4     1.1134  120.0000     0.0000 120.0000   1.5584
IC H41   C4   C3   C5     1.1134  120.0000   180.0000 120.0000   1.5519
IC H42   C4   C3   C5     1.1134  120.0000    60.0000 120.0000   1.5519
IC H43   C4   C3   C5     1.1134  120.0000   -60.0000 120.0000   1.5519
IC C1    C2   C3   C5     1.5519  120.0000   180.0000 120.0000   1.5519
IC C2    C3   C5   C6     1.3597  120.0000   180.0000 120.0000   1.5519
IC C3    C6   *C5  H51    1.5584   60.0000   180.0000 120.0000   1.1134
IC C3    C6   *C5  H52    1.5584   60.0000   180.0000 -120.000   1.1134
IC C3    C5   C6   C7     1.5584   60.0000   180.0000 -60.0000   1.5584
IC C7    C5   *C6  H61    1.5584  -60.0000   180.0000 120.0000   1.1134
IC C7    C5   *C6  H62    1.5584  -60.0000   180.0000 -120.000   1.1134
IC C5    C6   C7   C8     1.5584  -60.0000   180.0000  120.000   1.3597
IC H71   C7   C8   C10    1.1134  -120.000     0.0000 -120.000   1.5584
IC H101 C10   C8   C9     1.1134   120.000   180.0000 120.0000   1.5519
IC H102 C10   C8   C9     1.1134   120.000    60.0000 120.0000   1.5519
IC H103 C10   C8   C9     1.1134   120.000   -60.0000 120.0000   1.5519
IC C6    C7   C8   C9     1.5584  120.0000     0.0000  120.000   1.5584
IC C7    C8   C9   C11    1.3597  120.0000   180.0000  -60.000   1.5584
IC C11   C8   *C9  H91    1.5584   60.0000   180.0000  120.000   1.1134
IC C11   C8   *C9  H92    1.5584   60.0000   180.0000 -120.000   1.1134
IC C8    C9   C11  C12    1.5584  -60.0000   180.0000   60.000   1.5584
IC C9    C12 *C11  H111   1.5584   60.0000   180.0000  120.000   1.1134
IC C9    C12 *C11  H112   1.5584   60.0000   180.0000 -120.000   1.1134
IC C9    C11  C12  C13    1.5584   60.0000   180.0000 -120.000   1.3597
IC C9    C11  C12  C13    1.5584   60.0000   180.0000 -120.000   1.3597
IC H121 C12  C13  C14    1.1134  120.0000     0.0000  120.000   1.5584
IC C11   C12  C13  C15    1.5584 -120.000     0.0000 -120.000   1.5584
IC H151 C15  C13  C12    1.1134   120.000   180.0000 120.0000   1.5519
IC H152 C15  C13  C12    1.1134   120.000    60.0000 120.0000   1.5519
IC H153 C15  C13  C12    1.1134   120.000   -60.0000 120.0000   1.5519
IC H141 C14  C13  C12    1.1134   120.000   180.0000 120.0000   1.5519
IC H142 C14  C13  C12    1.1134   120.000    60.0000 120.0000   1.5519
IC H143 C14  C13  C12    1.1134   120.000   -60.0000 120.0000   1.5519
```

Parameter file: merge par_all36_cgenff.prm and par_all27_prot_lipid.prm for each section (bond, angle, dihedral *etc.*)